

SENSING MOLECULAR ADSORPTION THROUGH INTERFACIAL  
ELECTRON SCATTERING IN ATOM-SCALE JUNCTIONS

BY

PATRICK JAMES CASTLE

B.S., United States Air Force Academy, 1993  
M.S., University of Illinois at Urbana-Champaign, 1994

DISSERTATION

Submitted in partial fulfillment of the requirements  
for the degree of Doctor of Philosophy in Chemistry  
in the Graduate College of the  
University of Illinois at Urbana-Champaign, 2005

Urbana, Illinois

Report Documentation Page			Form Approved OMB No. 0704-0188		
Public reporting burden for the collection of information is estimated to average 1 hour per response, including the time for reviewing instructions, searching existing data sources, gathering and maintaining the data needed, and completing and reviewing the collection of information. Send comments regarding this burden estimate or any other aspect of this collection of information, including suggestions for reducing this burden, to Washington Headquarters Services, Directorate for Information Operations and Reports, 1215 Jefferson Davis Highway, Suite 1204, Arlington VA 22202-4302. Respondents should be aware that notwithstanding any other provision of law, no person shall be subject to a penalty for failing to comply with a collection of information if it does not display a currently valid OMB control number.					
1. REPORT DATE <b>15 OCT 2005</b>		2. REPORT TYPE <b>N/A</b>		3. DATES COVERED <b>-</b>	
4. TITLE AND SUBTITLE <b>Sensing Molecular Adsorption Through Interfacial Electron Scattering In Atom-Scale Junctions</b>				5a. CONTRACT NUMBER	
				5b. GRANT NUMBER	
				5c. PROGRAM ELEMENT NUMBER	
6. AUTHOR(S)				5d. PROJECT NUMBER	
				5e. TASK NUMBER	
				5f. WORK UNIT NUMBER	
7. PERFORMING ORGANIZATION NAME(S) AND ADDRESS(ES) <b>University of Illinois at Urbana-Champaign</b>				8. PERFORMING ORGANIZATION REPORT NUMBER	
9. SPONSORING/MONITORING AGENCY NAME(S) AND ADDRESS(ES) <b>The Department of the Air Force AFIT/CIA WPAFB, OH</b>				10. SPONSOR/MONITOR'S ACRONYM(S)	
				11. SPONSOR/MONITOR'S REPORT NUMBER(S)	
12. DISTRIBUTION/AVAILABILITY STATEMENT <b>Approved for public release, distribution unlimited</b>					
13. SUPPLEMENTARY NOTES <b>, The original document contains color images.</b>					
14. ABSTRACT					
15. SUBJECT TERMS					
16. SECURITY CLASSIFICATION OF:			17. LIMITATION OF ABSTRACT <b>UU</b>	18. NUMBER OF PAGES <b>150</b>	19a. NAME OF RESPONSIBLE PERSON
a. REPORT <b>unclassified</b>	b. ABSTRACT <b>unclassified</b>	c. THIS PAGE <b>unclassified</b>			

# SENSING MOLECULAR ADSORPTION THROUGH INTERFACIAL ELECTRON SCATTERING IN ATOM-SCALE JUNCTIONS

Patrick James Castle, Ph. D.  
Department of Chemistry  
University of Illinois at Urbana-Champaign, 2005  
Paul W. Bohn, Advisor

The goal of this work was to fabricate Au atom-scale junctions as the basis for robust, regenerable, nanostructured sensors to use with mass-limited samples for improved protection of health and safety. Atom-scale junctions were formed between two Au thin film electrodes. The inter-electrode gap was lithographically defined, and a microfluidic channel was aligned over the inter-electrode gap. The inter-electrode gap was reduced with electrodeposition, which was terminated at an atom-scale junction by setting a comparator to trigger a relay at a current corresponding to a junction conductance comparable to the conductance quantum. Based on conductance measurements and estimates from SEM images, atom-scale junctions were successfully formed. Lewis bases were introduced to atom-scale junctions, and the resulting alternating current impedance change was measured. For example, the interfacial scattering from chemisorption of 10 mM hexadecanethiol (HDT) on a  $2.6 G_0$  atom-scale junction caused a normalized impedance change of  $71\% \pm 1\%$ , with a noise level consistent with a population fluctuation of only 1 HDT molecule. To regenerate the device *in situ*, the junction was broken with a potential sweep and reformed with comparator-terminated electrodeposition. The atom-scale junction capability to measure small numbers of adsorption/desorption events makes a powerful case for pushing the limits of sensitivity for electrical measurements of single molecule events.

## ACKNOWLEDGEMENTS

I displayed two quotes above my desk in 51B Roger Adams Lab: “No matter what accomplishments you make, somebody helps you” (Wilma Rudolph) and “I can do all things through Christ who strengthens me” (Phil 4:13). Without the support of many great people and the gift of faith, I would not have achieved a PhD in analytical chemistry. I exclaim many thanks to my advisor, committee, colleagues, family, friends, and our awesome God!

My best friend and wife strengthened me daily with her selfless sacrifices and unconditional love. My daughters were a joyful distraction. My Mom provided a steady stream of prayers and communication. My Dad was engaged with my project, which enabled him to provide interesting research ideas. My parents ensured I was educated on God’s love for humanity, and the resulting faith has sustained me in challenging times. My brothers, sister in law, grandparents, and friends demonstrated pride in my pursuit of a PhD, which helped fuel my efforts.

My advisor, Professor Paul W. Bohn, was absolutely steadfast in providing essential support. His generous availability and expert professional guidance was critical for me to stay on schedule with the Air Force’s three-year timeline. My deep respect for Professor Bohn is reflected by the fact that I asked to rejoin his group for a PhD in 2002 after doing a MS summer project with him in 1994. The expertise of Dr. Jim Wentz (electronics), Dr. Bruce Flachsbart (fabrication), and Bill Lanford (fabrication) was critical to the success of my project. I also express my sincere appreciation for support from my committee (Prof. Andrzej Wieckowski, Prof. Ilesanmi Adesida, and Prof. Mark

Shannon) and group members, particularly Todd Williamson, Tim Rittenhouse, Xuejun Wang, and Qian Wang. Finally, with gratitude I acknowledge my high school chemistry teacher, Sister Jeanette Silvis, who taught me the basics of chemistry, and my Air Force Academy advisor, Dr. Don Bird, who strongly encouraged me and supported my selection for graduate school.

The United States Air Force Academy covered my tuition, and the Air Force Office of Scientific Research covered my research costs (Grant No. F49620-02-1-0381). The SEM work was carried out in the Center for Microanalysis of Materials, University of Illinois, which is partially supported by the U.S. Department of Energy under grant DEFG02-91-ER45439. The views expressed in this dissertation are those of the author and do not reflect the official policy or position of the United States Air Force, Department of Defense, or the U.S. Government.

## TABLE OF CONTENTS

<b>CHAPTER 1: BACKGROUND FOR ATOM-SCALE JUNCTIONS.....</b>	<b>1</b>
<b>1.1 Introduction.....</b>	<b>1</b>
<b>1.1.1 Atom-Scale Junction Formation.....</b>	<b>2</b>
<b>1.1.2 Quantized Conductance .....</b>	<b>3</b>
<b>1.2 Fabrication of Atom-scale Junctions.....</b>	<b>10</b>
<b>1.3 Structure of Atom-scale Junctions .....</b>	<b>13</b>
<b>1.4 Stability of Atom-scale Junctions .....</b>	<b>15</b>
<b>1.5 Contamination on Atom-scale Junctions .....</b>	<b>18</b>
<b>1.6 Modeling Atom-Scale Junctions .....</b>	<b>20</b>
<b>1.6.1 Tight-Binding Models.....</b>	<b>21</b>
<b>1.6.2 Free Electron Models.....</b>	<b>21</b>
<b>1.7 Characterizing Conductance Modes in a Single-Atom Junction .....</b>	<b>22</b>
<b>1.7.1 Elastic Scattering (conductance fluctuations vs preferred diameter) ...</b>	<b>23</b>
<b>1.7.2 Inelastic Scattering (phonons and heating) .....</b>	<b>26</b>
<b>1.8 Summary.....</b>	<b>27</b>
<b>1.9 Motivation.....</b>	<b>29</b>
<b>1.10 Outline of Work .....</b>	<b>30</b>
<b>1.11 References.....</b>	<b>31</b>
<b>CHAPTER 2: FABRICATION OF MICROFLUIDIC ELECTROCHEMICAL</b>	
<b>FLOW CELL .....</b>	<b>39</b>
<b>2.1 Introduction.....</b>	<b>39</b>

2.2 Experimental Methods .....	39
2.2.1 PDMS Microfluidics .....	41
2.2.2 Thin Au Film Electrode Fabrication.....	42
2.2.2.1 Photolithography with Metal Etching.....	43
2.2.2.2 Photolithography with Metal Lift-off.....	45
2.2.2.3 Photolithography and Electron Beam Lithography .....	45
2.3 Results and Discussion.....	46
2.3.1 Thin Au Film Electrode Fabrication (Photolithography) .....	46
2.3.2 Electron Beam Lithography (Nanotips).....	50
2.3.3 Microfluidic Channel.....	54
2.4 References.....	57
CHAPTER 3: ATOM-SCALE JUNCTION FORMATION .....	58
3.1 Experimental Methods .....	58
3.1.1 Reagents .....	58
3.1.2 Electrodeposition with $[Au^{+3}]$ .....	58
3.1.3 Directional Electrodeposition (etch/ deposit) .....	59
3.1.3.1 Resistor-Terminated Directional Electrodeposition .....	59
3.1.3.2 Comparator-Terminated Directional Electrodeposition.....	61
3.1.4 Junction Regeneration.....	63
3.1.5 Junction Characterization ( <i>I-V</i> curves) .....	63
3.2 Results and Discussion.....	63
3.2.1 Directional Electrodeposition (etch/ deposit) .....	63
3.2.1.1 Resistor-Terminated Directional Electrodeposition.....	66

3.2.1.2 Comparator-Terminated Directional Electrodeposition.....	69
3.2.2 Junction Characterization.....	70
3.2.3 Electromigration .....	76
3.2.4 Dendritic Growth.....	76
3.2.5 Junction Size.....	78
3.2.6 Junction Isolation.....	80
3.2.7 Junction Imaging .....	86
3.2.8 Junction Regeneration.....	89
3.2.9 Junction Stability .....	92
3.3 References.....	94
CHAPTER 4: SENSING WITH ATOM-SCALE JUNCTIONS.....	99
4.1 Introduction.....	99
4.2 Experimental Methods .....	103
4.3 Results and Discussion.....	103
4.3.1 Introducing Analyte.....	104
4.3.2 AC Impedance Measurements.....	105
4.3.3 Interfacial Electron Scattering .....	106
4.3.4 Interference with Chemisorption .....	110
4.3.5 Thiol Desorption.....	112
4.3.6 Noise .....	114
4.4 Conclusions.....	118
4.5 References.....	120



<b>CHAPTER 5: FUTURE DIRECTIONS.....</b>	<b>123</b>
<b>5.1 Junction Stability and Control .....</b>	<b>123</b>
5.1.1 Decrease Inter-Electrode Distance .....	123
5.1.2 Introduce Analyte with Less Force .....	124
5.1.3 Decrease Temperature.....	125
5.1.4 Mitigate Electrostatic Charge and Potential Difference .....	125
5.1.5 Reduce Au Nano-Particle Interference.....	127
5.1.6 Photochemical Growth .....	127
5.1.7 AC Monitoring of Junction Conductance .....	128
5.1.8 Referenced Electrodeposition .....	130
5.1.9 Two-Component Junction.....	132
<b>5.2 Imaging Junction .....</b>	<b>132</b>
<b>5.3 Sensing .....</b>	<b>133</b>
5.3.1 Noise Reduction.....	133
5.3.2 Threshold Junction Size for Sensing .....	135
5.3.3 Analytes.....	135
5.3.4 Chemical Isolation of Junction .....	136
5.3.5 Single Molecule Detection .....	137
<b>5.4 Molecular Electronics.....</b>	<b>137</b>
<b>5.5 References.....</b>	<b>139</b>
<b>AUTHOR’S BIOGRAPHY .....</b>	<b>141</b>

## **AUTHOR'S BIOGRAPHY**

Major Patrick James Castle was born in Sioux Falls, South Dakota. Pat has three brothers. He is married and has two daughters.

In 1993, Pat graduated from the United States Air Force Academy on the Dean's List with an accredited bachelor's degree in Chemistry. As an undergraduate, Pat held several leadership positions, including a Wing Staff position and coach of his squadron boxing and cross-country teams. In 1992, Pat was selected for the cadet summer research program at Edwards Air Force Base (AFB) in California, where he did research on a high-energy rocket fuel additive known as cubane. In 1994, Pat graduated with a master's degree in analytical chemistry from the University of Illinois, which included a summer project on Langmuir-Blodgett films with Professor Paul W. Bohn. Following graduate school, Pat attended a six-month Air Force Bioenvironmental Engineering school at Brooks AFB in Texas. From 1995 to 1997, Pat did OSHA and EPA related work at McClellan AFB in California.

From 1997 to 2000, Pat taught general, analytical, and environmental chemistry at the Air Force Academy in Colorado Springs. After serving as the course director for the environmental chemistry course, Pat was promoted to assistant professor. He assisted undergraduates with a research project on ionic liquids, which resulted in a poster session at the ACS conference. Pat led a team that developed an ethics program that was incorporated into the department curriculum. In 1999, Pat was recognized as the Outstanding Academy Educator in chemistry and was given the Wakin Character Award.

From 2000 to 2002, Pat was the Chief Bioenvironmental Engineer for Incirlik Air Base in Turkey, serving as the in-country expert on OSHA and EPA related matters, as well as chemical and biological agent protection. Two notable additional duties were executive officer for the hospital commander and command briefer for the wing commander. In 2002, Pat was recognized as the top officer in the hospital and the best Bioenvironmental Engineer in Europe.

From 2002 to 2005, Pat did his PhD work under Professor Paul W. Bohn, in pursuit of an atom-scale junction based sensor. Following the completion of this PhD, Pat will return to the Air Force Academy for another teaching assignment.

## CHAPTER 1

### BACKGROUND FOR ATOM-SCALE JUNCTIONS

#### 1.1 Introduction

The purpose of this section is to give a brief background on the research surrounding the study of atom-scale junctions, concluding with the motivation and outline of this thesis research. The study of atom-scale junctions is part of the field of nanoscience, where ‘nano’ refers to the nanometer scale.<sup>1</sup> Atom-scale junction research takes nanoscience to the ultimate size limit, the size of atoms and molecules. Atom-scale junctions are of great interest conceptually, because they are the smallest junctions which can be fabricated, and practically, because they can be used to fabricate nanostructured devices.<sup>1-20</sup> The goal of our research was to fabricate Au atom-scale junctions as the basis for robust, regenerable, nanostructured sensors to use in conjunction with mass-limited samples.<sup>21</sup> If such a device could be engineered into a miniature system, broad response would combine with low mass limits of detection, auguring potential improvements for protection of health and safety. For example, a lower level of sensitivity would save lives through early detection of chemical agents like dimethylaminoethoxy-cyanophosphine oxide (Tabun nerve agent), which Iraq used on Iran in 1984.<sup>22</sup> Atom-scale junction research is still a long way from large-scale fabrication of atomically engineered devices and circuits. The main barriers are fabrication costs for giga-component circuits and maintaining stability at room temperature. Regardless, atom-scale junction research may discover new material properties and principles to be exploited.

### 1.1.1 Atom-Scale Junction Formation

Atom-scale junctions are formed primarily with one of three methods: mechanically controllable break junctions (MCBJ), stretching scanning tunneling microscopy (STM) tips, and electrochemical deposition. The exponential dependence of the tunneling current allows only the closest atom of the STM tip, fractured MCBJ surface, or electrochemically deposited Au to ‘see’ the opposite electrode.<sup>1</sup> The MCBJ method typically uses a piezo element to bend an elastically deformable substrate, bending a metallic micro-wire or microfabricated bridge on the substrate. Through bending, the wire is broken and reconnected to form atom-scale junctions.<sup>9,11,16,20,23</sup> With the STM method, the metal tip is indented into a sample metal and retracted to form an atom-scale junction.<sup>6,7,10,19</sup> Piezoelectric ceramics allows control of the relative position of the STM tip with subnanometer accuracy. With electrochemical deposition methods, Au is deposited between two closely spaced electrodes on a substrate, and electronic feedback is used to terminate the electrodes at a current equivalent to an atom-scale junction.<sup>2,7,10,18,21,24-26</sup>

The MCBJ and STM methods are vulnerable to vibrational disturbances since these methods are mechanical and the atom-scale junctions are not resting on stabilizing substrates. With the STM method the atom-scale junction is pulled away from the sample. The MCBJ bends a wire mounted to a substrate, but the atom-scale junction area is typically not resting on the substrate. Tao *et al.* decreased the junction’s vulnerability to vibrational disturbance by electrochemically growing, either by electrodeposition<sup>2</sup> or electrolysis,<sup>18</sup> atom-scale junctions across a substrate. Therefore, the electrochemical

methods are better suited for handling the disturbances associated with a mobile field detection system. Furthermore, the electrochemical methods of fabricating atom-scale junctions could be feasibly integrated into a miniature detection device, unlike the STM method. However, the MCBJ and STM methods allow better control and efficiency than electrochemical methods when forming atom-scale junctions that demonstrate quantized conductance.

### 1.1.2 Quantized Conductance

For a proper description of the resistance in an atom-scale junction, the wave nature of the electrons must be considered because a continuum (bulk) description of the electrical and mechanical properties of bulk metal breaks down at the atom-scale. If the junction is composed of a single atom, the electrical and mechanical properties of the junction are dominated by the nature of the atom, allowing for quantitative comparison of theory and experiment.<sup>1</sup> The mechanical properties of the atom-scale junctions show pronounced quantum effects, since the Fermi wavelengths of metals are comparable to the size of the atom. In computer models, conductance modes affect the cohesive force, which impacts mechanical stability. Experiments have measured the yield strength of Au atom-scale junctions from about twice to more than an order of magnitude larger than bulk Au.<sup>27,28</sup> Au can be stretched into conducting chains of individual atoms with a conductance close to  $1 G_0$ , which is known as the conductance quantum and equal to  $2e^2/h$ .<sup>15</sup> The resistance of a conductor does not scale proportional to length (Ohm's Law) when electrons traverse an atom-scale junction ballistically, meaning the length and diameter of the junction is shorter than the electron mean free path (Figure 1.1).

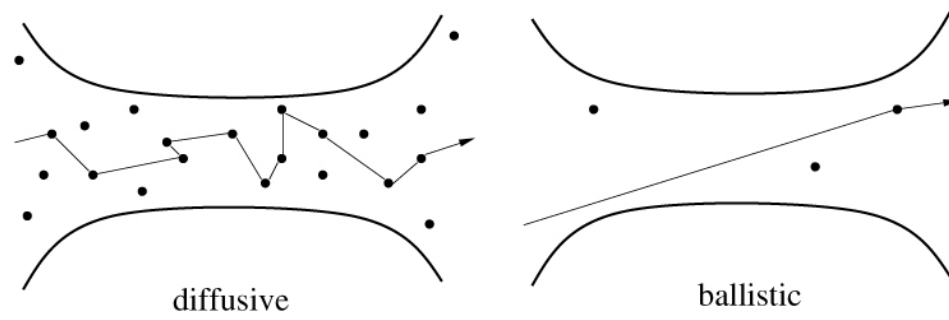


**Figure 1.1:** Illustration of a diffusive and ballistic atom-scale junction. For a ballistic junction, the length and diameter of the junction is shorter than the electron mean free path.<sup>1</sup>

In 1957, Landauer proposed the notion that electrical conductance is equivalent to the transmission probability for incoming waves, explaining the quantized conductance that would be measured in atom-scale junctions nearly three decades later.<sup>29,30</sup> Landauer was the first to outline the general scattering formalism for a two reservoir configuration.<sup>1,29,31</sup> If a voltage is applied between the reservoirs connecting a perfect conductor like a Au atomic chain (Figure 1.2), a current will occur from the electron population imbalance between the mode moving from the left (set by the Fermi distribution on the left electrode,  $f_L$ ) and the mode moving from the right (set by  $f_R$ ).

$$I = 2e/h \int d\varepsilon (f_L(\varepsilon) - f_R(\varepsilon))$$

The spin-degeneracy is responsible for the factor 2 in this relationship, while the electron charge ( $e$ ) is 1.6E-19 C and Planks constant ( $h$ ) is 6.62E-34 J\*s. At a temperature of 0 K,  $f_L(\varepsilon)$  and  $f_R(\varepsilon)$  are step functions, leading to  $I = GV$  with  $G = 2e^2/h$ .

For metal atom-scale junctions, the Landauer expression ( $G = 2e^2/h \sum \tau_n$ ) is applicable because the Fermi wavelength ( $\lambda_F$ ) of metals is comparable to the atomic diameter. The transmission probability for each of the metal conducting modes is represented by  $\tau_n$ . For a perfect conductor with  $\tau_n$  equal to 0 or 1 for all conductance modes, the conductance will be an integer multiple of the conductance quantum,  $G_0 = 2e^2/h$ . Therefore, a perfect single mode conductor has a finite resistance of  $h/2e^2 \cong 12.9 \text{ k}\Omega$ , as opposed to a perfect macroscopic conductor that is expected to have zero resistance. For most metal atom-scale junction with a cross section of only one atom, the estimated number of conductance modes is between 1 and 3.<sup>1</sup> The number of conductance modes is based on the valence orbital structure of the atoms. A gold atomic chain is a one-dimensional conductor with a single occupied mode.



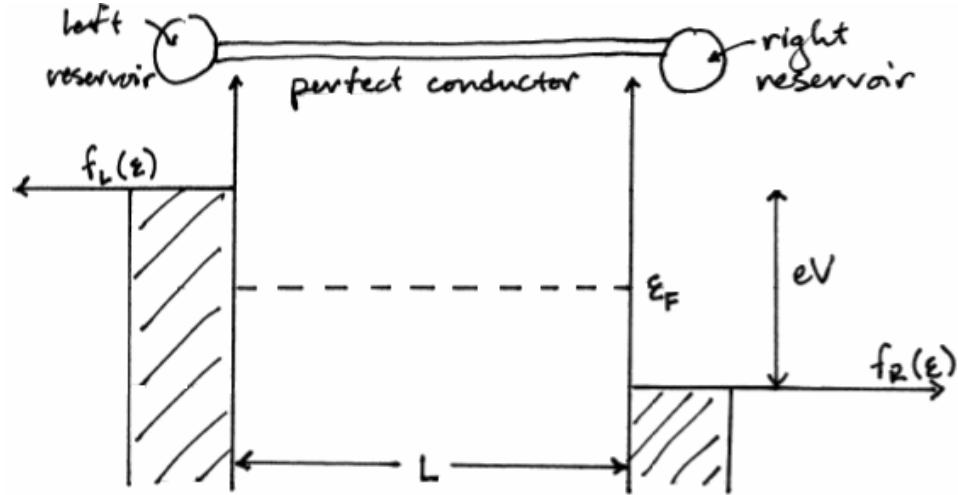


**Figure 1.2:** Schematic describing quantized conductance for a perfect conductor between two reservoirs. If a voltage is applied between the reservoirs, a current will occur from the electron population imbalance between the mode moving from the left (set by the Fermi distribution on the left electrode,  $f_L$ ) and the mode moving from the right (set by  $f_R$ ), represented by  $I = 2e/h \int d\epsilon (f_L(\epsilon) - f_R(\epsilon))$ . For a perfect conductor with a transmission probability of 0 or 1 for all conductance modes, the conductance will be an integer multiple of the conductance quantum ( $G_0$ ), which is equal to  $2e^2/h$ .<sup>1,31</sup>

In 1986, soon after the invention of STM, quantized conductance was first measured in atom-scale junctions.<sup>30</sup> For a typical STM method experiment, the STM tip is embedded, and then the conductance is recorded while the STM tip is stretched away from the metal sample. Just before breaking, atom-scale junctions are formed and recognized by the conductance decreasing in a stepwise fashion. The steps are on the order of the conductance quantum,  $G_0 = 2e^2/h$ . Quantized conductance is observed when junction length is less than the electron mean free path in Au ( $l = 3.8$  nm) and the junction thickness is comparable to the Fermi wavelength for Au ( $\lambda_F = 0.52$  nm).<sup>1,4,7,8,10,11,15,17,32</sup> For example, Ohnishi *et al.* measured conductance while forming atom-scale junctions with an STM and observed that a junction composed of two parallel rows of Au atoms has a conductance of  $\sim 2 G_0$  and a width of 0.58 nm, based on nearest-neighbor spacing.<sup>15</sup>

When measuring the conductance during the formation of atom-scale junctions, each conductance curve is unique due to the many possible atomic configurations (Figure 1.3).<sup>13</sup> However, the last plateau of the conductance curve is characteristic of each metal, implying that the conductance through a single atom is determined by the electronic structure of that atom.<sup>33</sup> Noble metals like Au and Ag typically exhibit a constant last plateau very close to  $G_0$ , while the last step is sloped for Al and Pb. Furthermore, all of the conductance steps are not an integer multiple of the conductance quantum ( $nG_0$ ) although Au has a strong preference for integer multiples of  $G_0$  between 1 and 3 (Figure 1.4).<sup>13</sup> Above  $3 G_0$ , several partially open modes exist due to scattering in the atom-scale junction.<sup>34</sup> Conductance and force measurements were combined to demonstrate atomic

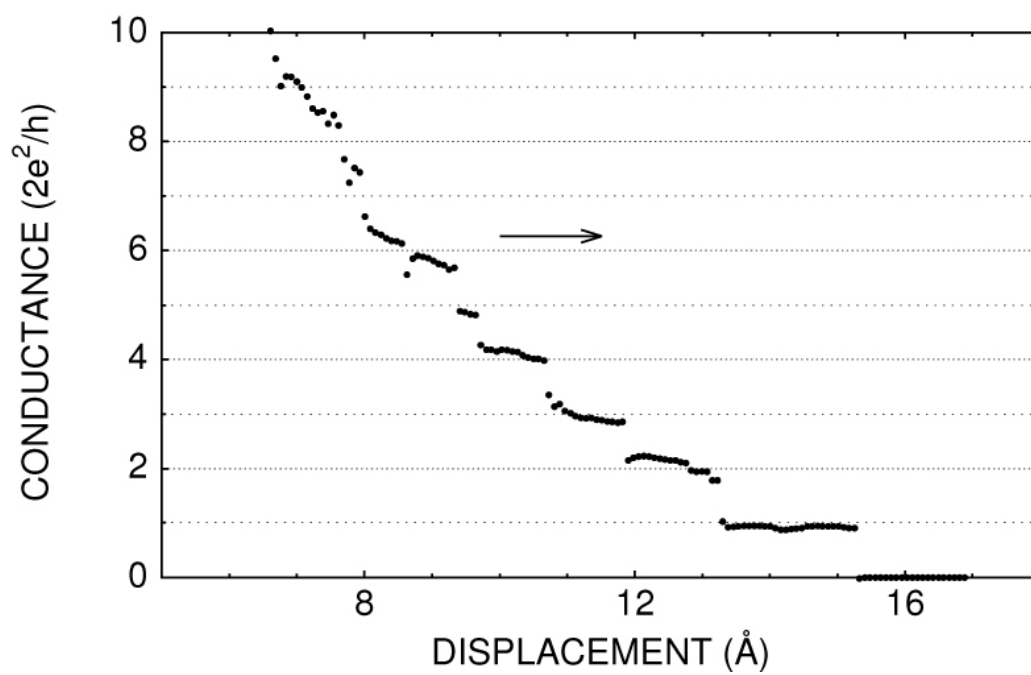


**Figure 1.3:** Curve for recording the conductance while retracting a STM tip after pressing it into a clean gold surface. Current and voltage measurements were taken over approximately 20 ms at room temperature in a UHV environment.<sup>1,13</sup>

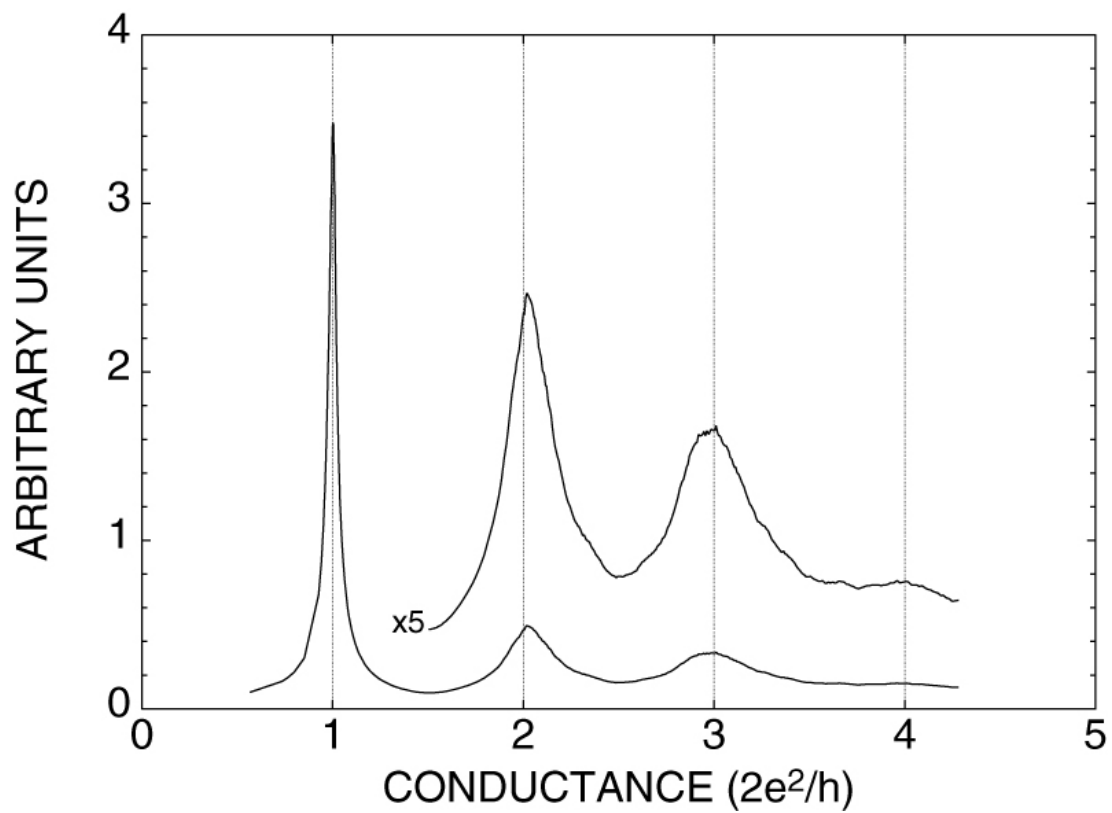


**Figure 1.4:** Histogram for atom-scale junctions formed by retracting a STM tip after pressing it into a clean Au surface (6562 data points). Measurements were taken at room temperature in a ultra-high vacuum (UHV) environment, corrected for an effective series resistance of  $150\Omega$ .<sup>1,13</sup>

rearrangements at the conductance steps by showing that jumps in conductance correspond to jumps in force.<sup>35</sup>

For a typical transport experiment, the atom-scale junction is connected to macroscopic electrodes that act as ideal electron reservoirs in thermal equilibrium. The assumptions are that phase-coherence is preserved across the atom-scale junction and inelastic scattering is restricted to the electron reservoirs. Such assumptions would be strictly valid at a temperature of 0 K and only for electrons at the Fermi energy. In reality, coherent electron propagation through the atom-scale junction may be limited by inelastic scattering due to electron-phonon and electron-electron collisions. Perfect coupling between the leads and the electron reservoirs would set the distribution of the incoming modes, as determined by the Fermi distribution on the corresponding electrode. With a probability of one, the outgoing modes would be transmitted into the electrodes. However, if the atom-scale junction is weakly coupled to the leads, strong Coulomb interactions (charging effects) can suppress electron transport.

## **1.2 Fabrication of Atom-scale Junctions**

The study of the quantum regime requires control of contact diameters comparable to the Fermi wavelength. The STM and MCBJ methods allow more control over contact size than electrochemical deposition methods. Therefore, the study of atom-scale junction conductance typically involves techniques that mechanically form and break metal junctions. In molecular dynamics simulations with Ni, Pd, Pt, Cu, Ag, and Au, only Au and Pt formed a single atom junction.<sup>1,36</sup> Once the electrodes are just in contact (single-atom), a step-wise conductance results from an increase in the atom-scale junction diameter. This interpretation is supported by classical molecular dynamics

simulations and experimentally with simultaneous measurements of the conductance and the force in the atom-scale junction. Since the atomic arrangement varies in the formation of each atom-scale junction, the conductance curves vary. For some monovalent metals (Au, Cu, Ag, Li, Na and K), the step height is close to a multiple of  $G_0$  for the first three conductance steps, with the  $1 G_0$  step being the most reproducible. When the atom-scale junction changes size by approximately the area of one atom, the conductance changes by  $\sim 1 G_0$ . Backscattering from defects near the junction may be the primary cause for deviations from perfect quantization.

The conductance of the last plateau is a result of a single-atom junction, as confirmed by force measurements, model calculations, and high-resolution transmission electron microscope (HR-TEM) images. This last conductance plateau is characteristic of the metal, and only Au and Ag have a sharply defined conductance of  $\sim 1 G_0$  for the last plateau.<sup>33</sup> For Au, the last plateau would have a conductance less than  $1 G_0$  if a single atom was not sufficient to open a conductance mode.<sup>1</sup> For confirmation, Ohnishi *et al.* imaged between two and five Au atom chains at room temperature with a UHV HR-TEM, and the conductance was simultaneously measured (Figure 1.5). By dividing the total conductance by the number of atomic chains, each chain would have a conductance of  $\sim 1 G_0$ .<sup>15</sup> Although the conductance for all metals is not strictly quantized (Figures 1.3 and 1.4), it is still determined by quantum phenomena and carried by a limited number of modes. The quantum nature is especially apparent in monovalent metals in which the first three modes show a tendency to open or close one at a time as the junction cross sectional area changes.

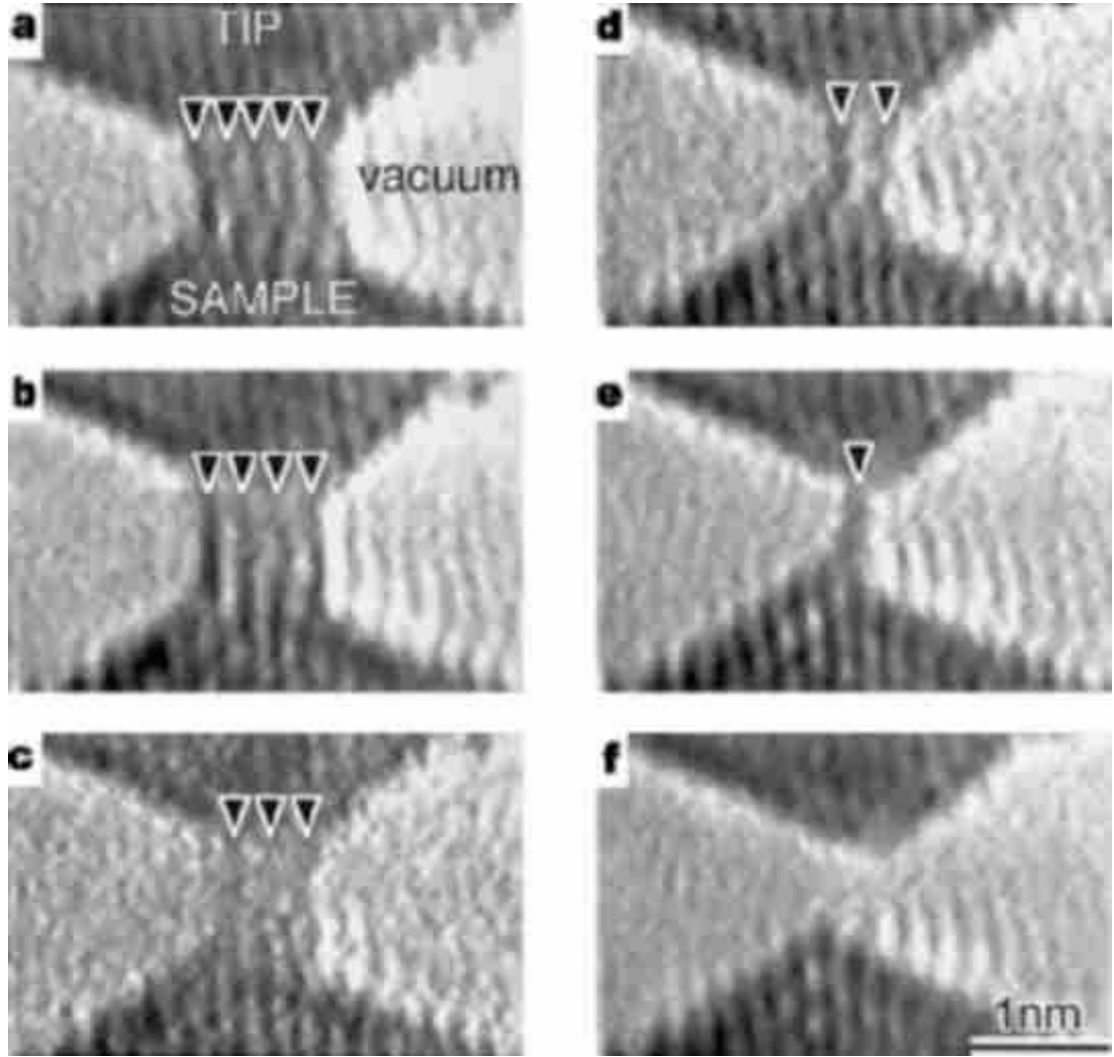


**Figure 1.5:** TEM images of a Au atom-scale junction as STM tip is withdrawn from the sample. Going from image (a) to (e), notice the number of Au chains is reduced until rupturing (f). The atom-scale junction is (e) is thought to be a double strand overlapping in the viewing direction because the conductance is  $2 G_0$ . From (a) to (f), the images are taken at 0, 0.47, 1.23, 1.33, 1.80 and 2.17 s.<sup>15</sup>

### 1.3 Structure of Atom-scale Junctions

HR-TEM in a UHV environment has been used to resolve individual Au atoms in a chain. An intense electron beam melted two adjacent holes in a Au thin film and then thinned the area between these holes to form a Au atomic chain (Figure 1.6).<sup>15</sup> The Au atom distance in the chain was 0.35–0.40 nm, considerably larger than the nearest neighbor spacing in bulk Au (0.288 nm) and model predictions based on electron cloud stabilization. Possibly, the single strand Au atom chain was stabilized by the inclusion of atoms such as C or O.<sup>1,37,38</sup> Contamination is present even in high vacuum experiments, and contaminants will only bind strongly to the low-coordination Au atoms in the chain. Oxygen is highly suspect because it is not resolved in the HR-TEM, and calculations demonstrate a Au-O-Au-O chain with a Au-Au distance close to those observed in the HR-TEM image. In addition, a Au-O-Au-O chain conducts with a single mode. However, with the same two-hole experimental technique, a new generation defocus-imaging modulation processing electron microscope observed Au-Au distances of 0.25–0.29 nm, comparable to the nearest neighbor spacing in bulk Au.<sup>1,39</sup> A different experiment used a miniature STM inside a HR-TEM (regular vacuum) to image an atomic chain between an STM tip and the sample, resulting in Au atom spacing of  $0.27 \pm 0.02$  nm.<sup>40</sup> Surprisingly, the conductance dropped to zero when the atom-scale junction was stretched from a multi-atom cross-section to a single-atom cross-section. In addition, the Au atom chains were bent even while the tip was stretched, and unusually long chains (up to 10 atoms) were observed for comparatively long times. Possibly, CO is binding to the Au chain and in turn making it an insulator, introducing bends, and stabilizing the atomic chain.<sup>38</sup>



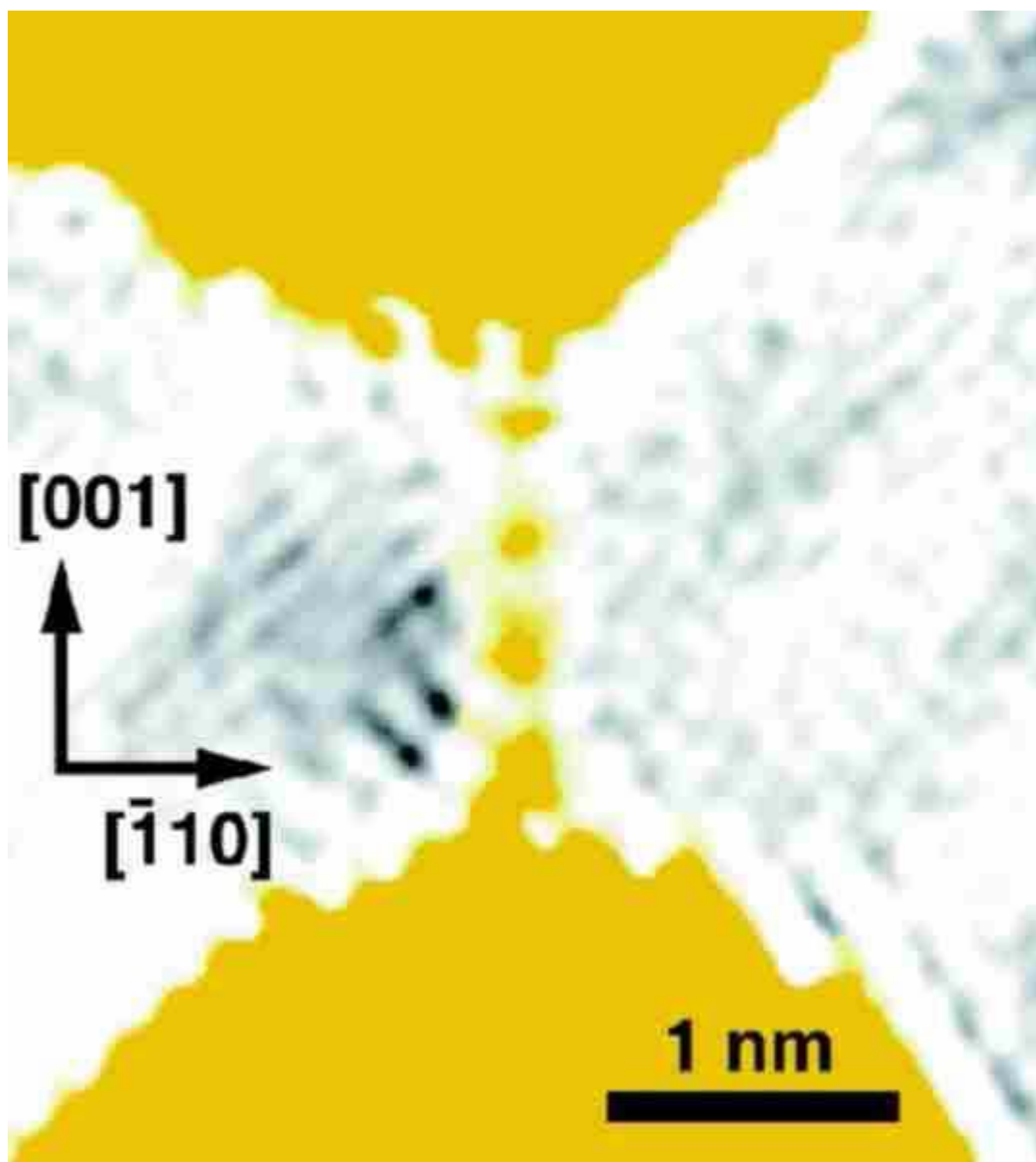


**Figure 1.6:** HR-TEM image of a Au atomic chain, where individual atoms are resolvable (4 gold dots). An electron beam was used to bore two holes in a thin Au film, followed by thinning of the area between these holes to form an atomic chain. The atomic spacing in the chain, 0.35 – 0.40 nm, is much larger than the nearest neighbor distance in bulk Au (0.288 nm).<sup>15</sup>

## 1.4 Stability of Atom-scale Junctions

The cross section minimum typically controls the conductance and concentrates the stresses, intertwining the mechanical stability and electronic properties of atom-scale junctions. This relationship was demonstrated by measuring the conductance and force during the thinning and thickening of an atom-scale junction.<sup>35,41,42</sup> In **Figure 1.7**, the conductance jumps are strongly correlated with the mechanical relaxations.

As a metastable structure, atom-scale junctions are subject to thermal diffusion of atoms, which can ultimately break the junction.<sup>1</sup> According to molecular dynamics calculations, an atomic chain is stable for only nanoseconds at 300 K, but an atomic chain would have a lifetime of hours to days at 4.2 K. However, these model calculations are in conflict with experimental results at room temperature, where atom-scale junctions have been reported with a surprising stability, lasting for an hour or more.<sup>10,18,21</sup> This enhanced stability is probably due to contaminants like CO and O, which could provide stronger binding and inhibit the surface diffusion of atoms.<sup>38</sup> An atomic chain with O between the Au atoms would still have a single conducting mode. In addition, methylthiol was inserted into a gold chain, and the chain still contained just a single conducting mode.<sup>37</sup> Adsorbates lower the tunneling barrier, so a conductance below  $1 G_0$  for a Au atom-scale junction is probably a result of contamination.<sup>30</sup> The proposed effect of impurities has been confirmed by *ab initio* calculations which self consistently included the applied bias voltage.<sup>43</sup> Fast scan  $I$ - $V$  curves (within 20  $\mu$ s) at low potential allow metals like Au to be studied even with a limited stability range.<sup>44</sup>

For Au, the stability is also enhanced at integer multiples of  $G_0$ . With high-vacuum room temperature experiments, multiples of  $G_0$  are preferentially formed because

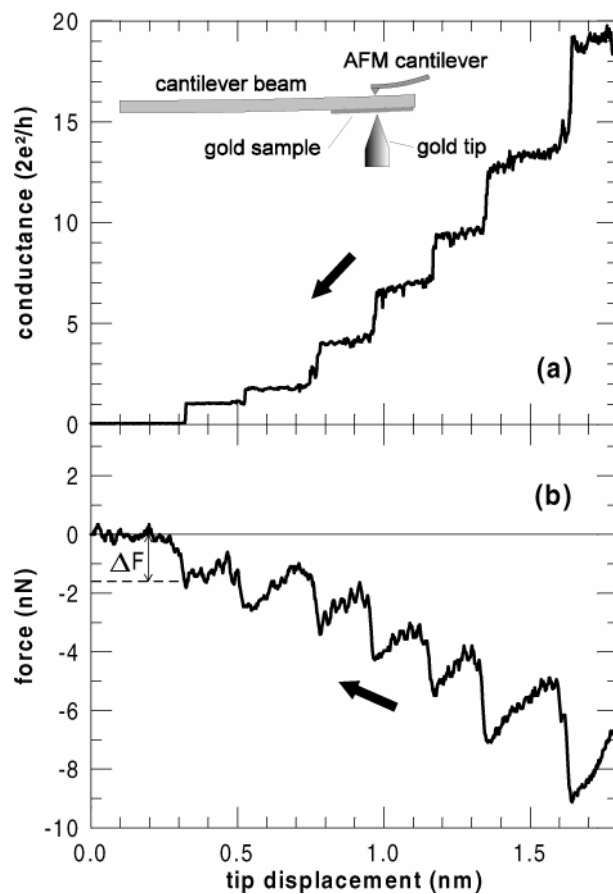


**Figure 1.7:** Plots from measuring the conductance and force simultaneously at 300 K while the Au STM tip was displaced from the Au sample, forming various atom-scale junction sizes. An AFM cantilever was mounted on a cantilever beam and used to measure the deflection of the sample (see inset). The force is directly proportional to the cantilever beam deflection. The single atom junction break force ( $\Delta F$ ) is labeled in (b).<sup>35</sup>

at room temperature atoms are able to diffuse to preferred atomic configurations.<sup>1,45</sup> With an electrochemical fabrication technique, Li *et al* concluded that integer multiples of  $G_0$  are also more stable.<sup>18</sup> Perhaps filling of the quantum modes stabilizes the atom-scale junction. For Au, the first conductance step ( $1 G_0$ ) is especially robust, surviving current-induced forces from applied bias voltage up to 1.9 V at room temperature before breaking.<sup>21,46-48</sup> The calculated force required to break a Au atomic chain is comparable to the experimental force required to break a Au atomic chain with bias of 1.5 - 2.0 V.<sup>49</sup> Further calculations demonstrate that current-induced forces weaken the atomic chain.<sup>50</sup> The atomic chain is ruptured as a consequence of heat generated by the current and primarily by electromigration of Au atoms. To rupture the atomic chain at 4.2 K rather than room temperature, only 16% greater potential was required, confirming that electromigration has more impact than thermal diffusion for rupturing the atom-scale junctions.<sup>47</sup>

Atom-scale junctions are stronger per volume than bulk metal, likely due to better crystallinity (less defects) and less impurities.<sup>1</sup> Using an STM with a force sensor, the yield strength of a Au atom-scale junction was measured at  $\sim 20$  GPa.<sup>27</sup> By fitting the data with a surface force contribution, the “intrinsic” yield strength of the Au atom-scale junction is  $\sim 6$  GPa, which is more than an order of magnitude larger than the bulk yield strength for Au (200 MPa) and comparable to the ideal yield strength of metals with no defects (2-4 GPa). In a separate experiment (Figure 1.7), the break force ( $1.5 \pm 0.3$  nN) of Au atomic chains was about twice as large as the force required to break individual bonds in bulk Au (0.8 – 0.9 nN).<sup>28</sup> At 300 K, Au requires a slightly larger break force than the other monovalent metals.<sup>27</sup> At higher temperatures, atom-scale junctions will

have better crystallinity (less defects), improving the probability of quantized conductance and the strength of the junction.<sup>41</sup>

### 1.5 Contamination on Atom-scale Junctions

Contaminants adsorbed to the surface of the electrodes could interfere with the formation, characterization, and sensing capability of atom-scale junctions. With electrochemical deposition methods, contamination could be limited by cleaning the electrodes in piranha solution (3 parts H<sub>2</sub>SO<sub>4</sub>/ 1 part H<sub>2</sub>O<sub>2</sub>) before forming junctions electrochemically in microfluidic channels filled with electrolyte.<sup>21</sup> The MCBJ method limits contamination by breaking the metal on the substrate in a UHV environment, which exposes clean fractured surfaces.<sup>1</sup> The STM method limits contamination by repeatedly crashing the tip on the sample surface, pushing any adsorbates aside. By performing the STM and MCBJ experiments at liquid helium temperatures (4.2 K), the surfaces would not be subject to gas contamination.

Contamination adsorbed on the junction typically increases the resistance due to interfacial scattering; therefore, an atom-scale junction conductance  $< 1 G_0$  could be an indication of contamination.<sup>30</sup> In addition, a gold atom-scale junction  $I$ - $V$  curve that is slightly non-linear between 0.5 V and 1.0 V is likely a reflection of contamination, as concluded by Hansen *et al.* after comparing measurements taken in air versus UHV (Figure 1.8).<sup>44</sup> Even under widely different environments and cleaning procedures, Au atom-scale junction  $I$ - $V$  curves are quite linear below 0.5 V, in large part because Au has a low reactivity and is easily cleaned. In a separate experiment by Li *et al.*, the conductance was gradually suppressed only after intentionally increasing the concentration of reactive molecules in the atmosphere; however, the  $1 G_0$  step was

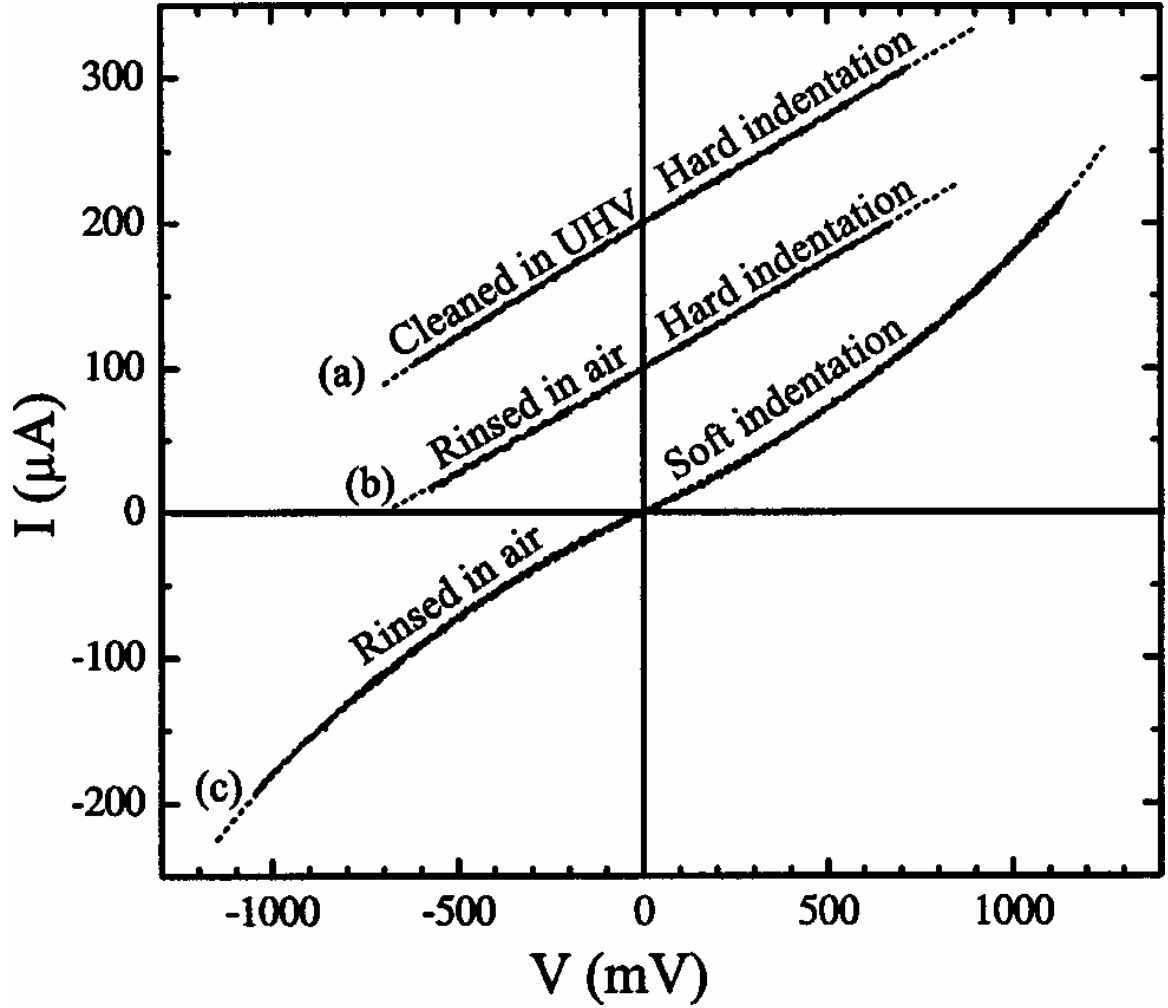


**Figure 1.8:**  $I$ – $V$  curves for Au atom-scale junctions formed at room temperature with the STM formation method: (a)  $1.95 G_0$ , (b)  $1.91 G_0$ , and (c)  $1.72 G_0$ . The samples were prepared with different procedures (labeled), which apparently impacts the amount of contamination on the contacting surfaces. For clarity, the  $I$ – $V$  curves are each separated by  $100 \mu\text{A}$ .<sup>44</sup>

unchanged.<sup>10</sup> For experiments with a higher reactivity than Au, clean UHV or cryogenic conditions are necessary to obtain reproducible results.<sup>1</sup>

## 1.6 Modeling Atom-Scale Junctions

Molecular dynamics (MD) simulations have modeled the STM and MCBJ atom-scale junction fabrication methods.<sup>1</sup> Classical MD simulations provide insight into atom-scale properties by modeling the interactions of the individual atoms. However, classical MD simulations are not reliable for metallic atoms with low coordination, like in single-atom metal junctions or metal atomic chains. MD simulations are computationally intensive; therefore, different aspects of the system are modeled separately.<sup>51</sup> For example, the conductance can be determined based solely on the calculated structure, while neglecting the electronic effects.

MD simulations expose mechanically drawn metallic constrictions that are generally non-adiabatic (cross-section does not gradually change along length of junction) and have defects like surface rugosity, stacking faults, vacancies, and local disorder.<sup>1</sup> Atom-scale junctions larger than a few atoms in thickness can have backscattering caused from defects and a non-adiabatic junction structure. These conditions cause partially open conductance modes and non-integer multiples of  $G_0$ .<sup>13,52</sup> In addition, a non-homogenous defect density distribution in the junction could cause the conductance to be controlled by a section of the junction that is not the narrowest.<sup>53</sup>

In considering electronic effects, the atomic structure can be completely ignored like in free electron (FE) models or assumed fixed like in tight-binding (TB) models.<sup>1</sup> By adjusting the junction cross section and electron density according to the type of atom, FE models produce nearly perfect conductance quantization for simple metals with cross

sections comparable to the Fermi wavelength.<sup>13,54</sup> With TB models, conductance quantization is not as common when using realistic models for the junction atomic structure.<sup>53</sup>

### **1.6.1 Tight-Binding Models**

For studying the conductance of a finite TB system, the system considered was an atom-scale junction connected between two semi-infinite systems (leads). Using a MD simulation with a TB scheme, theorists have determined that structural atomic rearrangement is related to the abrupt changes in conductance for atom-scale junctions.<sup>1,13,23,34,53</sup> The TB model was used to calculate the conductance of an atomic configuration, using atomic coordinates from classical MD simulations. However, this calculation does not represent the electronic structure of the metals accurately, because the calculation utilizes only one atomic orbital (1s). Regardless, in agreement with experimental data, the TB model for a single-atom junction predicted one conductance mode for monovalent metals, with nearly perfect transmission up to a bias voltage of about 1 V.<sup>55,56</sup>

### **1.6.2 Free Electron Models**

The conductance in an MD simulation can also be calculated with the FE model, resulting in a comparable conductance to the TB model.<sup>1,53</sup> However, the FE model depends only on the cross-section of the junction, rather than the precise atomic structure. The FE model is not able to take into account structural defects but can consider scattering due to internal disorder. In the FE model, electron-electron interaction is not considered, and the quantized conductance is a result of lateral electronic confinement. Ignoring the atomic nature of metals is the fundamental deficiency of the FE model;



therefore, experimental results should not be interpreted exclusively with the FE model, which is most reliable for monovalent metals.

For an FE model, conductance quantization is observed, if the length and thickness of the junction is smaller than the electron mean free path (ballistic), and the cross section is a smooth function of the longitudinal coordinate (adiabatic).<sup>1</sup> For a simplified model of an atom-scale junction, a set of parabolic one-dimensional subbands represent the electron states. As the thickness of the junction decreases, the subband separation increases. If the interface-derived connection scattering is ignored, the conductance is simply based on the subbands that cross the Fermi level, with each subband contributing  $2e^2/h$ . However, the conductance quantization is suppressed by backscattering caused by boundary roughness and internal junction defects, causing the conductance steps to shift downward.<sup>52,57</sup> In addition, internal defects in the junction causes backscattering that smears single quantized conductance steps. This suppression of the conductance results in partially open modes and non-integer multiples of the conductance quantum.

### **1.7 Characterizing Conductance Modes in a Single-Atom Junction**

The conductance of an atom-scale junction is predominantly determined by the properties of the narrowest part of the junction.<sup>1</sup> For a single-atom junction, the chemical nature of the atom determines the number of conductance modes. The transmission probability for the mode(s) is impacted by the lead connection. The transmission probability will be one if the connection does not have defects and surface corrugations close to the single-atom junction. Moving to larger junctions, any sudden variation in the cross section causes the electron wave to be partially reflected. The scattering due to

surface roughness is likely suppressed at higher temperatures that promote a smoother surface and a more gradual variation of the cross-section along the length of the junction. The conductance is altered by the extent that the partially reflected wave moves back through the junction (backscattering). As the scattering occurs further from the atom-scale junction (in the diffusive Au banks), the partially reflected wave has a lower probability of returning to the junction for conductance changing wave interference.

Conductance measurements provide a sum of the contributions from all conductance modes.<sup>1</sup> When the conductance is  $> 1 G_0$ , more than a single mode contributes. With a conductance of  $1 G_0$ , several partial modes could be contributing rather than a single mode. Furthermore, a poorly transmitted single mode(s) could result in a conductance  $< 1 G_0$ . By analyzing the subgap structure, mode information can be extracted, theoretically. For a single-atom junction, the number of valence orbitals of the single atom determines the number of conductance modes. The *sd* single-atom junctions have 5 or 6 conductance modes. Single-atom junctions for monovalent metals like Au and Ag sustain a single conductance mode with nearly perfect transmission ( $\sim 1 G_0$ ).<sup>58</sup> For junctions up to three to six atoms in cross section, the conductance modes have a strong tendency to completely open one after the other, while larger channels have several partially open channels. Therefore, conductance quantization is only strictly applicable to monovalent metals with a junction cross-section less than three to six atoms.

### **1.7.1 Elastic Scattering (conductance fluctuations vs preferred diameter)**

Interference between backscattered electron waves in atom-scale junctions gives rise to conductance fluctuations.<sup>1,58</sup> For systems with scattering centers near the junction, the electrons have many possible backscattering trajectories and all partial waves sum up

coherently. For each unique configuration of scattering centers, the conductance is slightly different, and the root mean-square amplitude of the conductance fluctuations is a universal value,  $dG_{rms} \cong e^2/h$ .

To describe the interference that causes conductance fluctuations, the junction is modeled as illustrated in **Figure 1.9**.<sup>1</sup> The junction is between diffusive banks where electrons undergo scattering events from defects (**Figure 1.1**). The junction is evaluated in terms of transmission and reflection values for the conductance modes. An electron wave is transmitted into a certain mode of the junction with probability amplitude  $t$ , and the diffusive medium reflects part of the wave back into the same mode with probability amplitude  $a$  ( $\ll 1$ ). Upon reaching the junction, this back-scattered partial wave is reflected again with probability amplitude  $r$ . The original transmitted wave interferes with this reflected partial wave, and the interference is dependent on the phase of the reflected partial wave. The phase is influenced by the bias voltage, which changes the electron velocity across the junction. Therefore, the bias voltage impacts the interference and in turn the transmission probability (conductance). The conductance fluctuations from electron wave interference is eliminated when  $t = 0$  or  $r = 0$ .<sup>58</sup>

For a Au 1  $G_0$  junction, conductance fluctuation and shot noise experiments conclude that the conductance is determined by one nearly perfect transmission mode.<sup>1</sup> This is supported by a histogram of atom-scale junction conductance measurements with a maximum near 1  $G_0$ .<sup>58</sup> The conductance fluctuation and shot noise experiments have the next maximum at 2  $G_0$ , but the next conductance histogram maximum is at 1.8  $G_0$ . The non-integer conductance measurements are likely due to a combination of backscattering (defects) and preferred atomic configuration (diameter). The latter is

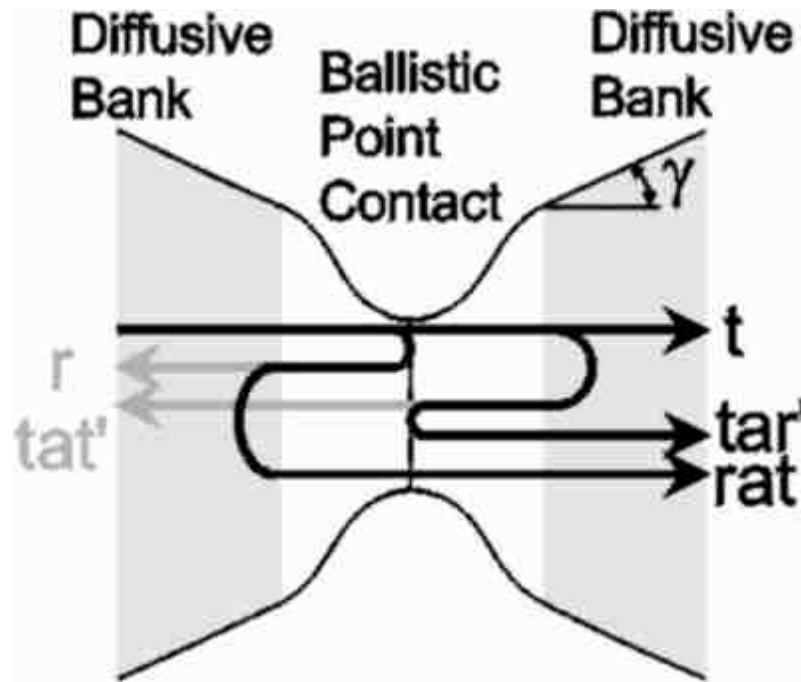


**Figure 1.9:** Schematic modeling the atom-scale junction as a junction (light) between two diffusive regions (gray). The dark lines are the electron wave paths that interfere and contribute to the conductance fluctuations.<sup>1</sup>

supported by *ab-initio* calculations (includes nuclear and electronic degrees of freedom) for a double strand of Au atoms, resulting in a conductance of  $1.79 G_0$  for two conductance modes.<sup>1,59</sup> Furthermore, if backscattering from defects near the junction were primarily responsible for shifting from  $2 G_0$  step to  $1.8 G_0$ , the  $1 G_0$  step could be expected to decrease to  $\sim 0.8 G_0$ . If the  $1 G_0$  step is from a single-atom junction, only one atomic configuration is possible. Since the  $1 G_0$  step histogram data was not significantly impacted, the  $2 G_0$  shift is likely due to a preferred atomic configuration for the double stranded Au junction.

By measuring the junction diameter with TEM while measuring the conductance, the dependence of the conductance on the junction diameter was evaluated.<sup>1,32</sup> The STM method was used to form junctions with diameters ranging from a single atom to 20 nm. From a plot of conductance vs junction area, the mean free path ( $l$ ) was calculated to be 3.8 nm. This mean free path value is about ten times shorter than the bulk Au value at 300 K, probably due to the junction diameter, surface roughness, and a large concentration of scattering centers (defects) created during the formation of the atom-scale junction.<sup>32</sup> The mean free path increases with the junction diameter; however, this is not expected to be significant when the junction diameter is less than  $l$ . For atom-scale junctions, the relatively short  $l$  (increased backscattering) and preferred atomic configurations are primarily responsible for shifting the max conductance peaks from the ideal quantized values (integer multiples of  $G_0$ ).

### **1.7.2 Inelastic Scattering (phonons and heating)**

The conductance of atom-scale junctions is also impacted by electron inelastic scattering. Electrons have a small probability of depositing some energy in the lattice

phonon system or local vibration modes of the atom-scale junction, creating heat.<sup>1,60</sup>

When the junction is composed of only a few atoms, the spectrum will measure local vibration modes, rather than bulk phonons. The conductance fluctuations will drown out the local vibration modes for atom-scale junctions. However, the conduction fluctuations are suppressed for a single conductance mode with nearly perfect transmission ( $1 G_0$ ), allowing the local vibration modes ('phonon signal') to be measured.<sup>61</sup> Interestingly, phonon signal spectrum for the atom-scale junction closely resembles the bulk phonon signal spectrum, just with different relative intensities (Figure 1.10).

Since a phonon signal was measured, heating of the junction occurs.<sup>1,61</sup>

Regardless, atom-scale junctions have withstood heating with bias voltages up to nearly 2 V.<sup>21,46-48</sup> At a bias potential of 2 V, the current density in the atom-scale junction is roughly five orders of magnitude larger than for bulk metal wires, which is possible because most of the electrical power ( $P = IV$ ) is converted into kinetic energy for the ballistic electrons. The excess kinetic energy is deposited into the phonon system at an average distance from the junction that is equal to the inelastic mean free path. Therefore, the heat is diluted in the banks, away from the atom-scale junction. The high current carrying capacity of the atom-scale junctions is reflected in the typically linear room temperature  $I$ - $V$  curves, up to at least 0.5 V.<sup>21,44</sup>

## 1.8 Summary

Single-atom monovalent metal junctions have a single conductance mode with nearly perfect transmission, conductance near  $1 G_0$ , sustain a bias potential up to 2 V, and are stable for up to several hours at room temperature (greater stability at 4.2 K).<sup>1</sup> In a single-atom junction (12.9 k $\Omega$ ), a 2 V bias results in a current density of  $2.1 \times 10^{15}$  A/m<sup>2</sup>,

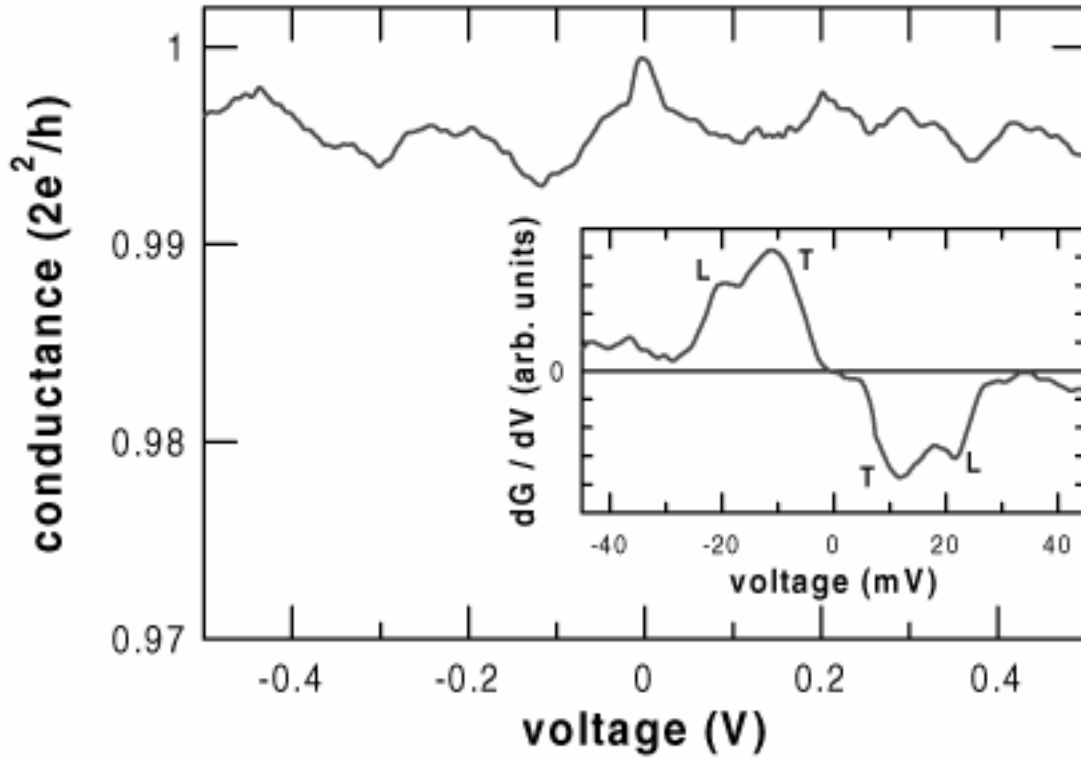


**Figure 1.10:** Plot from measuring conductance as a function of applied bias voltage, for a single-atom Au junction at 4.2 K. The amplitude of the conductance fluctuations is suppressed since the conductance was close to  $1 G_0$ , allowing the observation of the phonon signal. The phonon signal is a maximum at zero bias. The transverse (T) and longitudinal (L) acoustic branches are positioned symmetrically around zero when the derivative of the conductance is plotted as a function of bias potential (inset).<sup>61</sup>

which is more than seven orders of magnitude larger than the current density responsible for incandescence in the tungsten wire of a light bulb. Conductance below  $1 G_0$  has been measured, implying a finite amount of scattering at the interface between the single-atom junction and the banks, as well as scattering off defects in the banks near the junction. A monovalent metal junction with a diameters comparable to the Fermi wavelength demonstrates quantized conductance steps in integer multiples of  $G_0$ , especially up to  $3 G_0$ . The jumps between conductance steps result from a change in junction thickness, due to electrodeposited Au atoms, atomic rearrangements from thermal diffusion, electromigration from applied potential, or mechanical input (STM and MCBJ methods). At the atom-scale, the electrical and mechanical properties of bulk metals break down. Atom-scale junctions are a powerful test bench for nanoscience, which may lead to discovery of new material properties that can be applied in technologies such as circuits and sensors.

## 1.9 Motivation

Although testing theories with atom-scale junctions is interesting, the thrust of this work was to apply the powerful sensing capability of atom-scale junctions in a feasible, field-deployable device. This dissertation details the progress and future directions for building a miniature, robust, regenerable sensor for single molecule detection capability, the ultimate in mass-limited chemical analysis. The sensor is based on a measuring the resistance change resulting from interfacial electron scattering in the junction, due to a chemisorbed analyte. Since a full monolayer of chemisorbed hexadecane thiol (HDT) on a thin, planar Au film ( $t < 50$  nm) produced ~2% change in normalized conductance,<sup>62,63</sup> chemisorbed HDT on an atom-scale junction was expected



to cause a large enough change in resistance for detection of a single molecule. Any detectable changes in electrode resistance should be a result of changes at the junction because of the high resistance in the atom-scale junction compared to the electrode contact pads.

For atom-scale junction formation, the MCBJ and STM methods are too susceptible to vibrational disturbance for implementation into a miniature field-deployable detection device. Furthermore, the STM method is too heavy and costly for a feasible, field-deployable detection device. Therefore, atom-scale junction formation efforts were focused on a unique approach to the self-terminating electrochemical methods introduced by Tao, *et al.*<sup>2,7</sup> Rather than submerging gold wires or Au thin-film electrodes in bulk solution, an elastomeric polydimethylsiloxane (PDMS) microfluidic flow cell was sealed over the junction of two Au thin-film electrodes.<sup>64-67</sup> The applied potential was lower than the values reported by Tao, *et al.*, in order to decrease the rate of reaction for greater junction formation control. By forming atom-scale junction in a microfluidic channel, this technology can be engineered into a miniature chemical agent detection device much more feasibly.

### **1.10 Outline of Work**

An electrochemical cell was designed to form atom-scale junctions with feedback terminated electrochemical deposition. Thin Au film electrodes were fabricated with photolithography and electron beam lithography on both glass and silicon substrates. A PDMS microfluidic channel was used to introduce deposition solution to the junction area for atom-scale junction formation,<sup>64-68</sup> followed by analytes for measurement of interfacial scattering at the atom-scale junction. Many obstacles were overcome in route

to fabricating the electrochemical cell, forming atom-scale junctions, introducing analytes, and measuring the interfacial scattering.

### 1.11 References

- (1) N Agrait, AL Yeyati, JM van Ruitenbeek: "Quantum properties of atomic-sized conductors" *Physics Reports-Review Section of Physics Letters* 377 (2003) 81-279.
- (2) S Boussaad, NJ Tao: "Atom-size gaps and contacts between electrodes fabricated with a self-terminated electrochemical method" *Appl. Phys. Lett.* 80 (2002) 2398-2400.
- (3) C Joachim, JK Gimzewski, A Aviram: "Electronics using hybrid-molecular and mono-molecular devices" *Nature* 408 (2000) 541-548.
- (4) JM Krans, JM Vanruitenbeek, VV Fisun, IK Yanson, LJ Dejongh: "The Signature of Conductance Quantization in Metallic Point Contacts" *Nature* 375 (1995) 767-769.
- (5) B Xu, NJ Tao: "Measurement of Single-Molecule Resistance by Repeated Formation of Molecular Junctions" *Science* 301 (2003) 1221-1223.
- (6) GV Nazin, XH Qiu, W Ho: "Visualization and Spectroscopy of a Metal-Molecule-Metal Bridge" *Science* 302 (2003) 77-81.
- (7) CZ Li, HX He, NJ Tao: "Quantized tunneling current in the metallic nanogaps formed by electrodeposition and etching" *Appl. Phys. Lett.* 77 (2000) 3995-3997.
- (8) HE van den Brom, JM van Ruitenbeek: "Quantum suppression of shot noise in atom-size metallic contacts" *Physical Review Letters* 82 (1999) 1526-1529.

- (9) MA Reed, C Zhou, CJ Muller, TP Burgin, JM Tour: "Conductance of a molecular junction" *Science* 278 (1997) 252-254.
- (10) CZ Li, NJ Tao: "Quantum transport in metallic nanowires fabricated by electrochemical deposition/dissolution" *Appl. Phys. Lett.* 72 (1998) 894-896.
- (11) RHM Smit, Y Noat, C Untiedt, ND Lang, MC van Hemert, JM van Ruitenbeek: "Measurement of the conductance of a hydrogen molecule" *Nature* 419 (2002) 906-909.
- (12) AF Morpurgo, CM Marcus, DB Robinson: "Controlled fabrication of metallic electrodes with atomic separation" *Appl. Phys. Lett.* 74 (1999) 2084-2086.
- (13) M Brandbyge, J Schiøtz, MR Sørensen, P Stoltze, KW Jacobsen, JK Nørskov, L Olesen, E Laegsgaard, I Stensgaard, F Besenbacher: "Quantized Conductance in Atom-Sized Wires between 2 Metals" *Physical Review B* 52 (1995) 8499-8514.
- (14) Z Gai, Y He, HB Yu, WS Yang: "Observation of conductance quantization of ballistic metallic point contacts at room temperature" *Physical Review B* 53 (1996) 1042-1045.
- (15) H Ohnishi, Y Kondo, K Takayanagi: "Quantized conductance through individual rows of suspended gold atoms" *Nature* 395 (1998) 780-783.
- (16) J Hogsved: "Study of Quantized Conductance using a Mechanically Controlled Break Junction in Air at 300 K" *Master Thesis* (1997) Goteborg Department of Experimental Physics.
- (17) J Martinek, W Nawrocki, M Wawrzyniak, J Stankowski: *Molecular Phys. Reports* 20 (1997) 157.

- (18) CZ Li, A Bogozi, W Huang, NJ Tao: "Fabrication of stable metallic nanowires with quantized conductance" *Nanotechnology* 10 (1999) 221-223.
- (19) AI Yanson, GR Bollinger, HE van den Brom, N Agrait, JM van Ruitenbeek: "Formation and manipulation of a metallic wire of single gold atoms" *Nature* 395 (1998) 783-785.
- (20) C Zhou, CJ Muller, MR Deshpande, JW Sleight, MA Reed: "Microfabrication of a Mechanically Controllable Break Junction in Silicon" *Appl. Phys. Lett.* 67 (1995) 1160-1162.
- (21) PJ Castle, PW Bohn: "Interfacial scattering at electrochemically fabricated atom-scale junctions between thin gold film electrodes in a microfluidic channel" *Anal. Chem.* 77 (2005) 243-249.
- (22) WS Augerson: A Review of the Scientific Literature as It Pertains to Gulf War Illnesses, RAND, 2000.
- (23) CJ Muller, JM Vanruitenbeek, LJ Dejongh: "Conductance and Supercurrent Discontinuities in Atomic-Scale Metallic Constrictions of Variable Width" *Physical Review Letters* 69 (1992) 140-143.
- (24) A Bard, L Faulkner: *Electrochemical Methods*, John Wiley & Sons, New York, 1980.
- (25) EC Walter, MP Zach, F Favier, BJ Murray, K Inazu, JC Hemminger, RM Penner: "Metal nanowire arrays by electrodeposition" *Chemphyschem* 4 (2003) 131-138.
- (26) EC Walter, BJ Murray, F Favier, G Kaltenpoth, M Grunze, RM Penner: "Noble and coinage metal nanowires by electrochemical step edge decoration" *Journal of Physical Chemistry B* 106 (2002) 11407-11411.

- (27) A Stalder, U Durig: "Study of plastic flow in ultrasmall Au contacts" *Journal of Vacuum Science & Technology B* 14 (1996) 1259-1263.
- (28) G Rubio-Bollinger, SR Bahn, N Agrait, KW Jacobsen, S Vieira: "Mechanical properties and formation mechanisms of a wire of single gold atoms" *Physical Review Letters* 8702 (2001) art. no.-026101.
- (29) R Landauer: "Spatial variation of currents and fields due to localized scatterers in metallic conduction (reprinted from IBM Journal of Research and Development, vol 1, 1957)" *Ibm Journal of Research and Development* 44 (2000) 251-259.
- (30) JK Gimzewski, R Moller: "Transition from the Tunneling Regime to Point Contact Studied Using Scanning Tunneling Microscopy" *Physical Review B* 36 (1987) 1284-1287.
- (31) PW Bohn, Electronic and Optical Sensing at Atom-Scale Metal Junctions, AFOSR MURI, WPAFB, OH, 2004.
- (32) D Ertz, H Olin, L Ryen, E Olsson, A Tholen: "Maxwell and Sharvin conductance in gold point contacts investigated using TEM-STM" *Physical Review B* 61 (2000) 12725-12727.
- (33) JM Krans, CJ Muller, IK Yanson, TCM Govaert, R Hesper, JM Vanruitenbeek: "One-Atom Point Contacts" *Physical Review B* 48 (1993) 14721-14724.
- (34) M Brandbyge, MR Sorensen, KW Jacobsen: "Conductance eigenchannels in nanocontacts" *Physical Review B* 56 (1997) 14956-14959.
- (35) G Rubio, N Agrait, S Vieira: "Atomic-sized metallic contacts: Mechanical properties and electronic transport" *Physical Review Letters* 76 (1996) 2302-2305.

- (36) SR Bahn, KW Jacobsen: "Chain formation of metal atoms" *Physical Review Letters* 87 (2001).
- (37) H Hakkinen, RN Barnett, U Landman: "Gold nanowires and their chemical modifications" *Journal of Physical Chemistry B* 103 (1999) 8814-8816.
- (38) SR Bahn, N Lopez, JK Norskov, KW Jacobsen: "Adsorption-induced restructuring of gold nanochains" *Physical Review B* 66 (2002).
- (39) Y Takai, T Kawasaki, Y Kimura, T Ikuta, R Shimizu: "Dynamic observation of an atom-sized gold wire by phase electron microscopy" *Physical Review Letters* 8710 (2001) art. no.-106105.
- (40) T Kizuka, S Umehara, S Fujisawa: "Metal-insulator transition in stable one-dimensional arrangements of single gold atoms" *Japanese Journal of Applied Physics Part 2-Letters* 40 (2001) L71-L74.
- (41) MR Sorensen, M Brandbyge, KW Jacobsen: "Mechanical deformation of atomic-scale metallic contacts: Structure and mechanisms" *Physical Review B* 57 (1998) 3283-3294.
- (42) CA Stafford: "Quantum theory of metallic nanocoherence" *Physica E* 1 (1997) 310-312.
- (43) H Mehrez, A Wlasenko, B Larade, J Taylor, P Grutter, H Guo: "I-V characteristics and differential conductance fluctuations of Au nanowires" *Physical Review B* 65 (2002).
- (44) K Hansen, SK Nielsen, M Brandbyge, E Laegsgaard, I Stensgaard, F Besenbacher: "Current-voltage curves of gold quantum point contacts revisited" *Appl. Phys. Lett.* 77 (2000) 708-710.

- (45) CJ Muller, JM Krans, TN Todorov, MA Reed: "Quantization effects in the conductance of metallic contacts at room temperature" *Physical Review B* 53 (1996) 1022-1025.
- (46) H Yasuda, A Sakai: "Conductance of atomic-scale gold contacts under high-bias voltages" *Physical Review B* 56 (1997) 1069-1072.
- (47) K Yuki, A Enomoto, A Sakai: "Bias-dependence of the conductance of Au nanocontacts at 4 K" *Appl. Surf. Sci.* 169 (2001) 489-492.
- (48) SK Nielsen, M Brandbyge, K Hansen, K Stokbro, JM van Ruitenbeek, F Besenbacher: "Current-voltage curves of atomic-sized transition metal contacts: An explanation of why Au is ohmic and Pt is not" *Physical Review Letters* 89 (2002).
- (49) M Brandbyge, JL Mozos, P Ordejon, J Taylor, K Stokbro: "Density-functional method for nonequilibrium electron transport" *Physical Review B* 65 (2002).
- (50) TN Todorov, J Hoekstra, AP Sutton: "Current-induced embrittlement of atomic wires" *Physical Review Letters* 86 (2001) 3606-3609.
- (51) U Landman, WD Luedtke, NA Burnham, RJ Colton: "Atomistic mechanisms and dynamics of adhesion, nanoindentation, and fracture." *Science* 248 (1990) 454-461.
- (52) M Brandbyge, KW Jacobsen, JK Norskov: "Scattering and conductance quantization in three-dimensional metal nanocontacts" *Physical Review B* 55 (1997) 2637-2650.

- (53) AM Bratkovsky, AP Sutton, TN Todorov: "Conditions for Conductance Quantization in Realistic Models of Atomic-Scale Metallic Contacts" *Physical Review B* 52 (1995) 5036-5051.
- (54) JA Torres, JJ Saenz: "Conductance and mechanical properties of atomic-size metallic contacts: A simple model" *Physical Review Letters* 77 (1996) 2245-2248.
- (55) JC Cuevas, AL Yeyati, A Martin-Rodero, GR Bollinger, C Untiedt, N Agrait: "Evolution of conducting channels in metallic atomic contacts under elastic deformation" *Physical Review Letters* 81 (1998) 2990-2993.
- (56) M Brandbyge, N Kobayashi, M Tsukada: "Conduction channels at finite bias in single-atom gold contacts" *Physical Review B* 60 (1999) 17064-17070.
- (57) AM Bratkovsky, SN Rashkeev: "Electronic transport in nanoscale contacts with rough boundaries" *Physical Review B* 53 (1996) 13074-13085.
- (58) B Ludoph, MH Devoret, D Esteve, C Urbina, JM van Ruitenbeek: "Evidence for saturation of channel transmission from conductance fluctuations in atomic-size point contacts" *Physical Review Letters* 82 (1999) 1530-1533.
- (59) H Hakkinen, RN Barnett, AG Scherbakov, U Landman: "Nanowire gold chains: Formation mechanisms and conductance" *Journal of Physical Chemistry B* 104 (2000) 9063-9066.
- (60) IK Yanson, OI Shklyarevsky: "Point-Contact Spectroscopy of Metallic Alloys and Compounds" *Fizika Nizkikh Temperatur* 12 (1986) 899-933.
- (61) C Untiedt, GR Bollinger, S Vieira, N Agrait: "Quantum interference in atomic-sized point contacts" *Physical Review B* 62 (2000) 9962-9965.



- (62) Y Zhang, RH Terrill, PW Bohn: "In-plane resistivity of ultrathin gold films: A high sensitivity, molecularly differentiated probe of mercaptan chemisorption at the liquid-metal interface" *J. Am. Chem. Soc.* 120 (1998) 9969-9970.
- (63) YM Zhang, RH Terrill, PW Bohn: "Chemisorption and chemical reaction effects on the resistivity of ultrathin gold films at the liquid-solid interface" *Anal. Chem.* 71 (1999) 119-125.
- (64) BH Jo, LM Van Lerberghe, KM Motsegood, DJ Beebe: "Three-dimensional micro-channel fabrication in polydimethylsiloxane (PDMS) elastomer" *Journal of Microelectromechanical Systems* 9 (2000) 76-81.
- (65) TC Kuo, DM Cannon, YN Chen, JJ Tulock, MA Shannon, JV Sweedler, PW Bohn: "Gateable nanofluidic interconnects for multilayered microfluidic separation systems" *Anal. Chem.* 75 (2003) 1861-1867.
- (66) TC Kuo, DM Cannon, MA Shannon, PW Bohn, JV Sweedler: "Hybrid three-dimensional nanofluidic/microfluidic devices using molecular gates" *Sensors and Actuators a-Physical* 102 (2003) 223-233.
- (67) DC Duffy, JC McDonald, OJA Schueller, GM Whitesides: "Rapid prototyping of microfluidic systems in poly(dimethylsiloxane)" *Anal. Chem.* 70 (1998) 4974-4984.
- (68) DM Cannon, TC Kuo, PW Bohn, JV Sweedler: "Nanocapillary Array Interconnects for Gated Analyte Injections and Electrophoretic Separations in Multilayer Microfluidic Architectures" *Anal. Chem.* 75 (2003) 2224-2230.

## CHAPTER 2

### FABRICATION OF MICROFLUIDIC ELECTROCHEMICAL FLOW CELL

#### 2.1 Introduction

In order to avoid the shortcomings of the MCBJ and STM atom-scale junction formation methods, electrochemical methods were pursued for integration into a miniature field-deployable detection device. Atom-scale junctions formed with the MCBJ and STM methods (no substrate under junction) are likely more vulnerable to vibrational disturbances than an atom-scale junction formed electrochemically on a substrate. Furthermore, an STM is too large and costly to implement into a field-deployable detection device. A miniature device is suited for field-detection because it could be easily transported, would require less sample volume, and could assay several samples simultaneously for confirmation.<sup>1</sup> The high throughput potential of a miniature device translates into early detection of chemical/ biological agents, which saves lives. Therefore, a miniature electrochemical flow cell was fabricated for use in a field-deployable detection device that is based on the powerful sensing potential of the atom-scale junction.

#### 2.2 Experimental Methods

Construction of the miniature flow cell started by aligning a PDMS microfluidic channel over a gap between two thin film Au electrodes on a substrate of glass or silicon (<100>, test grade, boron doped). The thin film electrodes were easily designed with lithographic techniques and allowed sealing of a PDMS microfluidic channel (Figure 2.1). The microfluidic channel allowed for less electrolyte consumption and isolated the

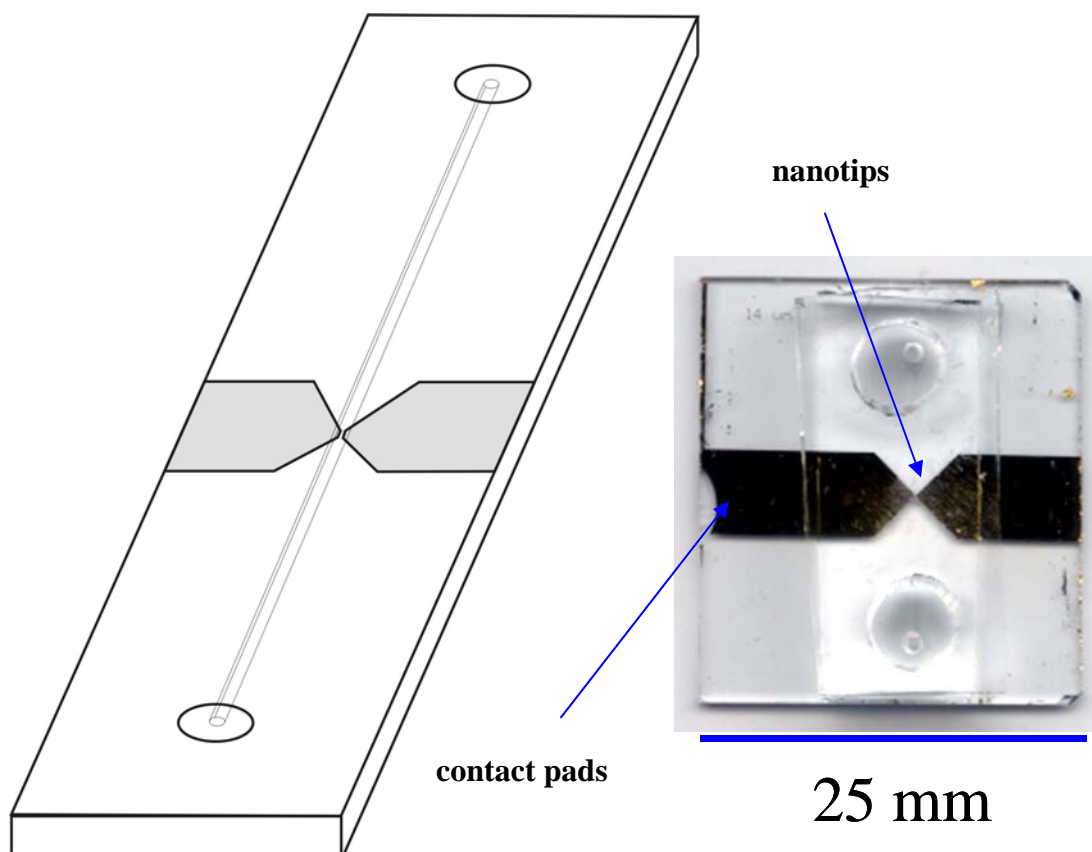


**Figure 2.1:** Schematic diagram and photograph of a microfluidic electrochemical flow cell. The thin film Au electrodes were fabricated with a combination of photolithography (contact pads) and electron beam lithography (nanotips). The contact pads have a ~10 nm Cr or Ti adhesion layer topped with 150 nm of sputtered or evaporated Au. The electrode nanotips have ~ 5 nm of Ti topped with ~ 40 nm of Au. The 100  $\mu\text{m}$  wide PDMS channel (bottom layer) spans the inter-electrode starting gap of about 40 nm (not visible in image). A PDMS reservoir layer is on top of the channel layer. The reservoir layer was later replaced with connectors for a peristaltic pump.

electrochemistry to a micrometer-scale area on the thin film electrodes, which allowed the inter-electrode gap to be closed with less time for a particular current density. Au wire leads (0.25 mm) were connected to the thin film electrodes with Teflon press connections.

### **2.2.1 PDMS Microfluidics**

The PDMS channel and reservoir layers were fabricated using standard rapid prototyping protocols.<sup>1-5</sup> The PDMS channel (100  $\mu\text{m}$  or 1 mm width) was designed with CAD software and printed with a commercial laser printer onto transparency film (5080 dpi, 5  $\mu\text{m}$  pixel, Printing Services, University of Illinois at Urbana-Champaign). To make positive relief master molds, the transparency film was used as a UV mask over a Si wafer (Silicon Quest International, Santa Clara, CA) coated with negative-tone UV photoresist specific for 50  $\mu\text{m}$  deep channels, SU 8-50 (Microlithography Chemical Corp, Newton, MA). A 10:1 weight ratio of prepolymer:curing agent (Sylgard 184, Dow Corning Corp, Midland, MI) was thoroughly mixed for 5 min and vacuum-aspirated for 1 h to remove air bubbles. The prepolymer mixture was poured to  $\sim 1$  mm thickness over the Si wafer master in a petri dish for the channel layer and to  $\sim 2$  mm thickness in a petri dish for the reservoir layer. After heating for 1 h at 110  $^{\circ}\text{C}$ , holes were punched in the channel (1 mm diameter) and reservoir (5 mm diameter) layers.

For efficiency of solution exchange, the PDMS reservoir layer was later abandoned to integrate a Cole-Parmer peristaltic pump (minimum flow = 0.6 mL/ min). Polyaryletherketone (PEEK) connectors (1 mm inside diameter) were fabricated in the SCS machine shop and used to connect the 0.8 mm L/S 13 tubing to the PDMS microfluidic channel. For proper fit, the connector joint diameter had to be slightly

smaller than the channel via diameter, and the connector joint length had to be slightly shorter than the channel layer thickness. The connectors were sealed to the PDMS with epoxy to prevent leaking. The PDMS was roughened to promote bonding with the epoxy. In order to prevent epoxy from clogging the channel, a very thin layer of epoxy was added to the connector and allowed to become tacky before pressing over the channel via. After allowing the epoxy to dry overnight, the 0.8 mm L/S 13 peristaltic pump tubing was attached to the connector. A few inches of Teflon tubing (1 mm inside diameter) was added to the L/S 13 tubing with heat-shrink tubing in order to observe the solution flow before entering the channel. An intentionally placed air bubble is a simple means to indicate when a new solution is about to enter the channel (or count exit tube drops).

### **2.2.2 Thin Au Film Electrode Fabrication**

The thin Au film electrodes were fabricated on 25 mm square glass and silicon substrates. Initially, glass coverslips were used. Due to breakage, the glass substrate was cut from a standard Fisher Scientific glass microscope slide. The silicon substrate was cut from a Si <100> wafer with a four-inch diameter. Prior to Au deposition, the substrate was cleaned by solvent rinsing (acetone, isopropyl, DI), soaking in 150 °C buffered HF (10:1 dilution), soaking in 10:1 H<sub>2</sub>O<sub>2</sub>:NH<sub>4</sub>OH and ultrasonic rinsing. However, this time consuming cleaning procedure (> 1 hr) was not necessary for adequate metal adhesion to the substrate, so this procedure was replaced with piranha cleaning (3 parts H<sub>2</sub>SO<sub>4</sub>: 1 part H<sub>2</sub>O<sub>2</sub>) for five minutes. CAD software was used to design a photolithography mask for fabricating the Au thin film electrodes.<sup>4</sup> The electrodes have large contact pads (8 mm x 5 mm) for connecting the Au wire leads with

Teflon press connectors. The Au thin film electrodes were fabricated with one of three methods: (1) photolithography with metal etching, (2) photolithography with metal lift-off, and (3) photolithography and electron beam lithography with metal lift-off.

#### **2.2.2.1 Photolithography with Metal Etching**

For electrodes formed by photolithography with metal etching, a Lesker CMS 18 sputter coater (Figure 2.2) was used to sputter an ~10 nm adhesion layer of Cr on the glass substrate (300 W, 30 s), immediately followed by ~150 nm of Au (300 W, 30 s). With sputter coating, Ar gas hits a target metal with enough energy to dislodge Au and coat the sample (medium vacuum). Next, a spin coater was operated at 5000 rpm for 30 seconds to cover the sample with a positive-tone UV photoresist (AZ 5214, Clariant Corp, Somerville, NJ), followed by a 30 s solvent bake at 110 °C. The spinner leaves an edge bead on the sample (photoresist thicker on edges). The edge bead was removed by masking the desired sample area, exposing the edge bead to UV for 12 s (40 mW/ cm<sup>2</sup>), and then dissolving the edge bead with a developer (AZ 327 MIF, Clariant Corp). The UV breaks enough bonds in the photoresist to allow it to dissolve in the developer. To resolve the desired electrode area, the CAD designed Cr mask (on glass) was aligned on the sample, followed by UV exposure for 2 s. Note that the UV exposure time was less for the thinner layer of photoresist. The UV exposed photoresist was removed with the developer. The photoresist-free metal layer was removed by soaking a few seconds in Au etchant (TFA, Transene Co, Danvers, MA) and then up to 1 min in Cr etchant (CEP-200, Microchrome Technology, Reno, NV). The sample was inspected under a microscope to ensure the metal outside the desired electrode area was removed, especially in the junction area (could short out electrode). Finally, the photoresist



**Figure 2.2:** Image of the Lesker CMS 18 sputter coater, which was used to sputter a 5 nm adhesion layer of Cr on the glass substrate, immediately followed by 150 nm of Au. The sample was brought through the load lock (LL) and the Radial Distribution Chamber (RDC) to get to the sputter chamber (SC) for Au deposition.

protecting the designed electrode from the etchants was removed with a stripper (Shipley 1165 Microposit Remover, Rohm and Haas).

#### **2.2.2.2 Photolithography with Metal Lift-off**

For electrodes formed by photolithography with metal lift-off, a positive-tone UV photoresist (AZ 5214) was applied (5000 rpm, 30 s), followed by a 30 s solvent bake at 110 °C. The edge bead was then removed as described above. To reveal the designed electrode area, a Cr mask was placed on the substrate and then exposed to UV light for 2 s (40 mW/ cm<sup>2</sup>). This was followed by baking at 120 °C for 90 s for cross-linking in the area exposed to the UV. Without a mask, the sample was then exposed to the UV for 8 s. The cross-linked photoresist outside the designed electrode area holds up to this exposure. However, the photoresist bonds are broken down in the previously masked electrode area, allowing the electrode area photoresist to be dissolved with developer (AZ 327 MIF). After sputter coating the Cr adhesion layer and Au contact pads, the metal outside the desired electrode area was lifted-off by dissolving the photoresist under the metal with a commercial photoresist stripper (Shipley 1165) or acetone (15 to 45 minutes). The lift-off was accelerated by placing the sample in a sonicator and by heating the acetone or stripper.

#### **2.2.2.3 Photolithography and Electron Beam Lithography**

The last thin-film Au electrode fabrication method is a combination of electron beam lithography and photolithography on thermally oxidized silicon, done in collaboration with Professor Adesida's group (Bill Lanford and Dr. Niu).<sup>6</sup> The photolithography and electron beam lithography procedures utilized a metal lift-off



technique. First, the JEOL JBX-6000FS electron beam (JEOL Ltd, Tokyo, Japan) was used to make electrode tips (~10 nm Ti adhesion layer, ~40 nm Au). The lithography was done with a two-layer resist technique employing: (1) 496 kDa PMMA in chlorobenzene, and (2) 950 kDa PMMA in chlorobenzene (Allresist GmbH, Strausberg, Germany). Photolithography with thermal evaporation (high vacuum) of Au was used to define the contact pads (~10 nm Ti, ~90 nm Au). A negative-tone UV photoresist (AZ 5214E, Clariant Corp) was applied before metal deposition, and the Cr mask was used to expose only the designed electrode area. After developing the photoresist and depositing the metal, the metal outside the designed electrode area was lifted off by dissolving the photoresist underneath the metal. For increased throughput and to save electron beam usage costs, eighteen nanotips were written on one Si <100> chip, which was cut into nine 25 mm square samples with two sets of nanotips per sample.

Electron-beam lithography was also used to form nanobridges that were connected with photolithographically fabricated contact pads. The nanobridge was about 90 nm wide and 150 nm long. The nanobridge was broken with a current sweep that induced electromigration of the Au atoms, resulting in reproducible inter-electrode gaps of < 5 nm, based on measuring tunneling current.<sup>7</sup>

## **2.3 Results and Discussion**

### **2.3.1 Thin Au Film Electrode Fabrication (Photolithography)**

The PDMS microfluidic channel was able to seal over the 150 nm thick thin-film Au electrodes. The thin-film electrode thickness was determined by a previous calibration of the sputtering chamber and confirmed by AFM data. The electrodes have large contact pads (8 mm x 5 mm) for Au wire press connections and to isolate any

change in resistance at the junction. With the pad length ( $l$ ) on the mm scale and the junction on the nm scale, changes in resistance are attributed to changes at the junction. The pads taper down to the junction to expose more substrate for sealing the PDMS channel near the junction. The electrodes were drawn using CAD software and printed on transparency film with a commercial laser printer (5080 dpi).<sup>4</sup> The transparency film mask was used to make a chrome mask (on glass), because the Cr mask rests tighter on the electrode substrate than the transparency film, limiting UV exposure to designed areas.

The inter-electrode gap size impacts the visual alignment of the microfluidic channel, the Au deposition time required to close the gap, and the stability of the junction. Therefore, both lithography and electrode design were optimized to reduce the gap size. First, the edge bead was removed to help ensure the UV exposure was limited to areas defined by the Cr mask. The edge bead is formed from spin coating the photoresist on the substrate. The edge bead does not allow the Cr mask to sit tightly against the substrate, allowing stray UV under the mask. Unless the edge bead is removed, this stray light will widen the inter-electrode gap. Second, the etch time was optimized to prevent widening the inter-electrode gap by over-etching the metal. To identify the proper etch time, the Cr/Au etching was done incrementally to ensure enough metal was removed in the inter-electrode gap to prevent shorting the electrodes (not enough etch time), while avoiding under-etching the photoresist protecting the Au electrode pattern (etch time too long). These processing precautions enable resolution within a few micrometers of the Cr mask gap size.

To reduce the photolithographically fabricated inter-electrode gap further and to optimize the Au deposition pattern for isolating one atom-scale junction, Cr masks were made with different tip shapes. The inter-electrode gap was limited by the resolution of the 5080 dpi printer transparencies and by the degree of photoresist under-etching. The electrode tip shape impacted the degree of photoresist under-etching. Squared off electrodes formed a deposition pattern that hindered the isolation of one junction. Electrode tip angles below  $90^\circ$  led to deleterious under-etching, while contact pad tip angles in excess of  $90^\circ$  were avoided to ensure enough glass was exposed for sealing the PDMS around the Au thin film electrode. A  $90^\circ$  tip angle was identified as the optimal design for optimum resolution ( $28\text{ }\mu\text{m}$ ) to reduce the fabricated inter-electrode gap size and for optimum deposition pattern for isolating the electrochemically formed junction (Figure 2.3). This electrode tip analysis was valuable when designing the electrodes for a commercially produced laser drawn mask ( $3\text{ }\mu\text{m}$  gap).

Once experiments unveiled a strong correlation between the starting gap size and junction stability, a commercially produced laser-drawn Cr mask ( $3\text{ }\mu\text{m}$  gap) was purchased. The mask was fabricated by rastering a laser across the mask to expose the resist layer. After the resist layer was patterned on the Cr mask plate, then the Cr is etched away from the exposed areas. With the laser-drawn mask, photolithography with etching only enabled 5 to  $10\text{ }\mu\text{m}$  gaps due to under-etching of the photoresist, but metal lift-off enabled a gap comparable to the mask gap size ( $3\text{ }\mu\text{m}$ ). Therefore, the metal-lift off procedure was utilized for lowering the attainable photolithographically fabricated inter-electrode gap size to  $3\text{ }\mu\text{m}$ . Since the junction stability was the limiting factor for

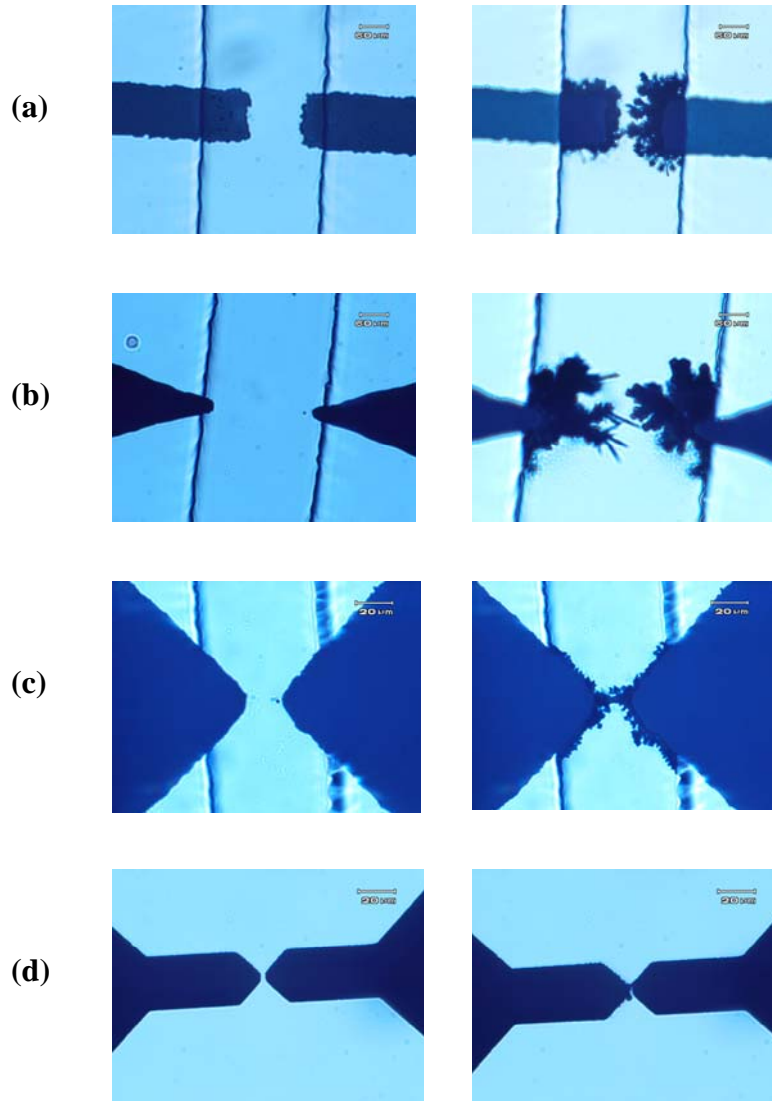


**Figure 2.3:** Optical micrographs of electrode junction area, all 40X except the deposition image (b), which is 60X. The scale bars should all be labeled 20  $\mu\text{m}$ , except the deposition image (b), which is 30  $\mu\text{m}$ . A 90° tip angle was identified as the optimal design, (c), for optimum resolution (28  $\mu\text{m}$ ) and deposition pattern. Electrode tip angles below 90° like (b) led to deleterious under-etching. Squared off electrodes like (a) formed a deposition pattern that hindered the isolation of one junction. This electrode tip analysis was valuable when designing electrodes for a commercially produced laser drawn mask with a 3  $\mu\text{m}$  inter-electrode gap, (d).

utilizing atom-scale junctions as sensors, electron beam lithography was pursued to push the inter-electrode gap size even smaller.

### **2.3.2 Electron Beam Lithography (Nanotips)**

Electron beam lithography was used to form “nanotips” (~ 40 nm gap) for the photolithographically fabricated thin film Au electrodes.<sup>6</sup> Initially, the 5080 dpi Cr mask (~28  $\mu\text{m}$  gap) was aligned over the nanotips for fabricating lead contact pads, and later the 3  $\mu\text{m}$  gap laser-drawn mask was used (Figure 2.4). While adding the contact pads photolithographically, a few issues were encountered. First of all, the pads did not have an adequate resist undercut for multidirectional sputter coating of Au (vs. more uniform thermal evaporation). Sputter coating apparently coated the sidewalls of the resist, which connected the metal on the substrate to the metal on the photoresist. The dark edges around the thin film electrodes are likely ragged metal (not photoresist) from tearing the metal film during lift off (Figure 2.5). This is supported by the fact that the dark edges survived AZ1165 photoresist stripper and a boiling acetone bath. With thermal evaporation of Au, the same resist profile is sufficient to prevent the metal on the substrate from connecting to the metal on the photoresist. To prevent future lift-off problems with sputter coated Au, a bilayer resist procedure was implemented with a photoresist overhang of ~1  $\mu\text{m}$ .

After adding the contact pads, the nanotips would break due to charging effects on the glass substrate, resulting in a 250 nm to 2  $\mu\text{m}$  inter-electrode gap (Figure 2.6). Many attempts were made to form stable nanotips on glass, because this transparent substrate could be monitored from underneath with an inverted microscope, using transmitted brightfield illumination. Upon switching to a thermal oxide treated silicon substrate, the

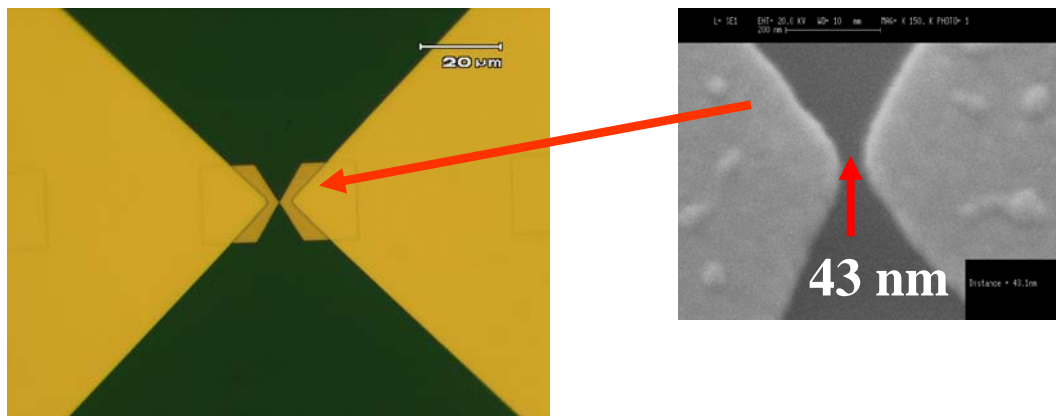


**Figure 2.4:** Optical micrograph (40X) of electrodes with nanotips (left), and high resolution SEM image of nanotips (right). Electron beam lithography was used to form the nanotips with a spacing of  $\sim 40$  nm. Initially, the 5080 dpi Cr mask ( $\sim 28$   $\mu\text{m}$  gap) was aligned over the nanotips for fabricating contact pads for the leads, and later the 3  $\mu\text{m}$  gap laser-drawn mask was used.

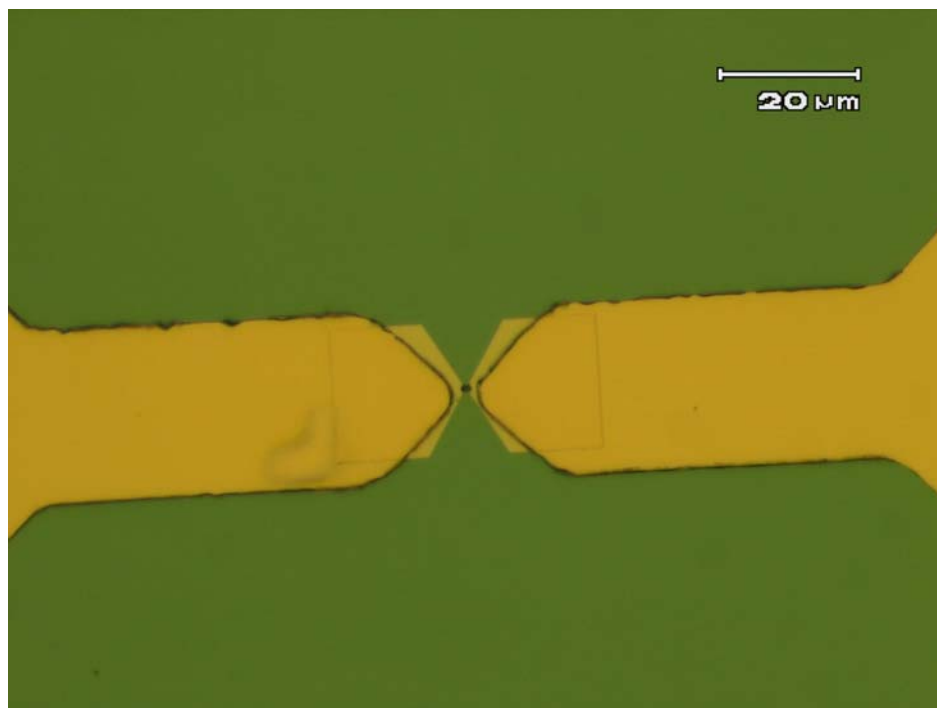


**Figure 2.5:** Optical micrograph (40X) of thin film electrodes with nanotips. The dark material on the thin film electrode edges and between the nanotips is likely ragged metal (not photoresist) from tearing the metal film during lift off. This is supported by the fact that the dark edges survived AZ1165 PR stripper and a boiling acetone bath.

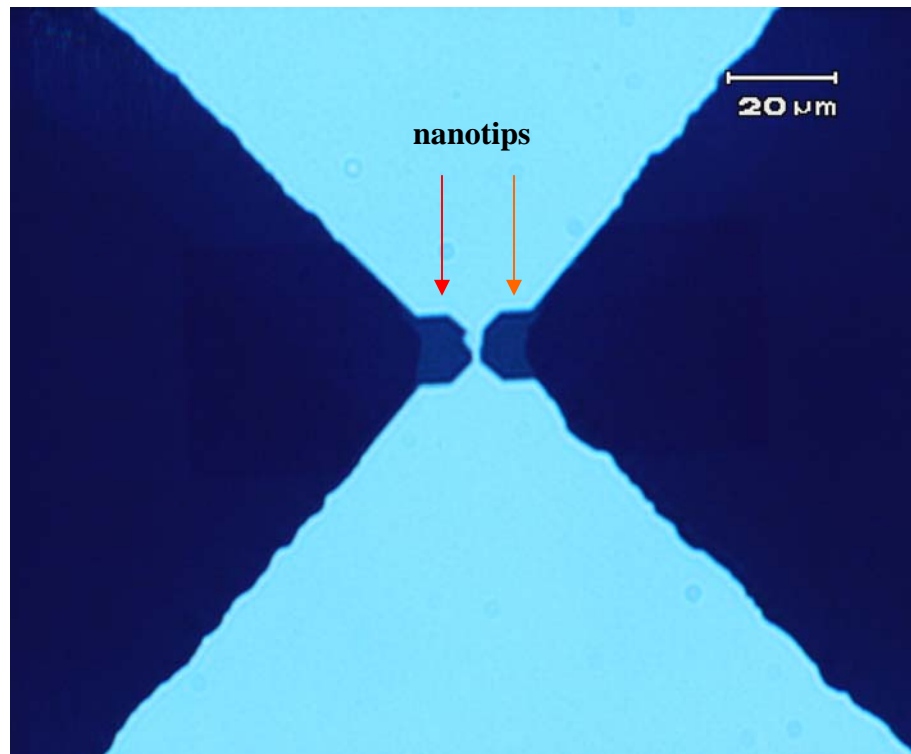


**Figure 2.6:** Optical micrograph (40X) illustrating broken nanotips. Electron beam lithography was used to form nanotips with a spacing of  $\sim 40$  nm. During the process of adding the contact pads, the nanotips would break, resulting in a 250 nm to 2  $\mu$ m inter-electrode gap.



nanotip breakage was eliminated. The non-transparent silicon substrate was monitored with a 10X objective, utilizing reflected brightfield illumination. To use the 50X objective with reflected brightfield illumination, the PDMS microfluidic channel was removed because the objective working distance was not sufficient. For transmitted brightfield with the inverted microscope, the PDMS channel did not interfere because the light entered from underneath the device.

The native silicon oxide layer (1-2 nm) was not adequate for insulating the sample from the conductive silicon. Current was measured across the substrate with a DVM by simply pressing the metal tip leads to the surface. Current was also measured between the nanotips with an inter-electrode spacing of 30 nm, which is too large for tunneling. Therefore, the silicon was thermally oxidized (> 20 nm oxide layer) to ensure the Si substrate conductivity did not interfere with atom-scale junction conductivity measurements.

### **2.3.3 Microfluidic Channel**

Significant effort was invested to identify the optimum strategy for aligning and sealing the PDMS microfluidic channel over the lithographically defined Au inter-electrode gap. The Kasper 2000 contact aligner was configured to vacuum hold the substrate and adjusted for aligning the 100  $\mu\text{m}$  PDMS channel layer over the inter-electrode gap (Figure 2.7). The PDMS channel alignment process could take up to one hour. The alignment was complicated when plasma sealing the PDMS channel to the substrate, because the PDMS channel had to be placed on the substrate within a couple minutes of plasma treating.



**Figure 2.7:** Image of the Kasper 2000 contact aligner, which was configured for aligning the 100  $\mu\text{m}$  PDMS channel layer over the initial  $\sim 28 \mu\text{m}$  inter-electrode gap.

Oxygen plasma treatment of the PDMS channel layer was initially used to ensure an adequate channel seal.<sup>2,4,5</sup> The treatment was active long enough for channel alignment (~1 min), with realignment possible, since the plasma treated surfaces were active for a few minutes. However, after the O<sub>2</sub> plasma treated surfaces sealed, the channel could not be removed intact to analyze the junction with a scanning electron microscope (SEM). This motivated attempts to seal the channel without plasma treatment. By maintaining a clean PDMS channel layer and clean substrate, Van der Waals forces provided a sufficiently strong seal between the channel and the substrate. The channel seal was verified with fluorescence by observing 1  $\mu$ M fluorescein in the channel.<sup>5</sup> Therefore, in all subsequent experiments, the PDMS channel was not plasma treated. When the channel was removed, it was placed channel side up in a clean Petri dish. Before realigning the channel, the substrate and PDMS channel were cleaned with alcohol (ethanol or isopropyl). With this careful handling procedure, the PDMS channel could be removed and sealed over 25 times. Even when stored under nitrogen for several months, the channels still sealed well, contradicting the common notion that PDMS must be used immediately for a proper seal.

Channel alignment was eventually simplified (to save time) by visually aligning the channels rather than using the contact aligner. Using a bright light, only a few minutes was required to visually align the 100  $\mu$ m channel over inter-electrode starting gaps < 28  $\mu$ m, aided by the tapered design of the electrode tips. To minimize pressure effects, the channel width was eventually switched to 1 mm. At this width, the channel could be aligned (by eye) over the nano or microscale inter-electrode gap within seconds.

## 2.4 References

- (1) TC Kuo, DM Cannon, MA Shannon, PW Bohn, JV Sweedler: "Hybrid three-dimensional nanofluidic/microfluidic devices using molecular gates" *Sensors and Actuators a-Physical* 102 (2003) 223-233.
- (2) BH Jo, LM Van Lerberghe, KM Motsegood, DJ Beebe: "Three-dimensional micro-channel fabrication in polydimethylsiloxane (PDMS) elastomer" *Journal of Microelectromechanical Systems* 9 (2000) 76-81.
- (3) DM Cannon, TC Kuo, PW Bohn, JV Sweedler: "Nanocapillary Array Interconnects for Gated Analyte Injections and Electrophoretic Separations in Multilayer Microfluidic Architectures" *Anal. Chem.* 75 (2003) 2224-2230.
- (4) DC Duffy, JC McDonald, OJA Schueller, GM Whitesides: "Rapid prototyping of microfluidic systems in poly(dimethylsiloxane)" *Anal. Chem.* 70 (1998) 4974-4984.
- (5) TC Kuo, DM Cannon, YN Chen, JJ Tulock, MA Shannon, JV Sweedler, PW Bohn: "Gateable nanofluidic interconnects for multilayered microfluidic separation systems" *Anal. Chem.* 75 (2003) 1861-1867.
- (6) P Rai-Choudhury (Ed.)^(Eds.), Handbook of Microlithography, Micromachining, and Microfabrication. SPIE Press, 1997.
- (7) H Park, AKL Lim, AP Alivisatos, J Park, PL McEuen: "Fabrication of metallic electrodes with nanometer separation by electromigration" *Appl. Phys. Lett.* 75 (1999) 301-303.

## CHAPTER 3

### ATOM-SCALE JUNCTION FORMATION

#### 3.1 Experimental Methods

##### 3.1.1 Reagents

The 0.2 M HCl was prepared with deionized (DI) water (18.2 M $\Omega$  cm, Milli-Q UV-plus system, Millipore, Bedford, MA) filtered through a vacuum-aspirated 0.1  $\mu$ m membrane filter system (Fisher Scientific, Pittsburgh, PA). HDT and HAuCl<sub>4</sub> were purchased from Aldrich. The Au deposition solution was prepared with 2.0 mM HAuCl<sub>4</sub> and 0.05 M HClO<sub>4</sub>.<sup>1,2</sup> The 10 mM HDT solution was prepared in absolute ethanol (EtOH) obtained from Aaper Alcohol and Chemical Co.

##### 3.1.2 Electrodeposition with [Au<sup>+3</sup>]

The Au deposition solution (2.0 mM HAuCl<sub>4</sub> and 0.05 M HClO<sub>4</sub>) was introduced to the inter-electrode gap by one of three ways: 1.) pipet-filling a single open reservoir (5  $\mu$ l), 2.) vacuum-filling a PDMS microfluidic channel between two open reservoirs, or 3.) utilizing a Cole-Parmer peristaltic pump to fill a PDMS microfluidic channel (closed system). Vacuum-filling was accomplished by loading one reservoir with solution and holding a tube under house vacuum against the other reservoir. The peristaltic pump was equipped with a Masterflex L/S variable speed modular drive (1-100 rpm, 115 V) with the smallest tubing (L/S 13, 0.8 mm inside diameter), which allows 0.6 ml/min to 6 ml/min flow rates. The pump tubing was attached to the microfluidic channel with specially designed connectors, forming a closed system.

The device was mounted on an Olympus IX70 inverted microscope, and the electrodeposition was monitored under the 40X objective. For the open reservoir device, a Pine Instruments bipotentiostat (model AFCBP1) was employed to deposit Au on both electrodes simultaneously, utilizing a micro Ag/AgCl reference electrode (Cypress Systems, Inc.) in one PDMS reservoir and a Pt wire counter electrode in the other reservoir.<sup>3</sup> With an applied potential of 0.3 V, the inter-electrode gap was reduced from ~28  $\mu\text{m}$  to less than 5  $\mu\text{m}$  in about 20 minutes. The peristaltic pump system was not designed for a reference electrode, so a bias of 1 V was used to reduce the gap from ~28  $\mu\text{m}$  to less than 5  $\mu\text{m}$  in less than 5 minutes.

### **3.1.3 Directional Electrodeposition (etch/ deposit)**

Once the inter-electrode gap was < 5  $\mu\text{m}$  under the 40X objective, the electrodeposition was terminated before contact by turning off the applied potential. For forming the atom-scale junction with auto-terminated directional electrodeposition, the leads were switched from the referenced Pine bipotentiostat to the two-electrode potentiostat with built-in external resistor and comparator. Electrodepositing Au on the electrodes before directional electrodeposition was not necessary, if the Au thin-film electrodes were ~150 nm thick with an inter-electrode gap of < 5  $\mu\text{m}$ . A data acquisition (DAQ) card and Labview software were used to capture the junction formation data (current *vs.* time plots).

#### **3.1.3.1 Resistor-Terminated Directional Electrodeposition**

Tao *et al.* described a self-terminating technique to form atom-scale junctions, utilizing an in-series external resistor ( $R_{ext}$ ) to terminate directional electrodeposition at a preset gap or junction size (Figure 3.1).<sup>4</sup> First, the microfluidic channel was filled with

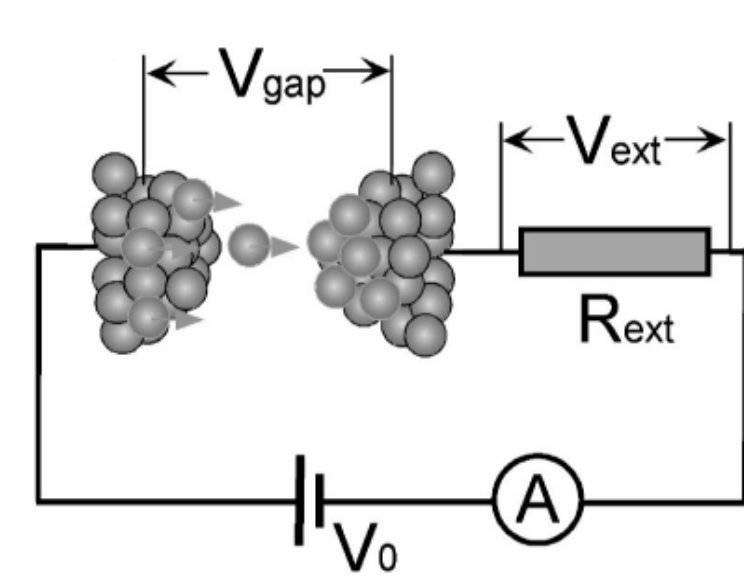


**Figure 3.1:** Schematic of the resistor-terminated method (developed by Tao *et al.*) of forming atom-scale junctions, utilizing an in-series external resistor ( $R_{\text{ext}}$ ) to terminate directional electrodeposition at a preset junction or gap size,  $V_{\text{gap}} = V_0 [R_{\text{gap}} / (R_{\text{gap}} + R_{\text{ext}})]$ .<sup>4</sup>

0.2 M HCl. For directional electrodeposition, a potential was applied between the electrodes. Metal atoms are oxidized (etched) from the anode and reduced (deposited) at the cathode. The electrolysis was terminated when the resistance in the junction ( $R_{gap}$ ) was reduced sufficiently (with respect to  $R_{ext}$ ) to lower the potential in the gap ( $V_{gap}$ ) below the effective potential for directional electrodeposition. This is expressed by  $V_{gap} = V_{appl} * [R_{gap} / (R_{gap} + R_{ext})]$ .<sup>4</sup>  $V_{appl}$  is the potential applied across the gap filled with electrolyte. The conductance quantum ( $G_0$ ) is  $2e^2/h$ , which is equal to  $1/12.9 \text{ k}\Omega$ . Theoretically, a junction should be formed if  $1/R_{ext}$  is comparable to or greater than  $G_0$ , and a gap should be formed if  $1/R_{ext}$  is much smaller than  $G_0$ .<sup>5-10</sup> This is supported by the Butler-Volmer equation, which demonstrates that current density decreases exponentially as  $V_{gap}$  decreases.<sup>3,11</sup>

### 3.1.3.2 Comparator-Terminated Directional Electrodeposition

Comparator-terminated directional electrodeposition is an auto-terminating technique that utilizes a feedback loop to form atom-scale junctions (Figure 3.2). The comparator was preset to terminate the electrolysis by triggering a mechanical relay at a current corresponding to that of an atom-scale junction,  $< 5 G_0$ .<sup>6</sup> The total time from the signal input exceeding the referenced set-point to relay closure was set for  $\sim 600 \mu\text{s}$  (capable of  $100 \mu\text{s}$ ), which was slow enough to prevent the noise from falsely triggering the relay. The junction was formed with directional electrodeposition by applying a bias potential of  $\sim 0.9 \text{ V}$  between the anode and cathode in the microfluidic channel (0.2 M HCl electrolyte). When tunneling current was measured,  $V_{appl}$  was lowered to  $0.3 \text{ V}$  to slow the electrolysis for better control before the comparator terminated the electrolysis at a preset current corresponding to an atom-scale junction. For additional control, an



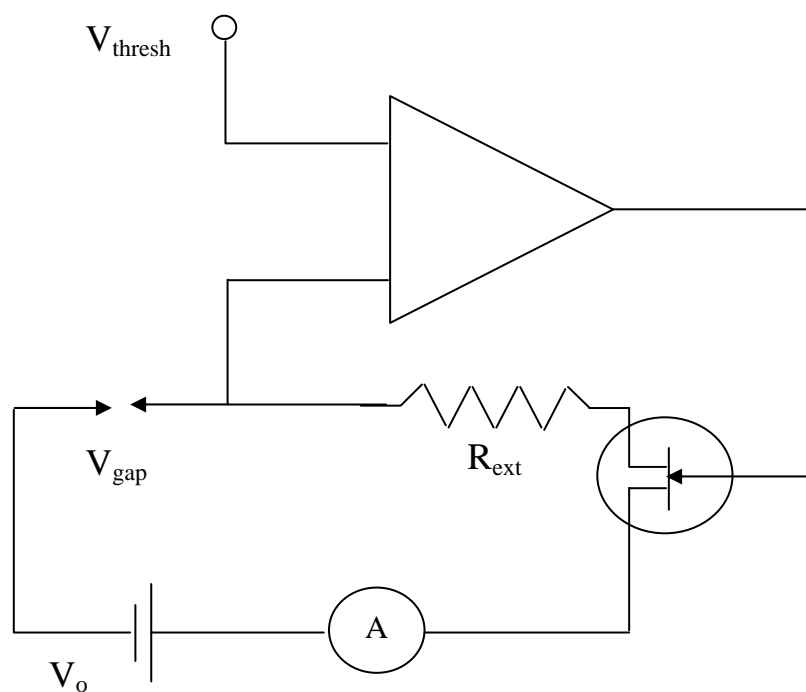


**Figure 3.2:** Schematic for the comparator-terminated atom-scale junction formation. A comparator was preset to trigger a mechanical relay that terminated the electrolysis at a current corresponding to an atom-scale junction ( $\sim 1 G_0$ ).

external resistance ( $R_{ext}$ ) equal to 100 k $\Omega$  was added to slow the deposition near the contact:  $V_{gap} = V_{appl} [R_{gap}/(R_{gap} + R_{ext})]$ .

### **3.1.4 Junction Regeneration**

A Pine bipotentiostat was configured for sweeping the potential with a two electrode system by shorting the counter and reference electrodes. A data acquisition card and Labview software were employed to capture the data.

### **3.1.5 Junction Characterization (*I-V* curves)**

A Pine bipotentiostat was used to sweep the potential and measure the current across the junction (*I-V* curve). The bipotentiostat was configured for *I-V* analysis by shorting the counter and reference electrodes, creating a two-electrode system. The potential sweep was limited to +25 mV to –25 mV to prevent electrolysis from changing the junction during characterization. The slope of the curve (conductance) was used to characterize the junction size.

If the current range on the potentiostat was not within a few orders of magnitude of the actual current, the instrument displayed an unusual *I-V* plot. Therefore, the current range was initially set for capturing all junction sizes. After the initial *I-V* plot, the current range was reset for another plot to eliminate the artifact (if present) and obtain better precision by lowering the noise from  $\pm 500$  nA to  $\pm 50$  nA. A data acquisition card and Labview software were employed to capture the data.

## **3.2 Results and Discussion**

### **3.2.1 Directional Electrodeposition (etch/ deposit)**

Atom-scale junctions were formed with major modifications to the auto-terminated (external resistor) directional electrodeposition method reported by Tao *et al.*

By incorporating a microfluidic electrochemical cell, lowering the applied potential, and utilizing a comparator, atom-scale junction formation efficiency and control was significantly improved.<sup>4</sup> Rather than submerging Au wires in bulk solution, an elastomeric polydimethylsiloxane (PDMS) microfluidic flow cell was sealed over the junction of two Au thin film electrodes and filled with 0.2 M HCl electrolyte.<sup>12-15</sup> With an applied potential between the electrodes, Au was oxidized from the anode (etched), “directed” across the inter-electrode gap, and then reduced (deposited) on the cathode. Another strong acid, HClO<sub>4</sub>, was attempted to avoid any possibility of specific adsorption of Cl<sup>-</sup>, but HClO<sub>4</sub> was not able to support dissolution of the anode. Specific adsorption of Cl<sup>-</sup> ions from the HCl electrolyte was not a problem for the intended application, because the thiol analytes preferentially adsorb to Au.

The first thin Au film electrode sample examined did not have enough Au on the anode (50 nm thick) to close the ~30 μm inter-electrode gap with directional electrodeposition. Within one minute at  $V_{appl} = 1.2$  V, the anode area in the channel (with electrolyte) was virtually etched away, and the cathode had very little visible deposition, concluding that the electrode thickness and spacing was not adequate for closing the inter-electrode gap (Figure 3.3). With 150 nm thick electrodes, the inter-electrode gap had to be < 5 μm in order to form a junction before the anode was etched away with directional electrodeposition. Therefore, for electrodes fabricated with an inter-electrode gap > 5 μm, the gap was reduced by poisoning the working electrodes at 0.3 V (referenced system) to electrodeposit Au from solution (2.0 mM Au<sup>+3</sup>). As the Au was deposited from solution to the working electrodes, the current through the Pt counter electrode increased from nA to μA until the deposition was terminated after ~25 min at a

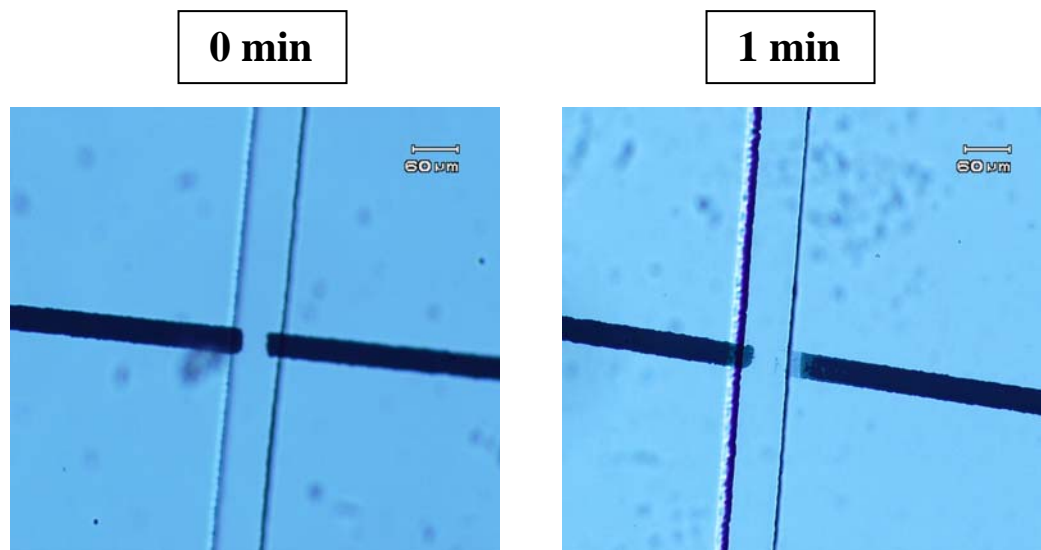


**Figure 3.3:** Optical micrographs (10X) of 50 nm thick electrodes straddled by a PDMS microfluidic channel. After one minute of applying 1.2 V between the electrodes, the anode was completely etched away, and the cathode had some observable deposition. Not enough Au was sputtered to close the  $\sim 28 \mu\text{m}$  gap.

<5  $\mu\text{m}$  gap (Figure 3.4). In their published work, Tao *et al.* did not need to reduce the inter-electrode gap of 10-20  $\mu\text{m}$ , because the 25  $\mu\text{m}$  diameter Au wire electrodes had dramatically more Au than 150 nm thin Au film electrodes.<sup>4</sup> After electrodepositing Au from solution to reduce the fabricated inter-electrode gap, the leads were connected to the two-electrode potentiostat for applying a potential (typically  $\sim 1.0$  V) between the electrodes to etch Au from the anode and deposit on the cathode, *i.e.* directional electrodeposition. If the anode began thinning before the junction was formed (observed with 40X objective), the anode and cathode leads were switched to build up the thinning electrode, rather than repeating the three electrode (referenced) deposition step. However, switching leads often caused some of the deposited Au to be released as nanoparticles that interfered with junction formation. The direction electrodeposition was terminated automatically when the measured voltage passed through a level preset either by an external resistor or a comparator.

### 3.2.1.1 Resistor-Terminated Directional Electrodeposition

The resistor-terminated method of forming atom-scale junctions is represented by  $V_{gap} = V_{appl} \times [R_{gap} / (R_{gap} + R_{ext})]$  (Figure 3.1).  $R_{ext}$  must be sufficiently large to lower  $V_{gap}$  below the effective electrolysis (etch/deposit) potential while  $R_{gap} > 12.9$  k $\Omega$ . Per this relationship, if  $V_{appl}$  is lowered,  $V_{gap}$  goes below the effective potential with  $R_{gap}$  final closer to  $R_{ext}$ . In other words, if  $R_{ext}$  is the same for two runs, the run with the larger  $V_{appl}$  should grow a thicker junction.<sup>16</sup> Therefore, the main two parameters that determined whether the deposition was stopped before, just at, or after contact are the applied potential,  $V_{appl}$ , and the external resistance,  $R_{ext}$ . [The role of electrode kinetics must also be carefully considered in order to control the termination of directional electrodeposition

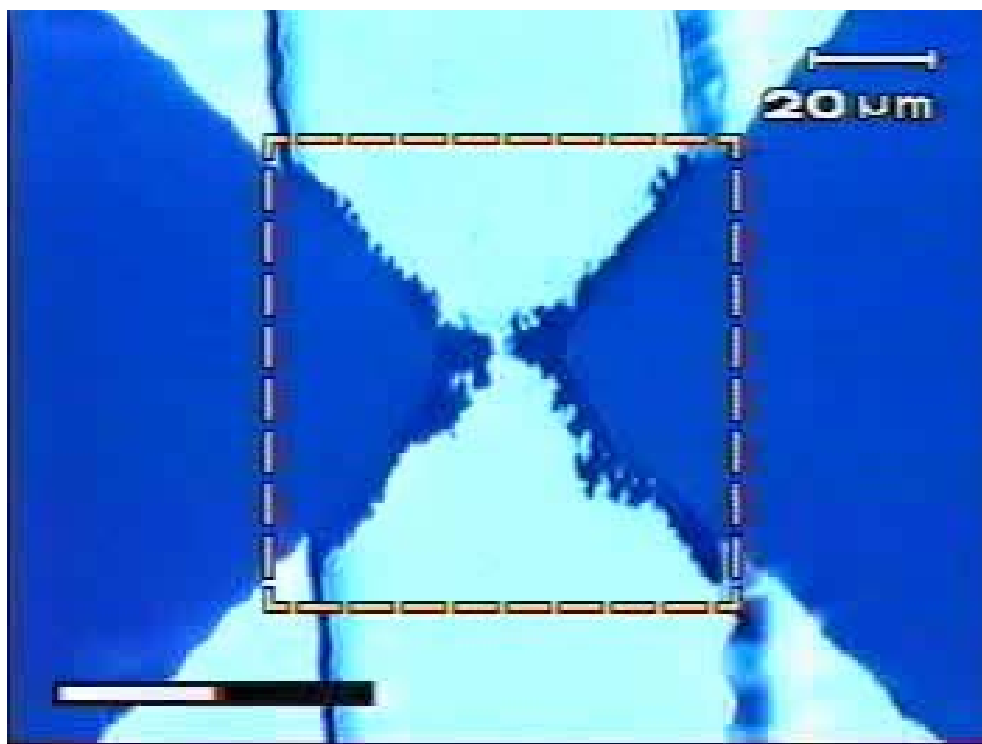


**Figure 3.4:** Optical micrograph (40X) of 150 nm thick electrodes straddled by a PDMS microfluidic channel. Au was electrodeposited on both electrodes until the gap was  $<5\ \mu\text{m}$  to ensure the gap could be closed with directional electrodeposition. The Au deposition solution was  $2.0\ \text{mM}\ \text{Au}^{+3}$ . With the working electrodes set at  $0.3\ \text{V}$  (referenced), reducing the gap from  $\sim 28\ \mu\text{m}$  to  $\sim 5\ \mu\text{m}$  took about 25 minutes.

at a single atom junction.] By applying a potential between the electrodes, directional electrodeposition transferred Au atoms from the anode to the cathode in the two-electrode cell. The electrodes were placed in series with an external resistor to form a voltage divider network that slowed the growth near contact. When the inter-electrode gap was larger than tunneling distance ( $\sim 5$  nm), the gap impedance remained large and constant, with the current flowing across the gap being essentially a leakage current. The magnitude of the leakage current varied from run to run because it depended on the electrode geometry and inter-electrode gap distance. Upon reaching the tunneling regime, the gap impedance fell, and the voltages being dropped across each of the series resistances began to change, *i.e.*  $V_{gap} = V_{appl} \times [R_{gap}/(R_{gap} + R_{ext})]$ .

In an effort to improve control of the junction formation, directional electrodeposition was used with various  $R_{ext}$  and  $V_{appl}$  settings for adjusting the junction growth rate and size. While theoretically a gap should be formed with a resistance just greater than the conductance quantum ( $12.9$  k $\Omega$ ),  $R_{ext}$  had to be  $\geq 100$  k $\Omega$  with  $V_{appl} = 1.2$  V to stop the directional electrodeposition consistently at a gap. Tao *et al.* had similar results with eight experiments set at  $V_{appl} = 1.2$  V and  $R_{ext} = 100$  k $\Omega$ , forming gaps from  $39.7$  to  $172$  k $\Omega$  with an average of  $55$  k $\Omega$  (poor control).<sup>4</sup> To improve this termination control reported by Tao *et al.*, the current density was lowered by decreasing the applied potential below  $1$  V, which resulted in conductance steps of approximately  $1 G_0$ , *e.g.* from  $1.3 G_0$  to  $2.2 G_0$  with  $R_{ext} = 17.1$  k $\Omega$  and  $V_{appl} = 0.2$  V. A final, steady junction conductance was measured as low as  $1.3 G_0$  ( $R_{ext} = 32.47$  k $\Omega$ ,  $V_{appl} = 0.5$  V). However, even with the increased control associated with lowering  $V_{appl}$  below Tao's reported  $1.2$  V, several attempts were still required to form junctions  $< 5 G_0$  with directional

electrodeposition, *i.e.* the run-to-run variations are too great for using a calibration curve ( $R_{ext}$  vs  $R_{gap}$ ) to determine a set external resistance for a precise junction size at a set  $V_{appl}$ .

### 3.2.1.2 Comparator-Terminated Directional Electrodeposition

The lack of control of the resistor-terminated method motivated the development of the comparator-terminated method of forming atom-scale junctions (Figure 3.2). The external resistor was still utilized to slow the growth near termination point. The applied potential,  $V_{appl}$ , was lowered to decrease the rate of reaction (current density) near the termination point. To compensate for error and the mechanical relay response time, the comparator was initially set to trigger at a current slightly lower than the calculated atom-scale junction current, *e.g.* a set point of 2.5  $\mu\text{A}$  was used if the calculated current was 2.7  $\mu\text{A}$ . If a gap formed at the lower setting, the current was adjusted slightly higher until an atom-scale junction was formed. This approach prevented forming a thicker junction than desired. Although an electronic relay would have a faster response time, electronic relays have leakage currents large enough to alter the atom-scale junction with unwanted electrolysis.<sup>17</sup> A typical atom-scale junction formation run involved directional electrodeposition between the electrodes with an initial applied potential of  $\sim 0.9\text{ V}$  ( $R_{ext} = 100\text{ k}\Omega$ ). Once tunneling current was measured ( $d < 5\text{ nm}$ ),  $V_{appl}$  was lowered to  $< 0.5\text{ V}$  in order to slow the electrolysis near the preset termination current (no electrolysis was measured at potentials  $< 0.2\text{ V}$ ), enabling the comparator-triggered mechanical relay to respond before the atom-scale junction changed significantly. With  $V_{appl} < 0.5\text{ V}$ , the electrolysis was slow enough to form atom-scale junctions ( $< 5\text{ G}_0$ ) by manually terminating the electrolysis after the current jump, indicating contact. The applied potential was initially set higher ( $\sim 0.9\text{ V}$ ) to narrow the gap efficiently, because a larger



current density increases the rate of reaction, before slowing the electrolysis for controlled atom-scale junction formation.

**Figure 3.5** compares the resistor-terminated and comparator-terminated junction formation methods, demonstrating the improved control obtained with the comparator-terminated method. The histogram of 1  $G_0$  attempts does not include gaps formed or junctions broken before the  $I$ - $V$  measurement was obtained (~20% of total attempts). Furthermore,  $I$ - $V$  measurements for all of the  $> 500 G_0$  junctions were not obtained and therefore not included in the histogram (~20 % of total attempts). For perspective, the empirical atomic diameter of Au is 0.27 nm, which is the thickness of a 1  $G_0$  atomic chain. Based on estimates discussed below, a 10  $G_0$  junction is 1.05 nm thick, and a 45  $G_0$  junction is 2.46 nm thick.

### 3.2.2 Junction Characterization

A number of features of the current-time behavior shown in **Figure 3.6** confirm atom-scale junction formation.<sup>10</sup> First, a tunneling current regime, indicating a gap size of  $< 5$  nm, was encountered at *ca.* 50 s, and is similar to observations reported by Tao and coworkers.<sup>4</sup> When  $V_{appl} < 1.1$  V, the rate of reaction was slow enough to resolve tunneling current above the noise. Later, a ground loop in the data acquisition set up was corrected, which reduced the noise by a factor of 100. The time between the commencement of directional electrodeposition and observation of tunneling current was dependent on the starting gap size, applied potential, and external resistance. For example, **Figure 3.7b** has a longer pre-tunneling current baseline (~200 s) than **Figure 3.6** (~100 s). Second, the jump in conductance at contact is clearly evident. Third, conductance step behavior is resolvable, consistent with the atomic-scale nature of the

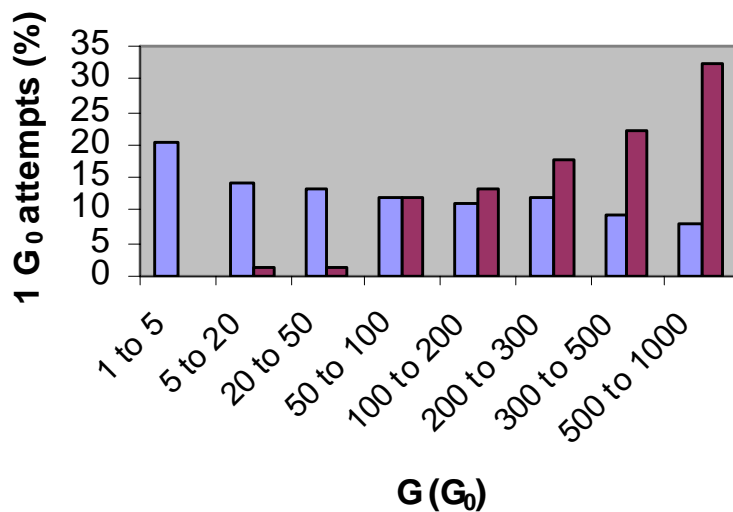


**Figure 3.5:** A histogram of a portion of the  $1 G_0$  junction formation attempts comparing the resistor-terminated (red/ right column) and comparator-terminated (blue/ left column) methods. The histogram clearly demonstrates that the comparator-terminated method is superior for atom-scale junction formation. The columns represent the percent of the  $1 G_0$  junction formation attempts that resulted in a certain junction size as represented by the conductance ( $G$ ); included 68 of the resistor-terminated attempts and 99 of the comparator-terminated attempts. The conductance values are the inverse slope of the junction  $I$ - $V$  curves.

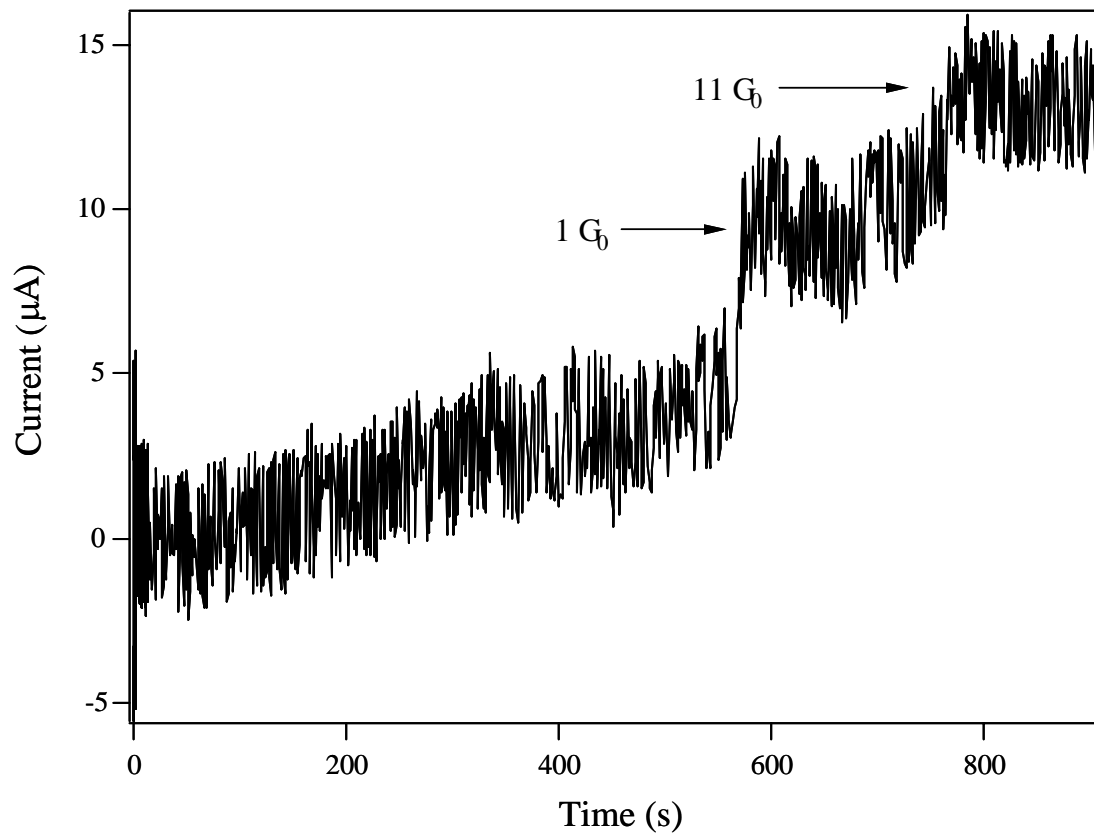


**Figure 3.6:** Current-time plots during the formation of a Au junction ( $V_{appl} = 0.3$  V,  $R_{ext} = 22.5$  k $\Omega$ ). Tunneling current is measured from  $\sim 50$  s up to the contact point. The contact point is labeled ( $1 G_0$ , 9  $\mu$ A).

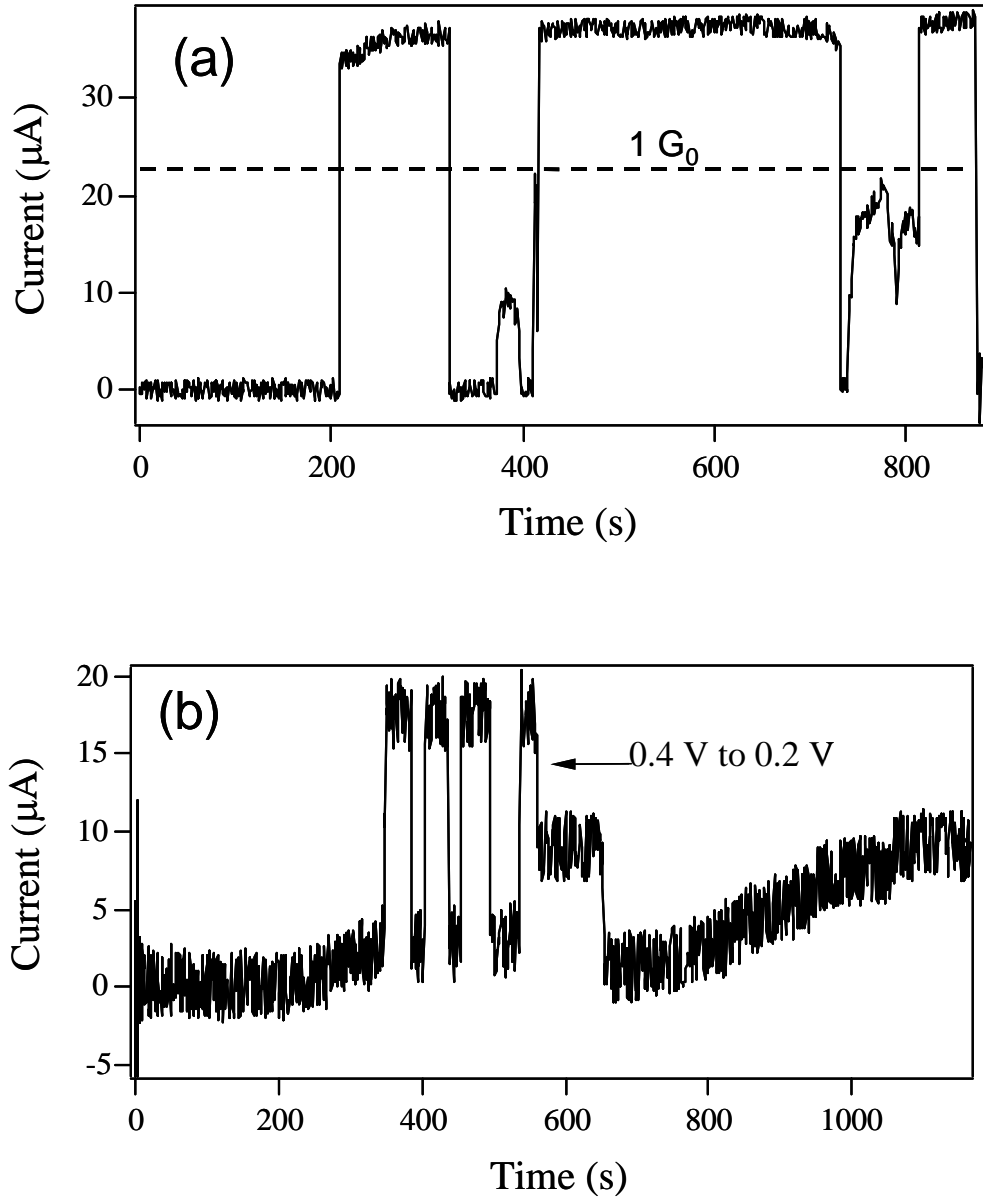


**Figure 3.7:** Current-time plots during atom-scale junction formation, which demonstrate the effect of electromigration of Au atoms and controlling the electromigration with external parameters. (a) Junctions formed ( $G > 1 G_0$ ) and broken ( $G \sim 0$ ) spontaneously at  $V_{\text{appl}} = 0.66 \text{ V}$ ,  $R_{\text{ext}} = 17 \text{ k}\Omega$ . (b) Current-time plot with  $V_{\text{appl}}$  lowered from 0.4 V to 0.2V at *ca.* 570 s ( $R_{\text{ext}} = 22.45 \text{ k}\Omega$ ).

junction. In most experiments, the electrolysis was too rapid to resolve the conductance step behavior leading up to the final comparator-terminated junction size. At  $V_{appl} < 0.8\text{V}$ , conductance steps were periodically resolved. Fourth, the electromigration induced junction breaks have been observed in several experiments and offer another clear signature of atomic-scale behavior. **Figure 3.7** shows examples of junctions breaking under an applied potential  $> 0.4\text{ V}$ , likely due to electromigration. In **Figure 3.7b**, note that the junction breaks back to the tunneling regime ( $< 5\text{ nm gap}$ ) in the time range of 375 to 500 s.

With an  $I$ - $V$  curve (**Figure 3.8**), the ohmic-nature of the atom-scale junctions at voltages between  $\pm 25\text{ mV}$  was observed, and the conductance magnitude was measured. The slope of the  $I$ - $V$  curve is  $R_{gap}$ . The inverse of  $R_{gap}$  is the conductance ( $G$ ) of the junction, which can be expressed in units of conductance quantum ( $G_0$ ) by simply dividing  $G$  by  $G_0$ . The final conductance values of the atom-scale junctions are presented in units of the conductance quantum,  $G_0$ , to emphasize the small size of these atom-scale junctions.

With a comparator setting designed to produce junctions of  $1\ G_0$  and  $V_{appl} < 0.5\text{ V}$ , atom-scale junctions are routinely produced with a conductance  $< 3\ G_0$ , and conductance steps were occasionally measured (**Figure 3.6**). Although the experiment was never optimized to form sharp conductance quantum staircases, the observation of conductance steps in **Figure 3.6** is clearly statistically significant. Taking the observations in the 50 s just prior to the 1st jump ( $I_{avg} = 4.2\ \mu\text{A}$ ,  $s = 1.6\ \mu\text{A}$ ) and comparing them to current data for 50 s in the middle of the first plateau ( $I_{avg} = 9.0\ \mu\text{A}$ ,  $s = 2.2\ \mu\text{A}$ ) yields a  $t$ -statistic,  $t = 20.0$ , which can be compared with a  $t = 3.506$  for the

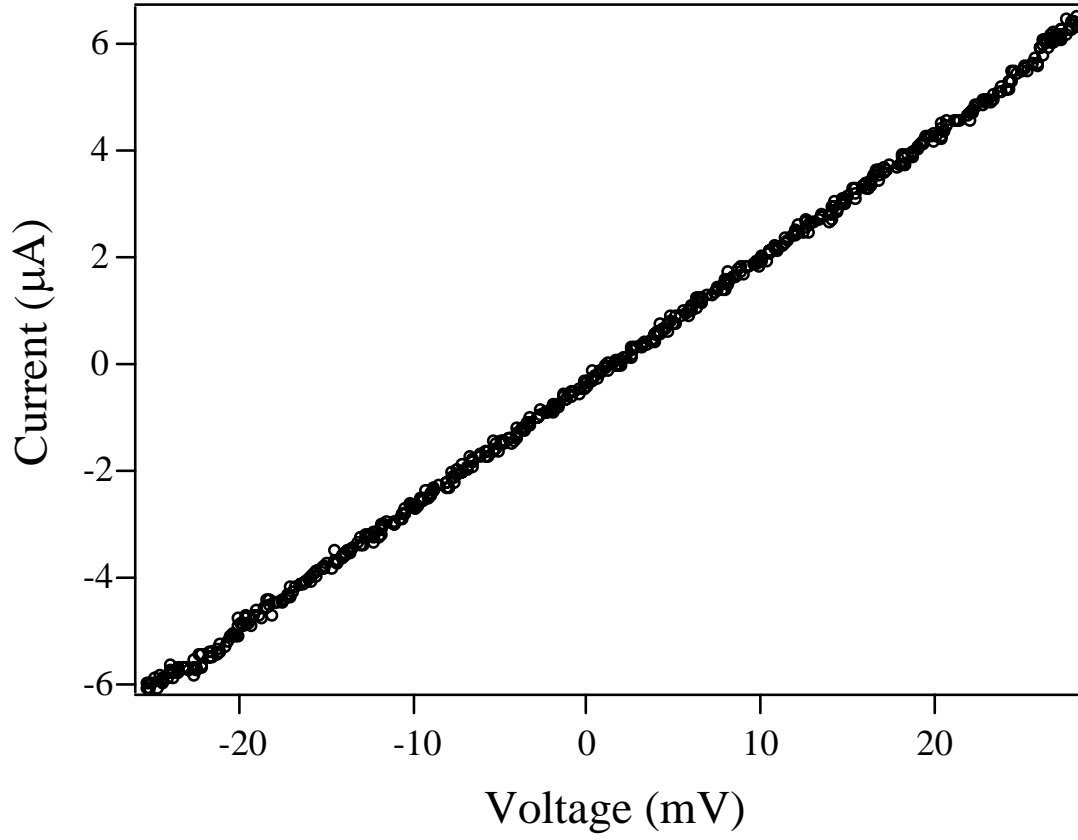


**Figure 3.8:** Current-potential (I-V) plot for an atom-scale junction formed with  $V_{appl} = 0.2$  V and  $R_{ext} = 17$  k $\Omega$ . The slope of the curve yields  $G = 3.0 G_0$ .

99.95% level for 50 degrees of freedom (interpolated from values given for 40 and 60 degrees of freedom).<sup>18</sup> Clearly, the statistical significance of the difference is established even in the presence of the noise. A similar analysis can be made for the difference between the 1st and 2nd plateaus to show that it is also statistically significant. The unusually high noise in **Figure 3.6** was eventually traced to a ground loop in the data acquisition set up. After fixing the ground loop, the noise was reduced by a factor of 100.

### 3.2.3 Electromigration

Electromigration of Au atoms is dependent on  $V_{appl}$  and can cause atom-scale junctions to break, thereby producing a 1 to 2 nm gap.<sup>4,6,19-22</sup> **Figure 3.7** shows a series of electromigration-induced breaks, each of which is followed by re-growth of the contact. The signal behavior below 1  $G_0$  is consistent with previous observations in the literature, which have been attributed to etching and depositing of single atoms in a gap small enough to exhibit tunneling current.<sup>4</sup> When  $V_{appl}$  was decreased from 0.4 V to 0.2 V ( $R_{ext} = 22.45 \Omega$ ), recurring contact breaking and reforming ceased. With  $V_{appl} = 0.2$  V, the current density is low enough to allow a steady current increase until contact, rather than a jump to contact (**Figure 3.7b**). After contact, the junction can continue to thicken as in **Figure 3.7a** from about 200 to 250 s (5.5  $G_0$  to 11.4  $G_0$ ). Pursuant to these observations, experiments were typically run with  $V_{appl} = 0.3$  V and  $R_{ext} = 100$  k $\Omega$  to avoid electromigration and to slow electrolysis near the calculated termination current for better comparator-terminated junction control.

### 3.2.4 Dendritic Growth

In the high voltage regime,  $V_{appl} > 1.2$  V, dendritic growth was often observed (**Figure 3.9**).<sup>10,23-25</sup> Initially, the dendrites were thought to be NaCl crystals from the Au

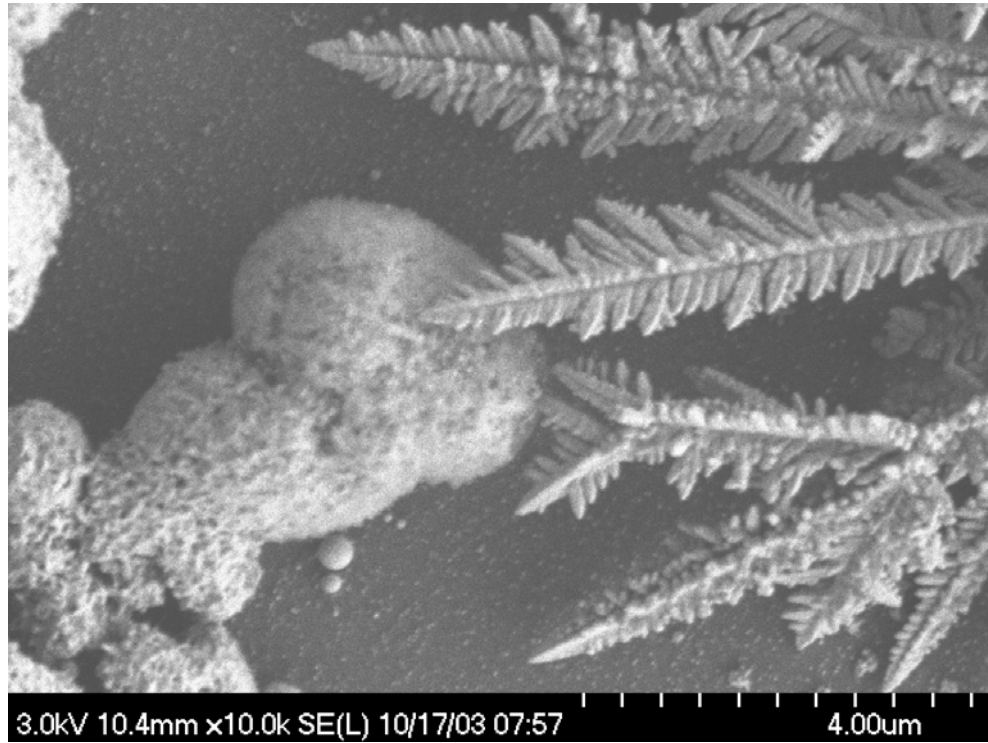


**Figure 3.9:** SEM image of the junction area between Au thin film electrodes. The rounded Au clusters on the left are from electrodepositing  $[\text{Au}^{+3}]$  to narrow the fabricated inter-electrode gap. The dendritic growth on the left is from resistor-terminated directional electrodeposition ( $R_{ext} = 50 \text{ k}\Omega$ ,  $V_{appl} = 1.2 \text{ V}$ ), which etched Au from the anode (left) and deposited it on the cathode (right).



deposition solution. However, the dendrites persisted after changing electrolytes (0.1M NaCl to 0.05M HClO<sub>4</sub>) and even held up to several hours of stirring and heating. Energy dispersive spectroscopy (EDS) identified the dendrites as Au. The metal dendrites reportedly form due to diffusion-limited mass transport; therefore, the space between the electrodes apparently has mass transfer limitations.<sup>23-25</sup> The large metal surface area of dendrites may be of interest for other applications, such as catalysis.

### 3.2.5 Junction Size

The junction size was estimated by measuring the resistance ( $R_{gap}$ ) during and after the formation of the junction. By configuring the circuit with two digital multimeters, one for the current ( $I$ ) and one for  $V_{gap}$ , the junction size ( $R_{gap} = V_{gap}/I$ ) was monitored during formation. The junction size ( $R_{gap}$ ) was also determined after formation with a current-voltage ( $I$ - $V$ ) measurement, using a Pine bipotentiostat. Between  $\pm 25$  mV, the  $I$ - $V$  curve was ohmic for Au junctions, and the slope is  $R_{gap}$ . The inverse of  $R_{gap}$  is the conductance ( $G$ ) of the junction, which can be expressed in units of conductance quantum ( $G_0$ ) by simply dividing  $G$  by  $G_0$ . **Figure 3.8** shows an ohmic  $I$ - $V$  curve for a  $3.0 G_0$  atom-scale junction. For junctions with a length less than the electron mean free path of Au (3.8 nm),<sup>26</sup> the conductance varies only with the width of the junction.

Typically, non-integer  $G_0$  values are observed and are attributed to the fact that the measured  $G_0$  value assumes no tunneling of non-conducting modes, nor scattering of electrons around the atom-scale junction.<sup>27,28</sup> Furthermore, non-uniform junction thicknesses would also result in non-integer  $G_0$  measurements, especially with directional electrodeposition across inter-electrode gaps larger than a few nanometers. For example,

a  $2 G_0$  row of Au atoms in series with a  $3 G_0$  row of Au atoms would result in a measurement of  $G = 1.2 G_0$ . Non-integer  $G_0$  conductance measurements could also result from more than one atom-scale junction in parallel, although we believe that the highly spatially anisotropic nature of the electric field in the directional electrodeposition and the exponential dependence of current on gap size in the tunneling regime make multiple parallel contacts unlikely.

A simple method of estimating the thickness of an atom-scale junction involves stacking Au atom chains in an energetically favorable triangular geometry with face-centered cubic (fcc) spacing, treating each  $G_0$  as one row of Au atoms. This correlation was based on the work of Ohnishi *et al.* who imaged two parallel rows of Au atoms and measured a conductance of  $2 G_0$ , giving a junction width of 0.58 nm based on nearest-neighbor spacing.<sup>29</sup> Non-uniform atom-scale junctions would cause measured conductances to deviate from integer  $G_0$  values, e.g. a  $2 G_0$  section of Au atoms in-series with a  $3 G_0$  section would result in  $G = 1.2 G_0$ . Another source of error comes from rounding fractional  $G_0$  values for determining the number of Au atom rows. The rows are stacked in a triangular geometry, which has a low surface area (energetically favorable). Although molecular-dynamics simulations found helical packing to be the most stable structure for free-standing Au nanowires with a diameter  $< 0.6$  nm, face-centered cubic (fcc) spacing was used to estimate the stacking of Au atom chains on a substrate.<sup>30</sup> The Au atom chain stacking method will only be used for junctions  $< 5 G_0$  to satisfy the theoretical boundary condition that the thickness must be “comparable” to the Fermi wavelength ( $\lambda_F$ ), which is 0.52 nm for Au.<sup>10,31</sup> By stacking five chains of Au atoms in a triangular geometry with fcc spacing, the estimated junction thickness was

calculated at 0.56 nm. This  $5 G_0$  limit is supported experimentally, since conductance measurements typically only have about five clear conductance steps. Therefore, the fcc-configured atomic chain stacking method of estimating junction thickness ties the theoretical and experimental together. When the length is estimated at 100 nm, the fcc-configured atomic chain stacking method is comparable to results from the bulk resistivity equation,  $R_{gap} = \rho l/A$ , where  $A$  is the cross sectional area of a triangle ( $d^2$ ),  $\rho$  is  $2 \times 10^{-6} \text{ cm}\Omega$ ,  $l$  is the length, and  $R_{gap}$  is from an  $I$ - $V$  measurement. However, for a junction with quantized conductance, the length can not exceed the electron mean free path for Au (3.8 nm).<sup>10,26</sup> A chain of Au atoms that is less than  $\sim 3.8$  nm in length will have a conductance of  $1 G_0$ . Furthermore, tunneling current measurements and scanning electron microscope (SEM) images are consistent with a junction length  $< 5$  nm (Figure 3.10). With an estimated junction length of 5 nm, the bulk metal resistivity equation gives a junction thickness of 0.20 nm for a  $5 G_0$  junction. Since the thickness is less than the diameter of a Au atom, the bulk resistivity equation is clearly not accurate for atom-scale junctions.

### 3.2.6 Junction Isolation

Ideally, an atom-scale junction would consist of a 1D Au atom chain grown between the two electrodes, isolated for SEM and atomic force microscopy (AFM) analysis. Dendritic growth from the directional electrodeposition step and rough features from the initial Au deposition (gap reduction) hinder isolation of the atom-scale junction (Figure 3.9). By lowering the applied potential below 1.2 V, the dendritic growth was eliminated. Junction isolation was also obstructed by Au deposition from solution. To improve junction isolation, only one electrode was built up with Au deposition.

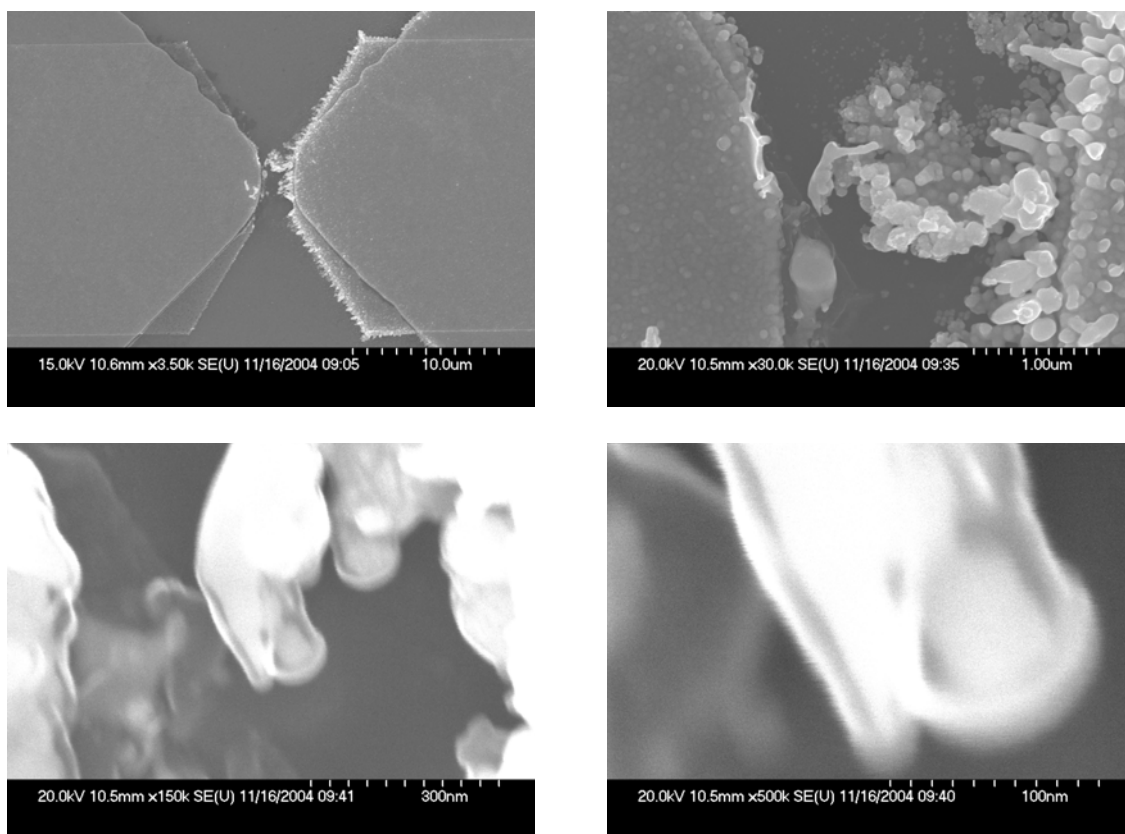


**Figure 3.10:** SEM images at successively higher magnification of the same atom-scale gap between Au thin film electrodes on a silicon substrate. The gap was  $< 5$  nm since tunneling current was measured (in 0.2 M HCl) both before and after imaging. The anode and cathode were overlapped ( $x = 20$  nm,  $y = 90$  nm), making it difficult to measure the gap size. By analyzing the contrast between the overlapped metal features, an inter-electrode gap of  $< 5$  nm could be estimated in the x-y plane.

However, the deposition took twice as long (~45 min) to narrow the gap to  $< 5\ \mu\text{m}$  (Figure 3.11). Notice in Figure 3.11 how the Au deposited directly from solution is in clusters (right), while the electrodeposited Au (left) is much more uniform, yielding better isolation and a more stable junction. To avoid Au deposition directly from solution entirely, great effort was made to form starting inter-electrode gaps  $< 5\ \mu\text{m}$ . First, the photolithography process was optimized (incremental etching then lift-off) with a Cr mask made from a 5080 dpi transparency film, providing a  $\sim 28\ \mu\text{m}$  gap. Next, a commercially produced laser drawn Cr mask was used with metal lift-off photolithography, allowing a  $\sim 3\ \mu\text{m}$  gap.

The  $3\ \mu\text{m}$  inter-electrode gap allowed for greater isolation of the junction area because junctions could be formed without first depositing extra Au (from solution) on the electrodes. However, even without deposition to reduce the inter-electrode gap, AFM analysis demonstrated that direction electrodeposition still built up 350 nm of Au on the edge of the 150 nm thick cathode during junction formation (Figure 3.12). The electrode edge height ( $\sim 500\ \text{nm}$ ) to junction length aspect ratio prevented a direct junction thickness measurement with AFM (50 nm wide tip). Regardless, the silicon or glass substrates are too rough (1-2 nm) for AFM to provide accurate information on the thickness of an atom-scale junction.

While reducing the inter-electrode gap, a correlation between junction length and stability was observed, with shorter junctions holding up better to solution flow in the microfluidic channel, likely due to the larger Ti adhesion layer and decreased Au deposition. With inter-electrode gaps  $> 5\ \mu\text{m}$ , Au clusters formed during deposition sometimes break off and lodge in the junction; note the uneven deposition distribution in

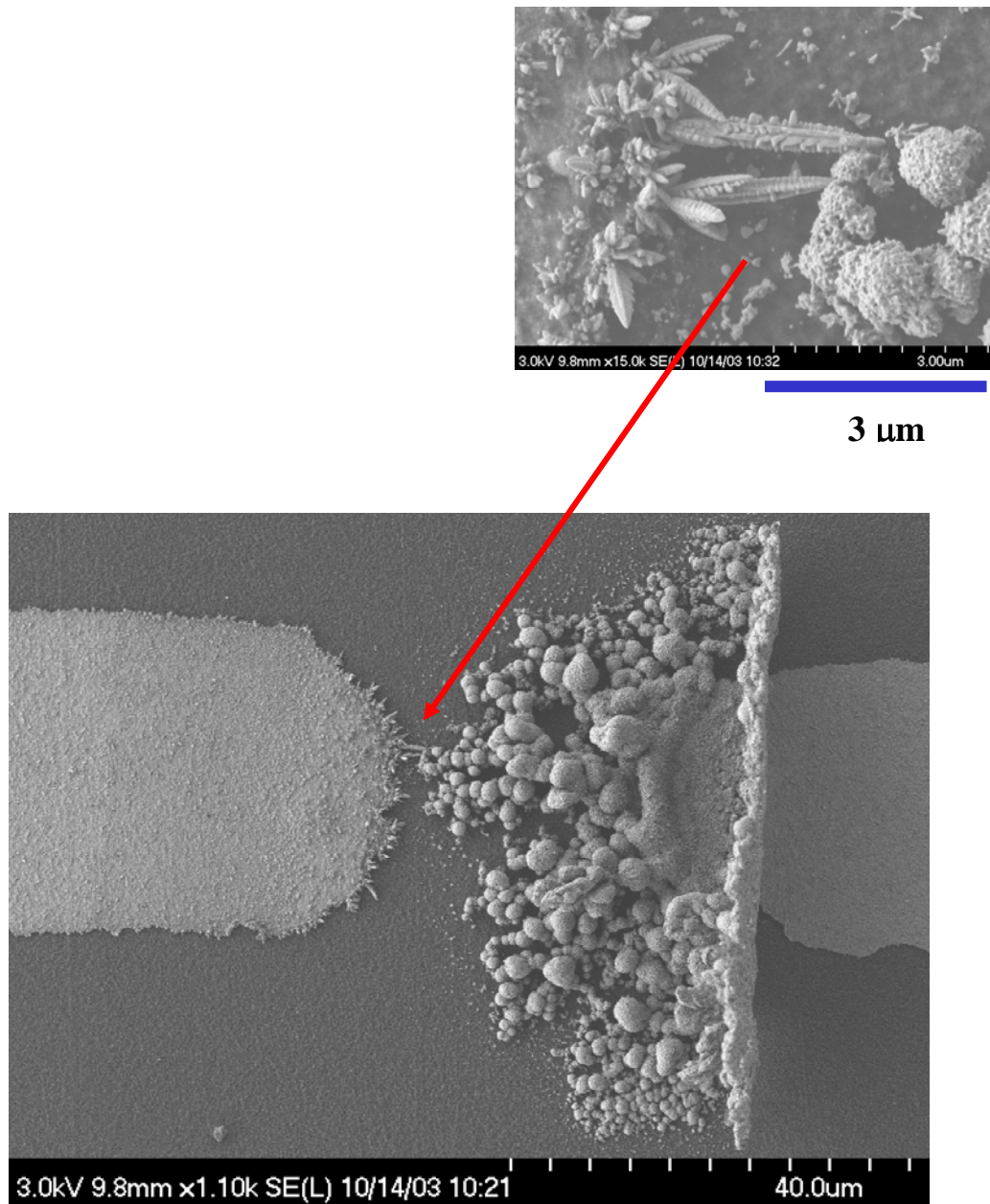


**Figure 3.11:** SEM images of junction area between Au thin film electrodes. Deposited  $[\text{Au}^{+3}]$  on just one electrode (right) to reduce the gap from the fabricated spacing of  $\sim 28 \mu\text{m}$  to  $< 5 \mu\text{m}$ . Then, resistor-terminated directional electrodeposition was employed ( $V_{\text{appl}} = 1.2 \text{ V}$ ,  $R_{\text{ext}} = 30 \text{ k}\Omega$ ) to form a junction by etching from the anode (right) and depositing on the cathode (left).

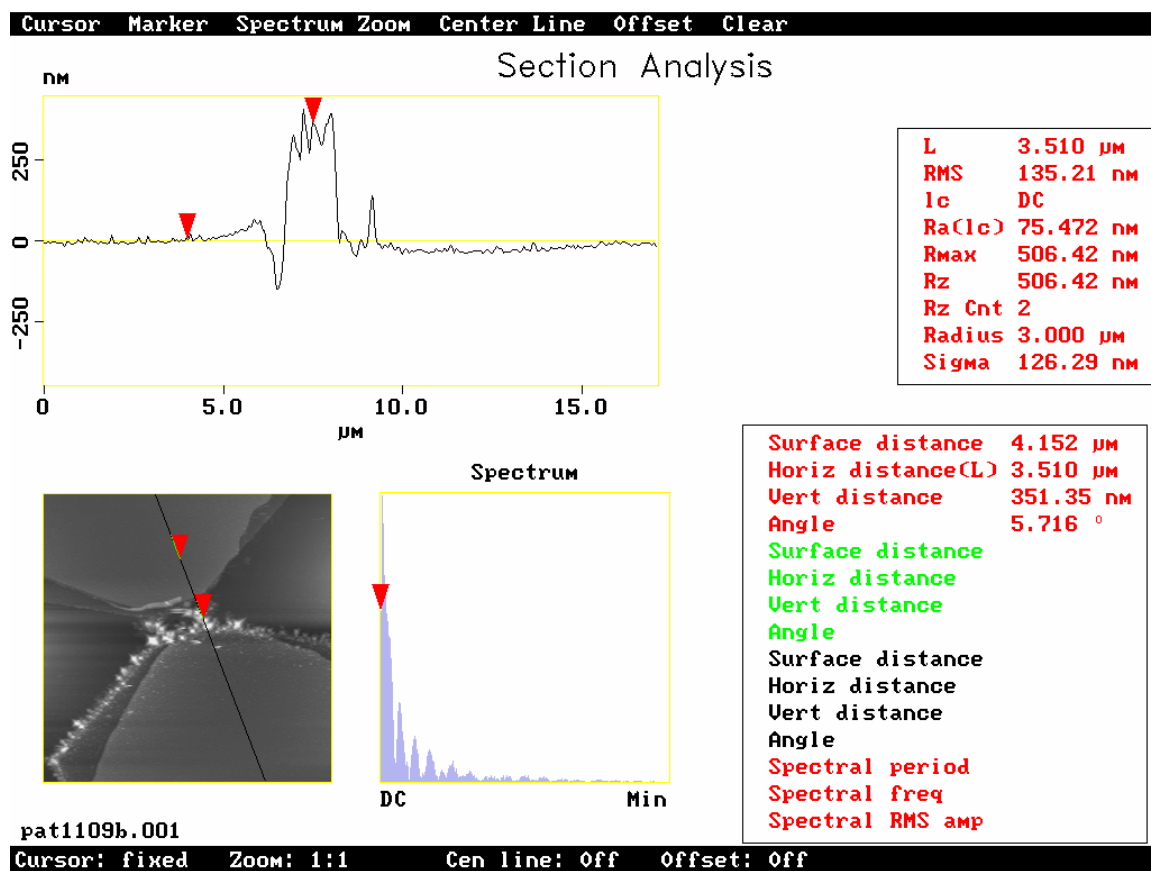


**Figure 3.12:** AFM analysis of a junction formed between nanotips ( $< 40$  nm spacing,  $\sim 40$  nm thick) on thin film Au electrodes ( $\sim 3$   $\mu\text{m}$  spacing,  $\sim 150$  nm thick). The fabricated inter-electrode spacing ( $< 40$  nm) did not require Au deposition before forming the junction with directional electrodeposition. Therefore, directional electrodeposition was solely responsible for depositing  $\sim 350$  nm of Au on the edge of the 150 nm thick cathode, during junction formation.

Figures 3.10 and 3.11. Therefore, electron beam lithography was considered to minimize the starting size of the inter-electrode gap, thereby removing the need for Au deposition, which in turn improved stability.

Electron beam lithography produced 40 nm thick Au electrode “nanotips” with an inter-electrode gap < 45 nm gap (Figure 2.4).<sup>32</sup> Unfortunately, the electron beam lithography fabricated nanotips broke off when the Au contact pads were added with photolithography. This was likely due to charge build up or potential difference between the pads and the insulating glass substrate. To alleviate this problem, a few samples were fabricated in which the nanotips were shorted out with a 10-20 nm wide Au strip. The nanotips did not break in this configuration, thereby confirming the charge build up problem. Switching to a more conductive silicon <100> substrate (test grade, boron doped) eliminated the charging problem and consequently the breaking. Processing on a silicon <100> wafer also improved electron beam processing time, because the wafer was easily broke into nine 25 mm square samples after writing the e-beam nanotips and aligning the contact pads (Cr mask). Therefore, a commercially produced laser drawn Cr mask with nine electrodes was designed and purchased. Also, the silicon substrate eliminated the charging during SEM imaging, improving the resolution (< 5 nm) of SEM images used to estimate the junction length for calculating the junction thickness (Figure 3.10). The e-beam lithography nano-scale starting gap allows atom-scale junctions to be formed much quicker than with photolithography micron-scale starting gaps (~1 min vs ~30 min).



### 3.2.7 Junction Imaging

The substrate type impacts the ability to image the junction area with transmission electron microscopy (TEM) and scanning electron microscopy (SEM). First, TEM was attempted, since this instrument has a resolution of ~2 nm features, compared to SEM best-case resolution of ~5 nm. Growing on a metal TEM grid would have shorted out the junction and not allowed directional electrodeposition. Therefore, attempts were made to grow a junction on a non-conductive substrate, bind it up with an Lx112 epoxy, and use a diamond cutter to section out the junction for the TEM grid. The glass substrate could not be used because the glass would damage the diamond cutter. Therefore, the electrode was processed on alternate substrates. The preferred TEM sample substrate is Lx112 epoxy, but it was difficult to build devices with this material. The epoxy had to be poured thin enough for transmitted light microscopy to monitor the junction growth, yet thick enough to handle the photoresist processing (~1 mm thick). Processing on an aclar substrate was much simpler, because it is purchased in thin, transparent sheets (~1 mm) and withstood photoresist processing. Furthermore, the aclar allowed for well isolated dendritic junction formation (Figure 3.13). Unfortunately, the aclar bowed during TEM sample preparation, and the junction was not captured in the sectioning. Further TEM attempts to assess junction morphology were abandoned.

With the glass substrate, SEM could not resolve the junction due to charging of the insulating glass substrate (Figure 3.14). The SEM resolution was dramatically improved by sputter coating the sample with 7 nm of AuPd. However, coating the sample with 7 nm of metal is not acceptable when trying to resolve nanometer scale features. Therefore, a more conductive substrate, silicon, was employed which allowed

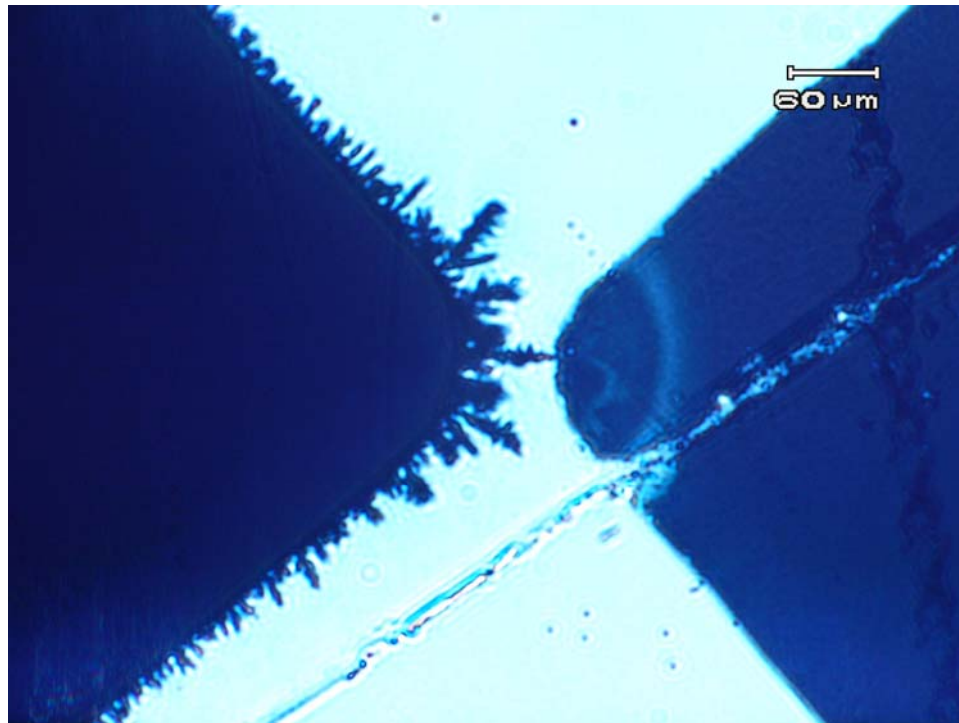


**Figure 3.13:** Optical micrograph (10X) of junction formed between thin film Au electrodes on aclar. Aclar facilitated the electrochemical formation of well isolated junctions.

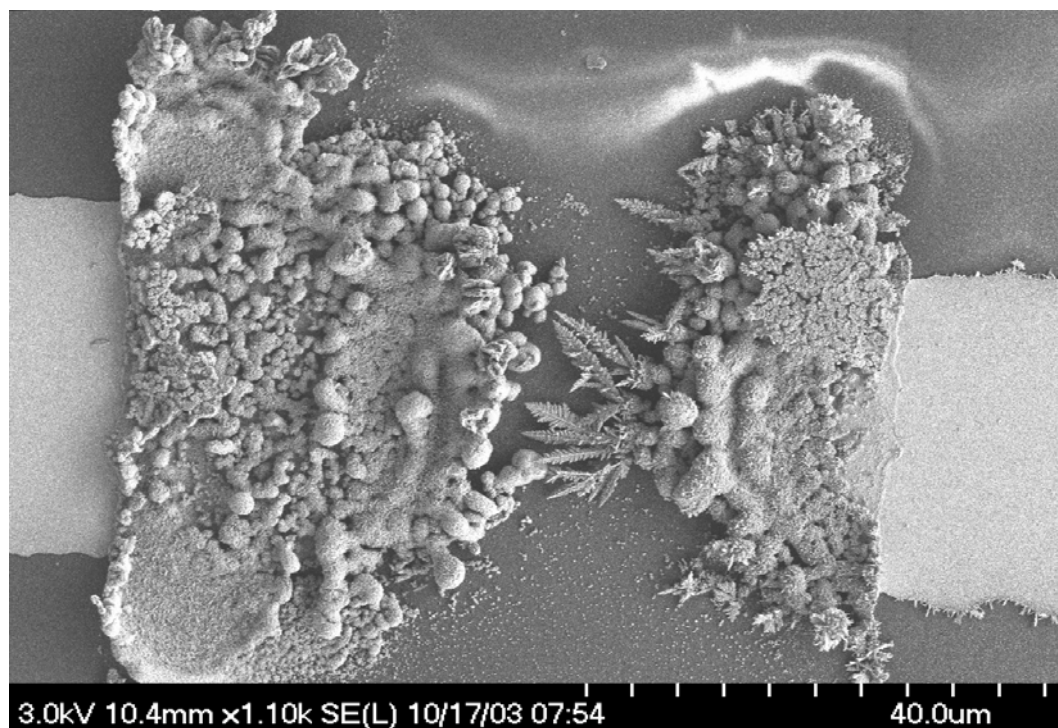


**Figure 3.14:** SEM image of junction area between Au thin film electrodes on a glass substrate. Charging of the insulating glass substrate reduced the SEM resolution (top of image).

the junction area to be imaged with the SEM ( $\sim 5$  nm features). However, even the junctions formed across the  $3\text{ }\mu\text{m}$  gap were not strong enough to be transported to the SEM instrument. Therefore, an atom-scale gap was imaged with the SEM, with the size determined by measuring tunneling current ( $< 5$  nm gap). In the SEM image, the anode and cathode were overlapped in the vertical direction ( $x = 20$  nm,  $y = 90$  nm), making it difficult to measure the exact gap size (Figure 3.10). By analyzing the contrast between the overlapped metal features, an inter-electrode gap of  $< 5$  nm could be estimated in the x-y plane, but the contrast does not allow the inter-electrode spacing to be quantified in the z plane. However, tunneling current was again measured between the electrodes after the SEM imaging, supporting an inter-electrode gap of  $< 5$  nm. Therefore, if an atom-scale junction was formed between the overlapped electrodes, the length would be  $< 5$  nm. This length estimate is comparable to the  $G_0$  length boundary condition ( $<$  mean free path), which is 3.8 nm for a Au atom-scale junction.<sup>26</sup>

### 3.2.8 Junction Regeneration

Regenerability is a key capability for use of any readout approach in a sensor platform, so the possibility of regenerating the atom-scale junction after use was explored. Three approaches to breaking the junction were used; high fluid flow rate, electrochemical etching, and current density-induced breaking. Breaking with a high flow rate ( $> 1.8$  mL/min) would indiscriminately break the junction with different size gaps, usually several micrometers. Electrochemical etching removes Au from the electrodes within the microfluidic channel in a spatially indiscriminant manner, decreasing the life of the electrode, *i.e.* the number of growth-test-break cycles that can be sustained by a single structure. On the other hand, the current density-induced

breakdown approach was quite robust. Typically, the atom-scale junctions broke when the applied potential across the junction exceeded 300-400 mV with the break power proportional to the contact thickness ( $R_{gap}$ ), viz. **Figure 3.15**. However, some thicker junctions broke with only a 250 mV sweep, typically occurring after several break/reform cycles. Hypothetically speaking, the nano-particle debris from Au electrodeposition or previously broken junctions may have interfered with the junction formation, forming thicker and weaker junctions. This possibility was supported by the observation of stronger junctions, indicated by sustaining a larger potential sweep, after a high flow rate rinse of the microfluidic channel, which likely removed loose Au nano-particles. The break size obtained by current-induced breaking was almost always less than the resolution of the 40X optical microscope objective ( $\sim 1 \mu\text{m}$ ), and breaks were confirmed with a baseline  $I$ - $V$  signal of  $\pm 50$  nA (15 Hz). Sometimes the break size was just a few nanometers, based on the observation of tunneling current across the inter-electrode gap. The break size was likely based on junction thickness, and the variable break size was indicated by the varying length of time required to reform the junction under the same conditions. Typically, the break size became larger with each successive break/reform cycle, as determined by micrographs. However, since the electrodes held up to multiple break/reform cycles, exceeding the current-density threshold was the preferred regeneration method.

The electrode regeneration dramatically increased research progress. Without pre-deposition or switching electrodes, the anode was etched away with less than 10 break/reform cycles. The electrode life span was further extended by periodically switching the cathode and anode leads, which extended the electrode life to 30

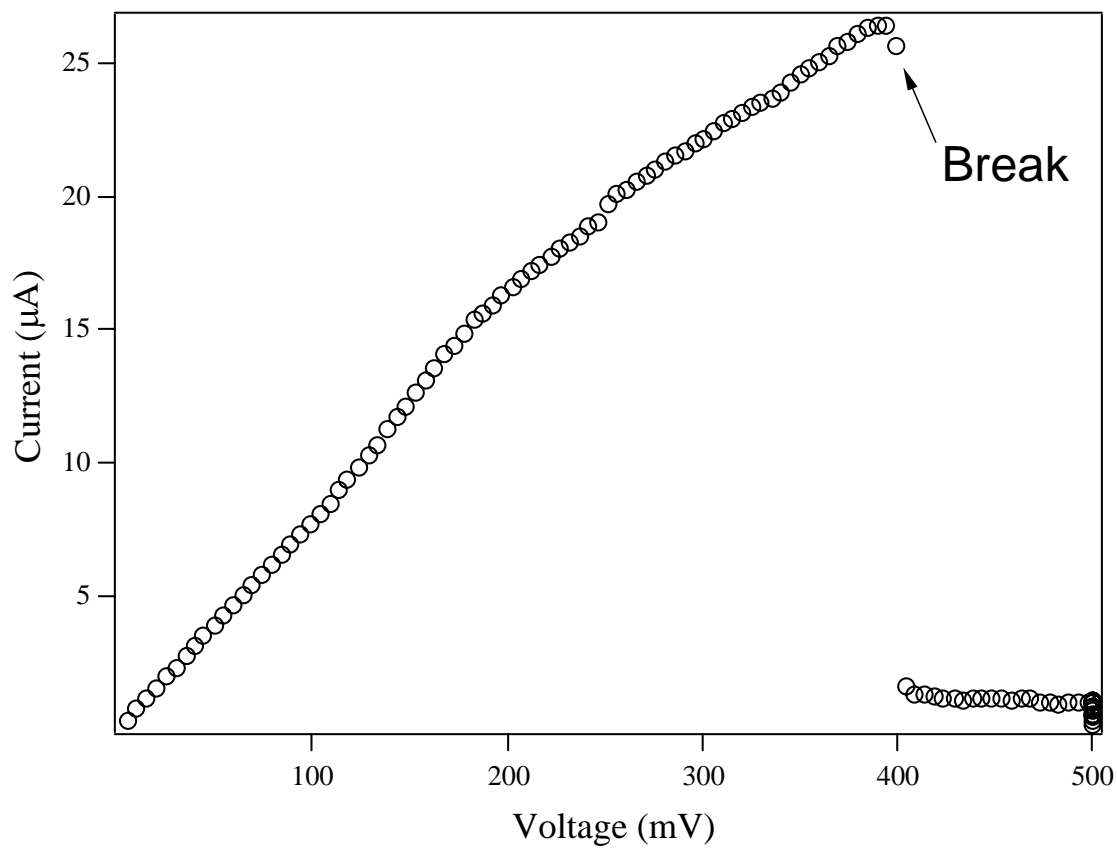


**Figure 3.15:** Current-voltage plot for a regeneration cycle in which current density is ramped up to the point that the junction breaks.

regeneration breaks before the Au anode was etched to the breaking point. Au was also deposited on the electrodes periodically to build them back up. Employing a sacrificial Au counter electrode could expand the electrode life. Electrode longevity is a long-term concern while pursuing a field detection device.

### **3.2.9 Junction Stability**

During the course of experiments aimed at assessing the sensitivity to adsorption of Lewis bases, junction stability became the primary concern. Before employing atom-scale junctions in a field-deployable device, either the analyte must be delivered with less force (0.6 mL/min), or the junction stability must be improved. The interfacial scattering data were obtained after many attempts to introduce analyte without breaking the junction, consuming many samples. In hopes of reducing sample fabrication costs and gaining more interfacial scattering data, efforts were made to stabilize the junction further. First, the analyte solvent was changed from EtOH to H<sub>2</sub>O, because it is less volatile. Second, instead of introducing the analyte to the junction by way of pipet into an open reservoir or vacuum filling a microfluidic channel, the analyte was delivered with less pressure, using a low-flow peristaltic pump at 1.2 mL/min (turbulent flow at 1.5 mL/min). The flow was stopped completely after the analyte filled the channel. Third, the analyte solvent was switched from H<sub>2</sub>O to the directional electrodeposition solvent (HCl). This prevented switching to EtOH for an AC impedance baseline before introducing the analyte that was in EtOH (less junction disturbance). Fourth, rather than removing the PDMS microfluidic channel for thiol desorption, ozone was delivered through the channel, followed by removal of the RSO<sub>3</sub> moieties in EtOH. This also allowed AC impedance measurements during desorption. Fifth, to limit air bubble

disturbance of the junction, the pump was turned off before switching the tubing to a different solution. Sixth, a switch was added for changing the leads between potentiostats to reduce atom-scale junction breakage.

To increase the longevity of the anode and possibly the stability of the junction, comparator-terminated atom-scale junctions ( $< 5 G_0$ ) were formed by depositing Au on the cathode from solution ( $[\text{Au}^{+3}]$ ) without etching the anode. Perchlorate was the electrolyte because etching was not measured with directional electrodeposition, *i.e.* a nanometer scale gap did not change even after applying a potential of 2 V between the electrodes for several minutes. By employing directional electrodeposition with  $[\text{Au}^{+3}]$  in perchlorate, the cathode was poised for deposition without etching the anode. This method improved the electrode longevity but not the stability. The deposited Au builds up on the entire cathode (in the channel) and is likely responsible for reducing the formation control and junction stability. Also, SEM images revealed that the Au is deposited with significant spatial clustering (Figures 3.10, 3.11, and 3.14), which is likely correlated to the rate of deposition as determined by the magnitude of  $V_{\text{appl}}$ .

A concomitant problem is that electrodeposited Au nano-particles break off of the cathode due to the flow of solution through the channel or the potential across the junction. During directional electrodeposition, the potential between the electrode nanotips directs the nano-particles into the gap between the electrodes, interfering with junction formation. As the cathode builds up with electrodeposited Au, larger (less R) and weaker (break with less power) junctions are more likely to form with each subsequent regenerated junction. Rinsing the channel at a high flow rate (high pressure) reduced, but did not eliminate, the negative impact of the nano-particle debris deposition.



The stability was further assessed by using directional electrodeposition (etch/deposit) without any Au deposition from solution. Pre-deposition of Au on the electrodes was not necessary with the e-beam samples, due to the nano-scale starting gap (< 50 nm). This approach demonstrated the best control (efficiency) when forming atom-scale junctions. However, the junctions did not hold up to the introduction of analyte at 0.6 mL/min (10  $\mu$ L/s), which was a flow velocity of 10 cm/s in the channel. Therefore, the stability is not better than the initial method of pre-depositing Au from solution (1  $\mu$ m gap), followed by directional electrodeposition to form the atom-scale junction. Perhaps the pre-deposited Au structures (> 100 nm height) protected the junction area (reduced the flow force) while introducing the analyte.

With the e-beam nano-scale starting gaps, the junction stability did not improve as expected. With a smaller starting gap, the initial junction required less electrodeposited Au and is likely more stable than a junction formed across a larger gap. However, subsequent regenerated junctions did not demonstrate improved stability. Apparently, Au nano-particles debris interferes with the junction formation. The source of the debris is likely Au nano-particles from regenerating the junction, Au nano-particles dislodged from the cathode while changing solutions, or Au nano-particles dislodged from the potential difference across the inter-electrode gap.

### 3.3 References

- (1) EC Walter, BJ Murray, F Favier, G Kaltenpoth, M Grunze, RM Penner: "Noble and coinage metal nanowires by electrochemical step edge decoration" *Journal of Physical Chemistry B* 106 (2002) 11407-11411.

- (2) EC Walter, MP Zach, F Favier, BJ Murray, K Inazu, JC Hemminger, RM Penner:  
"Metal nanowire arrays by electrodeposition" *Chemphyschem* 4 (2003) 131-138.
- (3) A Bard, L Faulkner: *Electrochemical Methods*, John Wiley & Sons, New York,  
1980.
- (4) S Boussaad, NJ Tao: "Atom-size gaps and contacts between electrodes fabricated  
with a self-terminated electrochemical method" *Appl. Phys. Lett.* 80 (2002) 2398-  
2400.
- (5) JM Krans, JM Vanruitenbeek, VV Fisun, IK Yanson, LJ Dejongh: "The Signature  
of Conductance Quantization in Metallic Point Contacts" *Nature* 375 (1995) 767-  
769.
- (6) CZ Li, HX He, NJ Tao: "Quantized tunneling current in the metallic nanogaps  
formed by electrodeposition and etching" *Appl. Phys. Lett.* 77 (2000) 3995-3997.
- (7) HE van den Brom, JM van Ruitenbeek: "Quantum suppression of shot noise in  
atom-size metallic contacts" *Physical Review Letters* 82 (1999) 1526-1529.
- (8) CZ Li, NJ Tao: "Quantum transport in metallic nanowires fabricated by  
electrochemical deposition/dissolution" *Appl. Phys. Lett.* 72 (1998) 894-896.
- (9) RHM Smit, Y Noat, C Untiedt, ND Lang, MC van Hemert, JM van Ruitenbeek:  
"Measurement of the conductance of a hydrogen molecule" *Nature* 419 (2002)  
906-909.
- (10) N Agrait, AL Yeyati, JM van Ruitenbeek: "Quantum properties of atomic-sized  
conductors" *Physics Reports-Review Section of Physics Letters* 377 (2003) 81-  
279.
- (11) PW Atkins: *Physical Chemistry*, W.H. Freeman and Company, New York, 1990.

- (12) BH Jo, LM Van Lerberghe, KM Motsegood, DJ Beebe: "Three-dimensional micro-channel fabrication in polydimethylsiloxane (PDMS) elastomer" *Journal of Microelectromechanical Systems* 9 (2000) 76-81.
- (13) TC Kuo, DM Cannon, YN Chen, JJ Tulock, MA Shannon, JV Sweedler, PW Bohn: "Gateable nanofluidic interconnects for multilayered microfluidic separation systems" *Anal. Chem.* 75 (2003) 1861-1867.
- (14) TC Kuo, DM Cannon, MA Shannon, PW Bohn, JV Sweedler: "Hybrid three-dimensional nanofluidic/microfluidic devices using molecular gates" *Sensors and Actuators a-Physical* 102 (2003) 223-233.
- (15) DC Duffy, JC McDonald, OJA Schueller, GM Whitesides: "Rapid prototyping of microfluidic systems in poly(dimethylsiloxane)" *Anal. Chem.* 70 (1998) 4974-4984.
- (16) R Saliba, C Mingotaud, F Argoul, S Ravaine: "Morphological control of gold electrodeposits grown at the gas-liquid interface" *J. Electrochem. Soc.* 150 (2003) C175-C183.
- (17) CZ Li, A Bogozi, W Huang, NJ Tao: "Fabrication of stable metallic nanowires with quantized conductance" *Nanotechnology* 10 (1999) 221-223.
- (18) SM Selby (Ed.)<sup>(Eds.)</sup>, CRC Standard Mathematical Tables. Chemical Rubber Co, Cleveland, 1970.
- (19) WS Liang, M. P.; Bockrath, M.; Long, J. R.; Park, H.: "Kondo resonance in a single-molecule transistor" *Nature* 417 (2002) 725-728.

- (20) H Park, AKL Lim, AP Alivisatos, J Park, PL McEuen: "Fabrication of metallic electrodes with nanometer separation by electromigration" *Appl. Phys. Lett.* 75 (1999) 301-303.
- (21) H Park, J Park, AKL Lim, EH Anderson, AP Alivisatos, PL McEuen: "Nanomechanical oscillations in a single-C-60 transistor" *Nature* 407 (2000) 57-60.
- (22) JP Park, A. N.; Goldsmith, J. I.; Chang, C.; Yaish, Y.; Petta, J. R.; Rinkoski, M.; Sethna, J. P.; Abruna, H. D.; McEuen, P. L.; Ralph, D. C.: "Coulomb blockade and the Kondo effect in single-atom transistors" *Nature* 417 (2002) 722-725.
- (23) E Benjacov, P Garik: "The Formation of Patterns in Nonequilibrium Growth" *Nature* 343 (1990) 523-530.
- (24) YC Zhu, HG Zheng, Q Yang, AL Pan, ZP Yang, YT Qian: "Growth of dendritic cobalt nanocrystals at room temperature" *J. Cryst. Growth* 260 (2004) 427-434.
- (25) GL Ding, SN Tewari: "Dendritic morphologies of directionally solidified single crystals along different crystallographic orientations" *J. Cryst. Growth* 236 (2002) 420-428.
- (26) D Erts, H Olin, L Ryen, E Olsson, A Tholen: "Maxwell and Sharvin conductance in gold point contacts investigated using TEM-STM" *Physical Review B* 61 (2000) 12725-12727.
- (27) J Martinek, W Nawrocki, M Wawrzyniak, J Stankowski: *Molecular Phys. Reports* 20 (1997) 157.

- (28) J Hogsved: "Study of Quantized Conductance using a Mechanically Controlled Break Junction in Air at 300 K" *Master Thesis* (1997) Goteborg Department of Experimental Physics.
- (29) H Ohnishi, Y Kondo, K Takayanagi: "Quantized conductance through individual rows of suspended gold atoms" *Nature* 395 (1998) 780-783.
- (30) BL Wang, SY Yin, GH Wang, A Buldum, JJ Zhao: "Novel structures and properties of gold nanowires" *Physical Review Letters* 86 (2001) 2046-2049.
- (31) R Landauer: "Spatial variation of currents and fields due to localized scatterers in metallic conduction (reprinted from IBM Journal of Research and Development, vol 1, 1957)" *Ibm Journal of Research and Development* 44 (2000) 251-259.
- (32) P Rai-Choudhury (Ed.)^(Eds.), Handbook of Microlithography, Micromachining, and Microfabrication. SPIE Press, 1997.

## CHAPTER 4

### SENSING WITH ATOM-SCALE JUNCTIONS

#### 4.1 Introduction

Analytical chemistry seeks to detect chemicals at low concentration with various techniques, with the ultimate goal of single molecule detection. Single molecule detection would save lives through early detection of chemical agents like dimethylaminoethoxy-cyanophosphine oxide (Tabun nerve agent), which Iraq used on Iran in 1984.<sup>1</sup> Fluorescence and atomic force microscopy techniques have been used for detecting single molecules.<sup>2-4</sup> Although an electrically transduced sensing scheme for single molecule detection is not found in the literature, Cui *et al.* exposed functionalized boron-doped Si nanowires to various chemical environments and measured the conduction change through the nanowire.<sup>3,5</sup> Since this field of research has vast potential but is filled with unanswered questions, single molecule detection was pursued by measuring the change in conduction in a Au atom-scale junction while introducing an analyte through a microfluidic channel. The literature has several reports for fabricating Au atom-scale junctions electrochemically<sup>6-13</sup> but not in a microfluidic flow cell.

This work was ultimately motivated by Zhang *et al.* who demonstrated that the chemisorption of thiol on a thin Au film ( $8\text{nm} < d < 80\text{nm}$ ) induced a ~2% change in the resistivity of the film.<sup>3,14,15</sup> The experiment measured the in-plane voltage drop (constant current) while introducing octanethiol. The chemisorbed octanethiol caused interfacial scattering that changed the conductivity of the thin Au film. The measurement noise was 61 nV in the assembly curve saturation region (Figure 4.1). Typically, a discernable

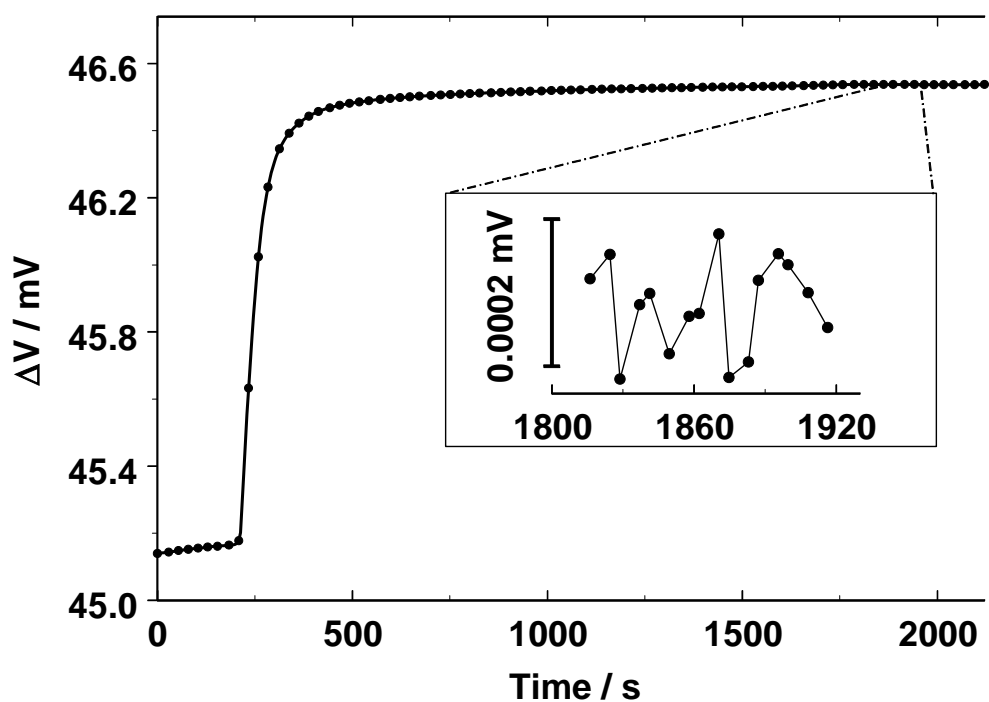


**Figure 4.1:** Change in voltage plot that is proportional to the change in resistance across a  $1 \text{ cm}^2$  area of an  $\sim 50 \text{ nm}$  thick Au film, resulting from the introduction of  $1 \text{ mM}$  octanethiol ( $\text{C}_8\text{H}_{17}\text{SH}$ ) in EtOH. The chemisorbed octanethiol caused interfacial scattering that changed the conductivity of the thin Au film. The noise was  $61 \text{ nV}$  in the assembly curve saturation region (inset).<sup>3,14</sup>

signal must be three times larger than the noise level, so the minimum detectable signal ( $\Delta V_{min}$ ) is approximately 183 nV. The change in voltage due to a monolayer of octanethiol ( $\Delta V_{monolayer}$ ) was 1.3 mV. Therefore, the minimum detectable change in octanethiol coverage ( $\Delta \Gamma_{min}$ ) is

$$\Delta \Gamma_{min} = (\Delta V_{min} / \Delta V_{monolayer}) = 1.4 \times 10^{-4} \text{ monolayer}$$

For a 1-cm<sup>2</sup> thin Au film area with a typical alkanethiol surface coverage of  $4 \times 10^{14}$  molecules/cm<sup>2</sup>, the number of molecules required for a detectable signal is calculated as follows.

$$\Delta \Gamma_{min} \times (4 \times 10^{14} \text{ molecules/cm}^2) \times 1 \text{ cm}^2 = 5.6 \times 10^{10} \text{ molecules}$$

If the results of this experiment hold at the nano-scale, a 40 nm x 40 nm area on a Au thin film would enable the discernment of single molecule adsorption and desorption events. By depositing octanethiol on a 150 nm by 800 nm nanofilm (~ 20 nm thick), Swint *et al.* were able to discern the presence of 3000 molecules (Figure 4.2). This improved mass detection limit motivated the research to the next level, fabrication of atom-scale junctions for the pursuit of single molecule detection.

Chemisorption of alkanethiols on a Au atom-scale junction caused interfacial scattering that changed the conductance with a resulting signal large enough to discern a molecule population difference of a single molecule (discussed below). Atom-scale junctions may provide the means of developing the first electrically transduced sensing scheme with single molecule detection capability.



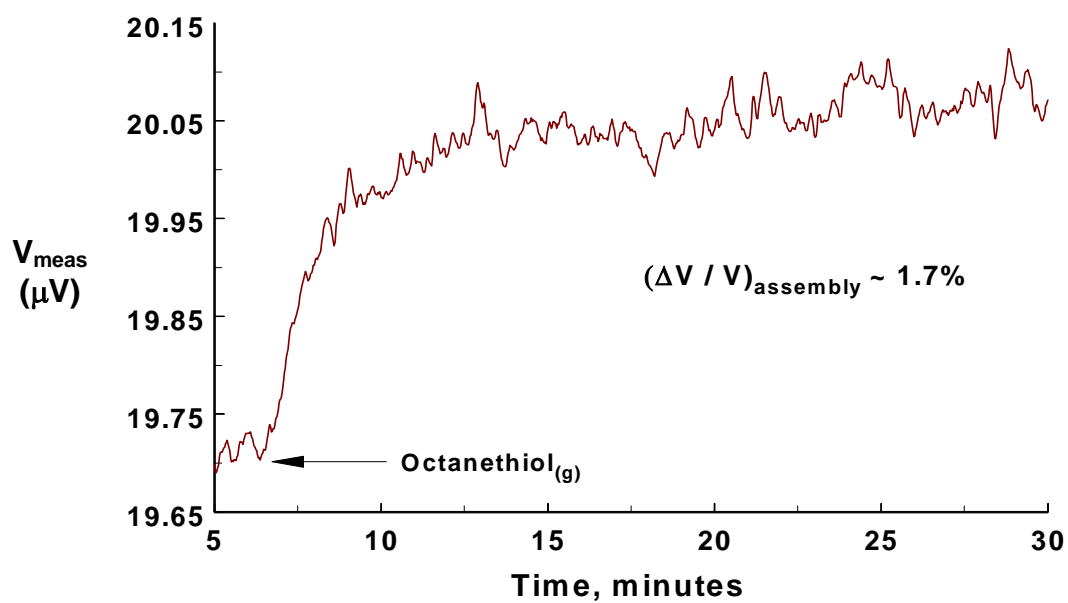


**Figure 4.2:** Change in voltage plot that is proportional to the change in resistance across a 150 nm x 800 nm area of an ~ 20 nm thick Au film, resulting from the introduction of gaseous octanethiol.<sup>3</sup>

## 4.2 Experimental Methods

A Stanford Research Systems model SR830 DSP AC lock-in amplifier was used for impedance measurements to sense chemisorption on electrochemically fabricated Au atom-scale junctions. The lock-in measured the impedance change of a 5 kHz signal (10 mV amplitude) through the atom-scale junction in the analyte solvent for a background measurement. Then, the impedance was measured through the atom-scale junction while introducing 10 mM hexadecanethiol (HDT) or 3-mercaptopropionic acid (MPA) in either EtOH or 0.2 M HCl. After the impedance change equilibrates, analyte solvent is reintroduced to determine how much of the signal is due to physisorption. Rather than removing the PDMS microfluidic channel for thiol desorption, ozone was delivered through the channel.  $O_3$  oxidizes RSH to  $RSO_3^-$  moieties, and the labile sulfonates are rinsed away with EtOH. The AC impedance was measured during thiol desorption.

## 4.3 Results and Discussion

The goal of this work was to fabricate regenerable atom-scale junctions for detecting small mass amounts of Lewis base adsorbates (*e.g.* thiols), with sensing based on impedance change from chemisorption. The measured impedance change was attributed entirely to the atom-scale junction, because the resistance in a typical atom-scale junction (4.6 k $\Omega$ ) was orders of magnitude larger than the electrode pads (0.85  $\Omega$ ). Furthermore, impedance change was not measurable when adsorbing thiol on just the 150 nm thick contact pads. To isolate the impact of the chemisorption on the junction, the impedance was measured through the junction in the analyte solvent before (background) the analyte was introduced. Since the impedance did not change significantly after removing the analyte and reintroducing just the analyte solvent, physisorption was

apparently not a major factor, which was consistent with other studies on the stability of RSH on Au.

The regenerable atom-scale junctions were used to measure the effects on the conductance properties of the adsorption of small numbers of Lewis base molecules. The structures were first tested by exposure to a stable long-chain Lewis base, HDT. Later, the structures were exposed to a water-soluble, short-chain thiol, MPA, which could be used to evaluate pH impact on the interfacial scattering. To maximize sensitivity, atom-scale junctions with  $G < 3 G_0$  were initially used for detection of chemisorbed HDT. However,  $< 3 G_0$  junctions rarely held up to the introduction of analyte, so thicker junctions ( $6.2 G_0$  and  $513.4 G_0$ ) were used with MPA. A number of precautions were exercised (discussed below) to ensure an optimum measurement of the interfacial scattering effect on the conductance (impedance change) in the atom-scale Au junctions.

#### **4.3.1 Introducing Analyte**

Initially, the atom-scale junction was formed in a 5  $\mu\text{L}$  PDMS reservoir to prevent disturbing the junction when vacuum-filling through the microfluidic channel. Unfortunately, delivering the analyte to the junction by way of pipet also disturbed the junction. Therefore, a peristaltic pump was set up to deliver the analyte to the junction at the lowest setting of 0.6 mL/min (turbulent at 1.5 mL/min). Occasionally, air bubbles were introduced when changing solutions with the pump, which caused a change in the AC impedance. This change in AC impedance was likely due to a junction disturbance associated with a change in pressure.

Even at the lowest setting, the peristaltic pump created pressure in the 100  $\mu\text{m}$  wide/ 50  $\mu\text{m}$  deep channel that significantly changed the impedance ( $\sim 5\%$ ), requiring a

pressure release valve, constant flow rate (since plotting  $\Delta Z$ ), or larger channel. The pressure release valve would add another variable to the experimental set up. A constant flow rate increased the probability of disturbing the junction, as opposed to simply turning off the flow after the analyte reaches the junction. Incorporating a wider channel (1 mm wide/ 50  $\mu\text{m}$  deep) allowed for an effective flow rate range without a measurable impedance change. Furthermore, the 1 mm channel width was simple to align over the junction and provided access to more anode Au when forming atom-scale junctions with directional electrodeposition. Atom-scale junctions in the 1 mm wide channel typically held up to flow rates between 0.6 and 1.8 ml/min.

#### **4.3.2 AC Impedance Measurements**

An AC lock-in amplifier allowed the change in impedance from chemisorbed analyte to be determined by measuring the potential drop across the atom-scale junction. The AC lock-in detects the specific frequency and phase of a signal that is relative to a reference signal, thereby eliminating all noise contributions from all other non-referenced frequencies and phases. By using a high frequency signal (5 kHz), the AC lock-in mitigates against  $1/f$  noise, making AC measurements preferable to DC measurements. Continuous data acquisition was accomplished by collecting the lock-in output signal with an A/D data acquisition card.

Impedance has a reactive and resistive component. Initially, the analyte solvent was EtOH, because it dissolves HDT and has a minimal reactive component in the AC impedance measurements. To obtain a baseline for the AC impedance measure, the electrolyte used in the formation of the junction (0.2 M HCl) was exchanged with EtOH, initially with a pipet (eventually with a peristaltic pump). Adequate exchange of HCl for

EtOH took between 5-10 pipet exchanges of  $\sim 1/3$  the volume of the 5  $\mu\text{L}$  reservoir. Only  $1/3$  the volume of the reservoir was exchanged at a time to prevent disturbing the junction. The electrolyte was considered to be adequately removed when the impedance did not change significantly as the frequency was changed, indicating that the vast majority of the reactive electrolyte was removed. Since the junction was typically only stable for a few minutes, the solvent exchange step would often result in the junction breaking before the analyte was introduced. The extra time and disturbance from this step was avoided by simply using 0.2 M HCl as the electrolyte for forming the junctions and as the analyte solvent. The large reactive component of HCl was factored out by using the normalized change in impedance measurement ( $\Delta Z/Z_0$ ).

#### 4.3.3 Interfacial Electron Scattering

The chemisorption of thiols on Au causes a dramatic change in interfacial scattering, resulting in a consequent impedance change. Sensitivity is enhanced due to the large surface to volume ratio of the atom-scale junction. To ensure this impedance change ( $\Delta Z/Z_0$ ) was not a result of the junction changing between the  $I$ - $V$  and AC impedance measurements, the junction size ( $G_0$ ) was calculated from the AC impedance measured just before adding analyte. Figure 4.3 shows the normalized change in impedance,  $\Delta Z/Z_0$ , upon introducing 10 mM HDT to a  $2.6 G_0$  atom-scale junction. This result represents one of the experiments where the atom-scale junction held for the introduction of the analyte/EtOH to the 5- $\mu\text{L}$  open PDMS reservoir by pipet. The HCl electrolyte was first changed out with EtOH by pipet in order to get a baseline impedance measurement before adding HDT/EtOH. The reservoir was kept  $1/3$  full to stabilize the junction. HCl and EtOH have AC impedances with widely different reactive

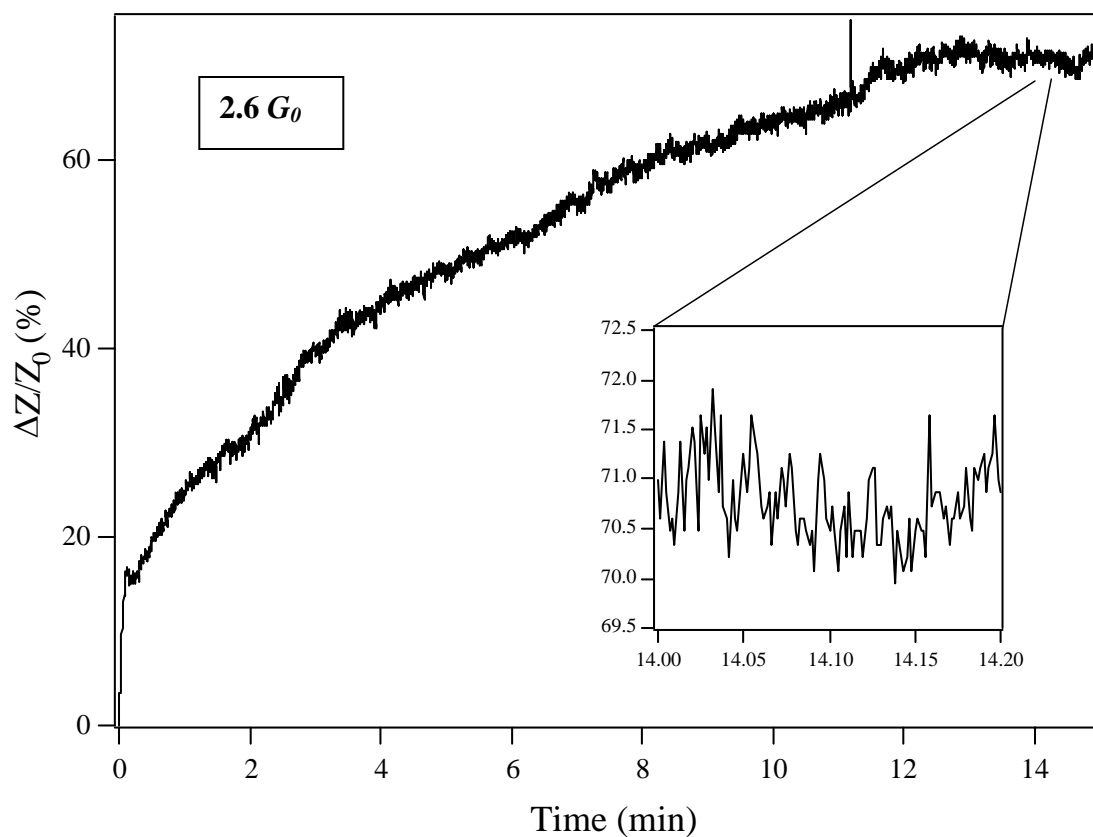


**Figure 4.3:** Plot of the normalized impedance change,  $\Delta Z/Z_o$  (%), at 5 kHz in an atom-scale junction ( $2.6 G_0$ ) after adding 10 mM HDT/EtOH. The inset shows an expanded portion of the saturation region of the curve, which can be used to assess the noise associated with the electrical measurement.

components, so complete change out was determined by measuring the AC impedance. Finally, the HDT/EtOH was introduced to the reservoir, which was 1/3 full with EtOH. The HDT mixed with the EtOH and chemisorbed on the junction area, causing a dramatic change in conductance. This change was not due to junction disturbance based on the fact that the solution exchange steps, averaged over many observations, caused changes in conductance that were only a fraction of the HDT-induced conductance change. For example, the small spike near 12 minutes was from adding additional HDT after EtOH evaporation brought the reservoir level down to about 1/3 full.

Several features of the self-assembled monolayer curve (Figure 4.3) warrant careful examination. First, the signal changes from its pure solvent value to a steady-state value of  $\Delta Z/Z_0 = 71\%$  change in *ca.* 20 min. Both the magnitude and the kinetics of the impedance change are significantly different than observed for the same adsorbate on thin ( $t < 50$  nm) planar Au films, where full monolayer coverage of HDT produces *ca.* 2% change in normalized conductance in *ca.* 2 min. from 1 mM solution.<sup>14,15</sup> Clearly, the fractional effect of each molecule is much larger on the atom-scale junction. To evaluate the impact of any physisorbed thiol on the impedance of the atom-scale junction, the thiol was replaced with pure solvent after assembly. Since this exchange did not result in a significant change in impedance, interfacial scattering from the chemisorbed thiol dominated the measured  $\Delta Z/Z_0$ .

The inset to Figure 4.3 shows the normalized impedance change in the saturation region of the assembly curve,  $\Delta Z/Z_0 = 0.708$  with  $s = 0.004$ , representing a fractional change of  $70.8\% \pm 0.4\%$ . The measured signal for the 2.6  $G_0$  junction does not contain broadband noise because (1) the junction conductance was constant prior to introducing

the HDT, and (2) the magnitude of the measurement noise was below the 244 nA analog to digital precision steps. The noise in the saturation region of the assembly curve represents the sum of the instrumental and environmental noise as well as chemical fluctuations from the dynamic adsorption/desorption of n-alkane thiol molecules to/from the atom-scale junction. Assuming all of the signal variation could be assigned to stochastic fluctuations in surface population, it is interesting to calculate the fluctuation in surface coverage that would give rise to a signal equivalent to the noise in the saturation region, which was less than the 2.44  $\mu\text{V}$  digital steps ( $\Delta Z/Z_0 = \sim 1\%$ ). An estimated thickness and length were used to calculate the number of HDT molecules on the junction, utilizing an approximate HDT coverage of  $4 \times 10^{14} \text{ cm}^{-2}$ . As discussed in section 3.2.5), the junction thickness was estimated by equating one Au atom chain per  $G_0$  and then stacking the chains in a triangular geometry with fcc spacing. For a  $2.6 G_0$  junction, this approach would result in a 0.56 nm thick junction. The length of the  $2.6 G_0$  was estimated at  $< 5 \text{ nm}$ , based on SEM images and complimentary conductance measurements of a different atom-scale junction (section 3.2.7). In addition, the conductance of the junction was in the quantized conductance regime ( $< 5 G_0$ ), which has a length boundary condition of  $\sim 3.8 \text{ nm}$  based on the electron mean free path. Therefore, for an estimated junction size of 5 nm in length and 0.56 nm in thickness, the total surface coverage would be 31 molecules. If most of the noise was attributed to the fluctuation in the HDT surface population, the measured signal variations were consistent with a surface population difference of one molecule, based on  $\delta I \cong 31 \text{ molecules} \times (1\% / 71\%) = < 1 \text{ molecule}$ . When the lock-in amplifier output signal was offset and the



digital-analog conversion range was decreased, the true noise was still below the digital steps of 244 nV ( $\Delta Z/Z_0 = \sim 0.1\%$ ), allowing for even greater sensitivity.

Note that the normal definition of detection limit refers to a species detected in the presence of noise in the background signal, while the background noise for these signals was measured at saturation coverage. Although these calculations do not demonstrate detection limits, nevertheless signal fluctuations in the saturation region clearly define the smallest population differences that can be discerned. This comparison yields valuable insight into the ultimate low-mass detection capabilities that could be attained with these atom-scale junctions.

The analyte was switched from HDT to MPA, because MPA is soluble in water (or aqueous HCl), which is much less volatile than EtOH. This allowed for a more stable environment as the thiol forms a self-assembled monolayer on the junction. The interfacial scattering increased exponentially below  $\sim 20 G_0$ , identifying a threshold region where the resistance change goes from typical thin Au film electrode values ( $\sim 2\%$ )<sup>14,15</sup> to atom-scale junction values above 20% (Figure 4.4). This dramatic increase in sensitivity fuels continued efforts to integrate atom-scale junctions into a field detection system.

#### **4.3.4 Interference with Chemisorption**

Some atom-scale junctions did not demonstrate the dramatic interfacial scattering impact on the resistance, which was attributed to contamination or a limited adhesion layer. Contamination can have a stabilizing effect on the junction but could prevent the chemisorption of analyte.<sup>16</sup> This would explain why some atom-scale junctions held up to the introduction of analyte but did not demonstrate the expected conductance change

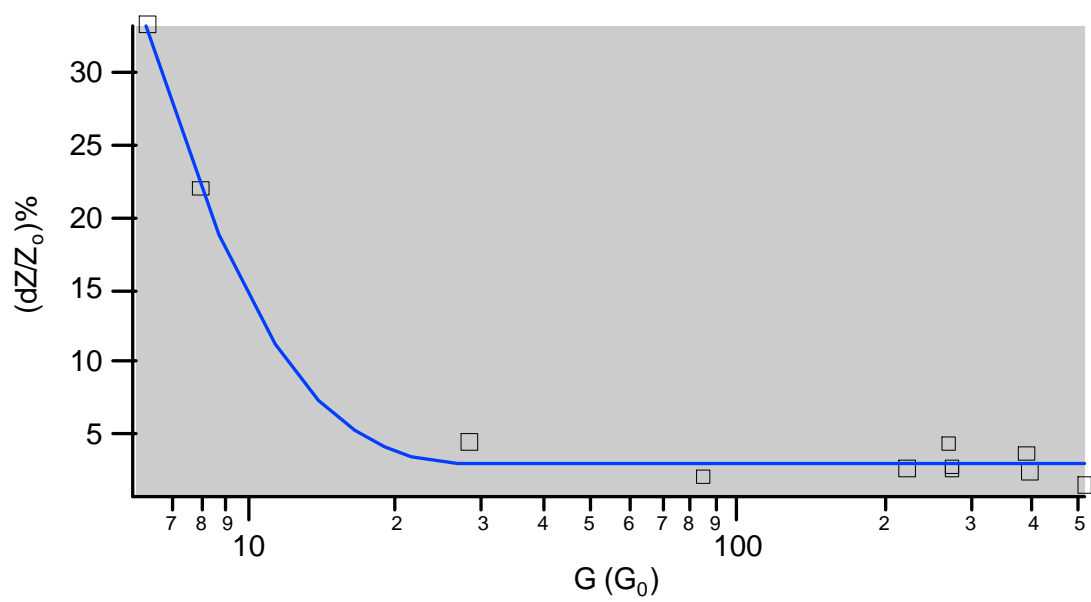


**Figure 4.4:** Plot of the normalized change in impedance  $(dZ/Z_0)\%$  from introducing MPA/H<sub>2</sub>O to various Au junction sizes in terms of  $G_0$ .

due to chemisorption. Thiol would not chemisorb to an atom-scale junction formed from the Ti or Cr adhesion layer, which would explain a low response if HDT was introduced to an atom-scale junction composed of Ti or Cr. A Ti atom-scale junction was possible if directional electrodeposition caused the anode to etch back while the cathode grew just to the edge of the adhesion layer. One junction with  $G = 3 G_0$ , would not break even with a 3 V sweep, while stable Au junctions typically break with a 350 mV sweep. This increased stability may be due to forming a Ti atom-scale junction, since Ti has a stronger affinity for the glass substrate than Au. Another junction,  $G = 31 G_0$ , had a minimal response to 10 mM HDT and was able to hold up to flow rates that typically break even stable junctions.

#### 4.3.5 Thiol Desorption

The thiols were desorbed from the electrode before regenerating a junction. Simply breaking the junction and rinsing was considered, but the thiol molecules on the thin film electrode could contaminate a newly formed junction. Initially, the PDMS microfluidic channel was removed for the thiols to be removed either with piranha solution (5 min) or ozone (25 min). Removing the PDMS channel often disturbed the junction area, so ozone was delivered through the channel. By desorbing the thiols in the channel with ozone, AC impedance measurements were possible during desorption. The desorption results were comparable to adsorption results. For a run with 10 mM MPA, the  $\Delta Z$  was about 5% for the thiol adsorption and the ozone-induced thiol desorption (Figure 4.5). The small change in impedance at the beginning of the desorption curve was caused when the ozone entered the channel and displaced the MPA. The small

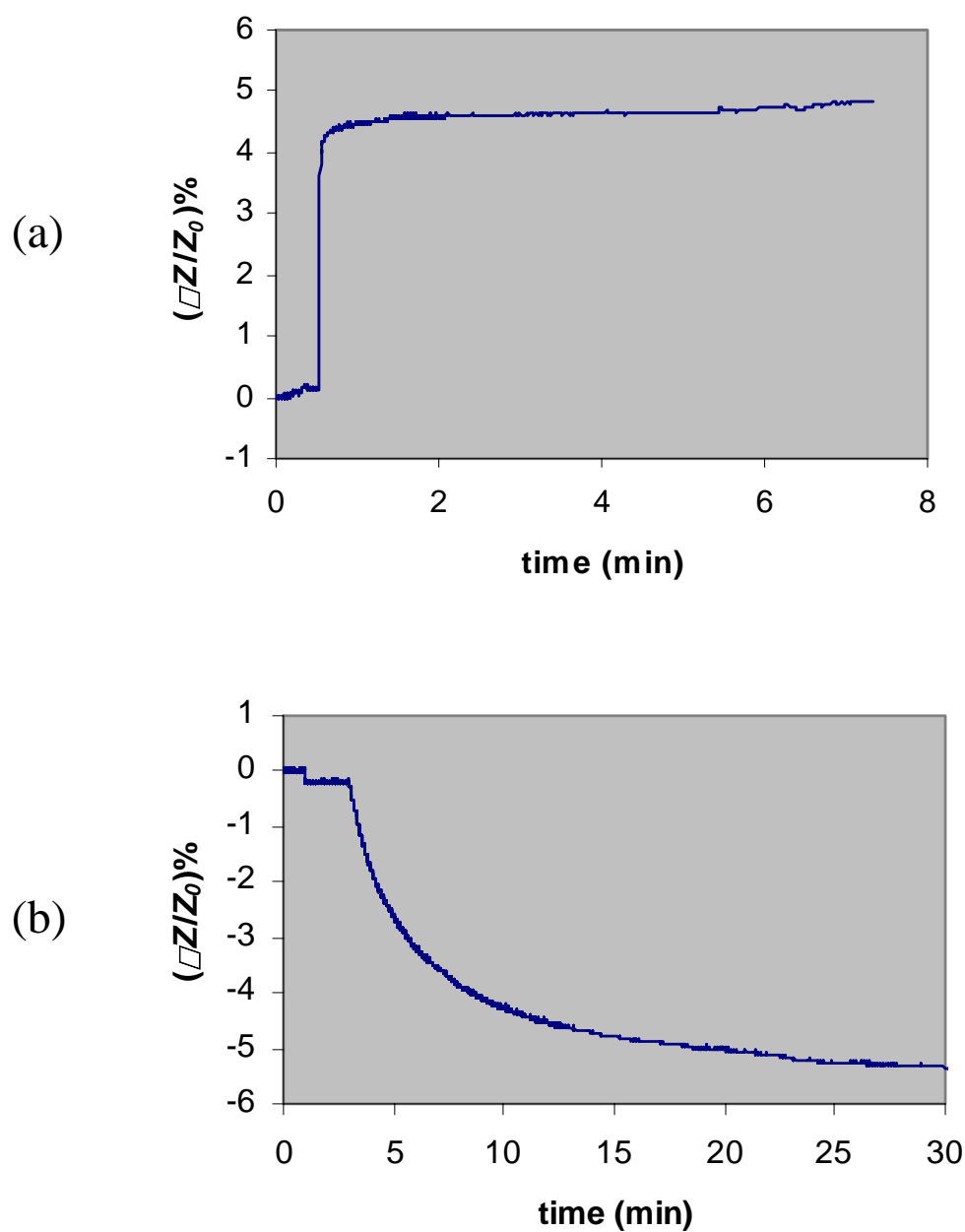


**Figure 4.5:** Plots for change in impedance ( $\Delta Z/Z_0$ ) as 10 mM MPA was chemisorbed (a) to a 270  $G_0$  Au junction and then desorbed (b) by introducing ozone to the junction. The  $\Delta Z/Z_0$  for the thiol adsorption and desorption were comparable ( $\sim 5\%$ ).

impedance change in the beginning of the adsorption curve was caused from the pressure effect when the pump was engaged.

#### 4.3.6 Noise

Noise was a concern when scaling the conductance measurements down from a 1 cm<sup>2</sup> area on a thin Au film to atom-scale junctions. The goal of detecting small changes in adsorbed population for an atom-scale junction was based on the noise being comparable to the noise measured with the thin Au film (61 nV).<sup>14</sup> For measurements with the 8 k $\Omega$  atom-scale junction (1.6 G<sub>0</sub>), the noise was below the digital steps of 244.14 nV.

Intrinsic (random) noise sources are part of all electronic signals.<sup>17</sup> The intrinsic noise from the resistance through the Au film or atom-scale junction (Johnson noise) is due to thermal fluctuations in the resistor electron density. These fluctuations cause an open-circuit voltage,

$$V_{Johnson} = \sqrt{4kTRB}$$

where  $k$  is Boltzmann's constant ( $1.38 \times 10^{-23}$  J/°K),  $T$  is temperature (°Kelvin),  $R$  is resistance (Ohms), and  $B$  is the measurement bandwidth. Johnson noise is independent of size and material type. Since the Johnson noise varies primarily with  $R$ , the atom-scale junction will have greater Johnson noise, if all other variables remain the same. An 8 k $\Omega$  atom-scale junction (1.6 G<sub>0</sub>) was calculated to have 185 nV of Johnson noise with the AC lock-in time constant set at 300  $\mu$ s ( $B = 260$  Hz). By increasing the instrument time constant from 300  $\mu$ s to 300 ms, the calculated Johnson noise is lowered to 6 nV; however, this decreased sampling frequency could filter important data from the signal.

The noise measured above the Johnson noise (resistor/ thermal noise) could be from two other sources of intrinsic noise, shot noise (current noise) and 1/f noise (“flicker” or “pink” noise).<sup>17</sup> The shot noise is from non-uniformity in the electron flow and has a linear dependence on current.<sup>18</sup> The noise level from the preamplifiers on the AC lock-in generally exceed the shot noise. The 1/f noise is of course universal and arises from a distribution of mechanisms. The 1/f noise was minimized by using the AC lock-in amplifier at a high frequency (5 kHz). Furthermore, the AC lock-in measures the part of the signal that is at a specific frequency and phase relative to a reference signal, eliminating noise from all frequencies except a small band of frequencies around the reference frequency.<sup>3</sup> To mitigate noise from junction potentials at dissimilar metal interfaces, the thin Au wire connectors were pressed firmly against the thin Au film electrodes.

Although a Fourier Transform of the noise demonstrated a random distribution of frequencies (Figure 4.6), the measurements were still vulnerable to various external sources of noise like lighting fixtures and computer monitors, as well as interactions between the experiment, detector, and lock-in amplifier. These noise sources could interact with the signal by capacitance coupling, inductive coupling, resistive coupling, ground loops, microphonics, and thermocouple effects. Due to different experimental set ups, these external noise sources will vary when comparing the results from Au thin films and atom-scale junctions, contributing to the difference in noise between the Au thin film measurements (61 nV) and the atom-scale junction measurements (< 244.14 nV). Figure 4.7 demonstrates the noise reduction from fixing a ground loop on the DAQ pin board. To mitigate the various sources of noise, a 4 Hz low pass filter was added between the

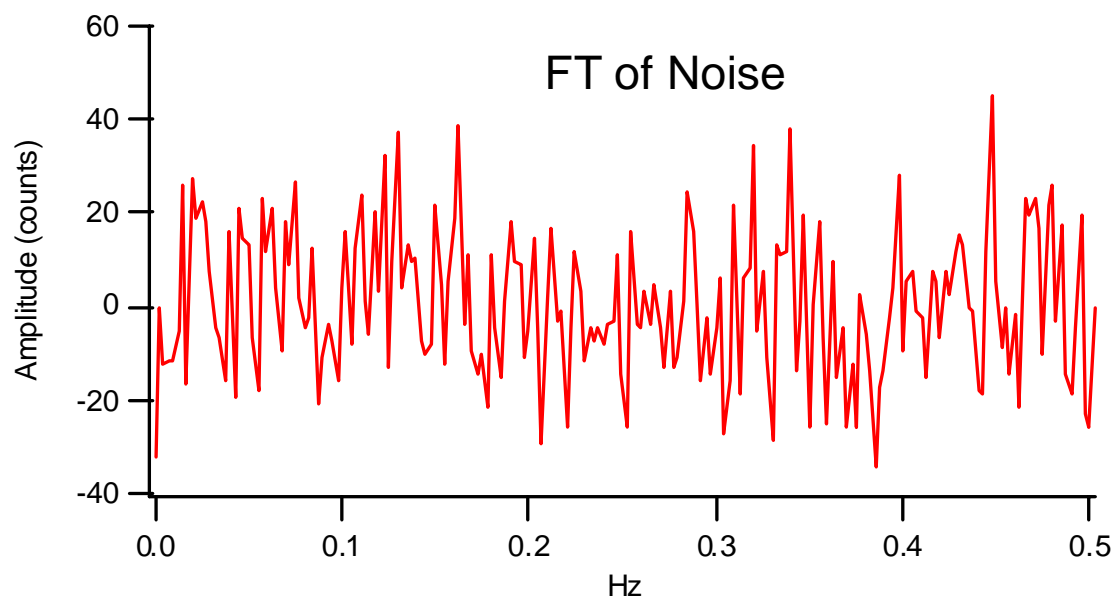


**Figure 4.6:** The Fourier Transform of the noise demonstrated a random distribution of frequencies (low frequency portion).

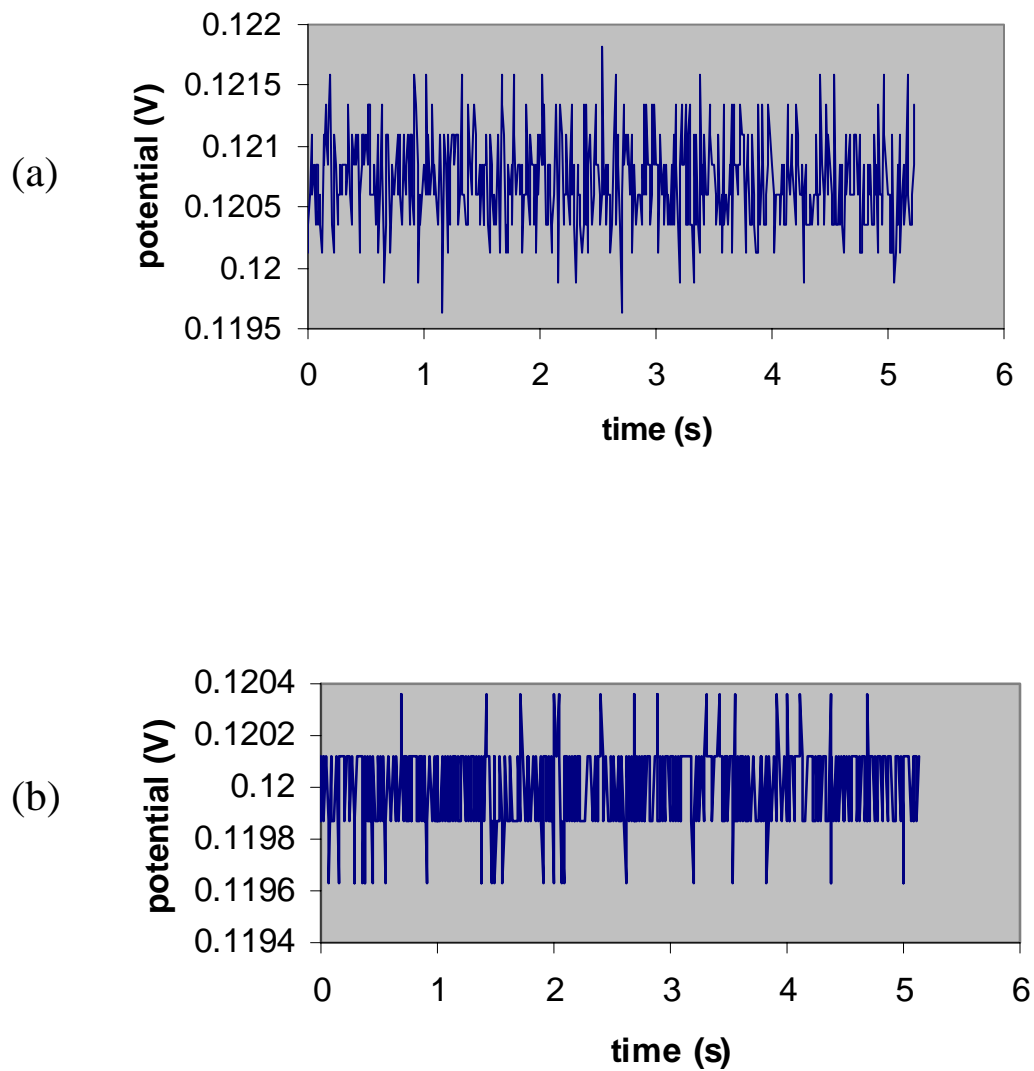


**Figure 4.7:** Potential verses time plots for analyzing the noise before (a) and after (b) the ground loop was corrected. The analysis was performed with an 8-kohm resistor, representing a  $1.6 G_0$  atom-scale junction.



AC lock-in output and the DAQ card (Figure 4.8). Figure 4.8 also demonstrates that the true noise (not digital steps) was measured with the narrower DAQ range, which is addressed further in the Future Directions (Chapter 5).

#### 4.4 Conclusions

The goal of this work was to fabricate regenerable atom-scale junctions for detecting small numbers of Lewis base adsorbates (*e.g.* thiol), with sensing based on impedance change from analyte chemisorption. Ultimately, this sensor would be engineered into a miniature, field-deployable chemical agent detection device. Although the development of this particular device is at an early stage, the relevance to sensor technology is clear. The most important characteristics of the device are: (1) the ability to regenerate the sensing structure once used and (2) the extreme mass sensitivity. The sensor consists of a Au atom-scale junction, fabricated with a controllable electrochemical method. Based on conductance measurements ( $I$ - $V$  curves) and estimates from SEM images, atom-scale junctions were successfully formed. By incorporating all of the critical fabrication steps within a microfluidic channel, it is possible to sequentially prepare an atom-scale junction with well defined conductance properties, test an analyte-containing solution, and then regenerate a new atom-scale junction to perform another measurement cycle. The other salient feature is the extreme mass sensitivity of the atom-scale junction. By exploiting the inherent low-noise properties of the  $I$ - $V$  measurement for an atom-scale Au junction, one could assay very small numbers of analyte molecules, a necessary capability for use in mass-limited chemical analysis. The capabilities of these structures for measurements of small numbers of adsorption/desorption events

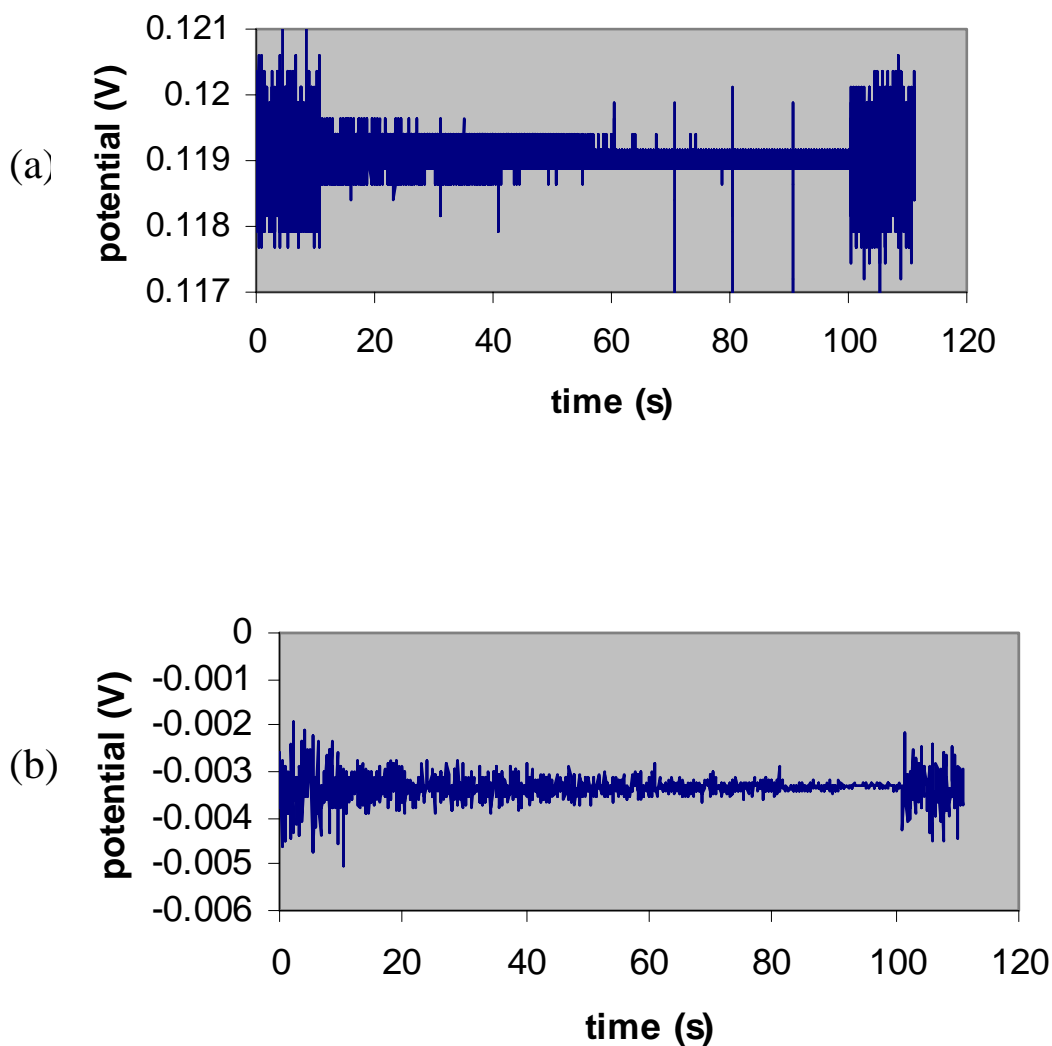


**Figure 4.8:** Potential verses time plots that demonstrate the noise reduction as the signal filtering was increased about every 10 seconds and then back to no filtering at 100 s. The low pass filter had 9 settings, from no filtering (setting 0) to 4 Hz (setting 9). (a) With a DAQ range of 1.0 V (244.14 nV digital steps), the noise magnitude was less than the digital steps. (b) The signal was offset in order to capture the signal with a DAQ range of 0.1 V (24.41 nV steps), which allowed the noise to be observed.

makes a powerful case for pushing the limits of sensitivity to electrical measurements of single molecule events.

#### 4.5 References

- (1) WS Augerson: A Review of the Scientific Literature as It Pertains to Gulf War Illnesses, RAND, 2000.
- (2) S Weiss: "Fluorescence Spectroscopy of Single Biomolecules" *Science* 283 (1999) 1676-1683.
- (3) AL Swint: In-Plane Conductance of Thin Films as a Probe of Surface Chemical Environment: Adsorbate Effects on Film Electronic Properties of Indium Tin Oxide and Gold, Dissertation, University of Illinois, Urbana-Champaign, 2003.
- (4) AF Oberhauser, C Badilla-Fernandez, M Carrion-Vazquez, JM Fernandez: "The mechanical hierarchies of fibronectin observed with single-molecule AFM" *J. Mol. Biol.* 319 (2002) 433-447.
- (5) Y Cui, Q Wei, H Park, CM Lieber: "Nanowire Nanosensors for Highly Sensitive and Selective Detection of Biological and Chemical Species" *Science* 293 (2001) 1289-1292.
- (6) S Boussaad, NJ Tao: "Atom-size gaps and contacts between electrodes fabricated with a self-terminated electrochemical method" *Appl. Phys. Lett.* 80 (2002) 2398-2400.
- (7) A Bard, L Faulkner: *Electrochemical Methods*, John Wiley & Sons, New York, 1980.
- (8) CZ Li, HX He, NJ Tao: "Quantized tunneling current in the metallic nanogaps formed by electrodeposition and etching" *Appl. Phys. Lett.* 77 (2000) 3995-3997.

- (9) CZ Li, NJ Tao: "Quantum transport in metallic nanowires fabricated by electrochemical deposition/dissolution" *Appl. Phys. Lett.* 72 (1998) 894-896.
- (10) EC Walter, MP Zach, F Favier, BJ Murray, K Inazu, JC Hemminger, RM Penner: "Metal nanowire arrays by electrodeposition" *Chemphyschem* 4 (2003) 131-138.
- (11) EC Walter, BJ Murray, F Favier, G Kaltenpoth, M Grunze, RM Penner: "Noble and coinage metal nanowires by electrochemical step edge decoration" *Journal of Physical Chemistry B* 106 (2002) 11407-11411.
- (12) CZ Li, A Bogozi, W Huang, NJ Tao: "Fabrication of stable metallic nanowires with quantized conductance" *Nanotechnology* 10 (1999) 221-223.
- (13) PJ Castle, PW Bohn: "Interfacial scattering at electrochemically fabricated atom-scale junctions between thin gold film electrodes in a microfluidic channel" *Anal. Chem.* 77 (2005) 243-249.
- (14) YM Zhang, RH Terrill, PW Bohn: "Chemisorption and chemical reaction effects on the resistivity of ultrathin gold films at the liquid-solid interface" *Anal. Chem.* 71 (1999) 119-125.
- (15) Y Zhang, RH Terrill, PW Bohn: "In-plane resistivity of ultrathin gold films: A high sensitivity, molecularly differentiated probe of mercaptan chemisorption at the liquid-metal interface" *J. Am. Chem. Soc.* 120 (1998) 9969-9970.
- (16) K Hansen, SK Nielsen, M Brandbyge, E Laegsgaard, I Stensgaard, F Besenbacher: "Current-voltage curves of gold quantum point contacts revisited" *Appl. Phys. Lett.* 77 (2000) 708-710.
- (17) SR Systems: SR830 DSP Lock-In Amplifier Operating Manual, 1999.

- (18) HE van den Brom, JM van Ruitenbeek: "Quantum suppression of shot noise in atom-size metallic contacts" *Physical Review Letters* 82 (1999) 1526-1529.

## **CHAPTER 5**

### **FUTURE DIRECTIONS**

#### **5.1 Junction Stability and Control**

The recommendations are targeted at improving the stability of the atom-scale junction for introducing analyte and improving the control of the comparator-terminated directional electrodeposition method of forming atom-scale junctions.

##### **5.1.1 Decrease Inter-Electrode Distance**

The fabricated inter-electrode gap was critical to the stability and control of electrochemically formed atom-scale junctions. As the inter-electrode gap widens, more Au is deposited on bare glass (no adhesion layer) to decrease the gap size leading up to the atom-scale junction, and the Au deposited on the bare glass is more vulnerable to disturbance. Furthermore, with more Au deposition comes the possibility of dislodging Au nano-particles, which can interfere with junction formation. Instead of forming a junction based on depositing one Au atom at a time with directional electrodeposition, comparatively weaker and thicker junctions are formed when nano-particles are incorporated into the junction. Therefore, junctions formed with smaller inter-electrode gaps and less electrodeposited Au tend to be formed with greater control and are more stable.

Electron beam lithography was used to fabricate electrodes spaced  $< 40$  nm apart, as well as nano-bridges (i.e., 40 nm thick, 100 nm wide) that were broken with electromigration for an inter-electrode spacing of  $< 5$  nm (measured tunneling current). Rather than connecting the nanotips with a nano-bridge, the nanotips were also slightly

overdosed to form a nano-scale connection that was broken with electromigration. Since only a few nano-bridge samples were tested, optimum parameters must be determined for reproducible electromigration-induced breaks. The Pine bipotentiostat could be used to sweep a potential, or the other potentiostat could be used to simply hold a bias until the junction breaks. If the nanobridge is broken in solution, the breakage could be more confidently attributed to electromigration (atom movement) over heating effects. This confidence would be raised by cooling the junction area with He (g) or  $\text{N}_2(\text{l}) \leftrightarrow \text{N}_2(\text{g})$  through the microfluidic channel. To avoid disturbing the junction area with gas flow through the microfluidic channel, the device could instead be cooled in a chamber. Based on the reported reproducible inter-electrode gap size of  $< 5$  nm and preliminary experiments confirming  $< 5$  nm inter-electrode gaps (measured tunneling current),<sup>1</sup> electromigration-induced break junctions should be highly considered in lieu of the  $< 40$  nm spaced nanotips.

### **5.1.2 Introduce Analyte with Less Force**

Since it was an exception for atom-scale junctions to hold up the lowest peristaltic pump flow (0.6 ml/ min), ways of introducing the analyte with less force should be considered. For example, a syringe pump is capable of introducing the analyte at a minimum flow rate of 0.003  $\mu\text{L}/\text{min}$ . The syringe pump will allow the rate to be lowered for assessment. Another option would be to form an atom-scale junction in a PDMS open reservoir that is covered with a polycarbonate membrane. The analyte could be placed drop-wise on the membrane and allowed to slowly diffuse through the membrane and electrolyte to the junction area. Unfortunately, the open reservoir approach does not allow for an efficient means of exchanging solutions.

Introducing the analyte to the junction as a gas would allow even a lower probability of junction disturbance. Swint *et al* introduced gas phase octanethiol molecules by flowing a stream of N<sub>2</sub> through a flask, containing neat octanethiol, that was connected to the flow cell.<sup>2</sup> Octanethiol, C<sub>8</sub>H<sub>17</sub>SH, is a great option when taking into consideration volatility and surface diffusion. The nanofilm (800 nm x 150 nm x 20 nm) resistance in the monolayer saturation region was less than expected based on extrapolations from the macroscopic measurements (1 cm x 1 cm x ~50 nm). Perhaps the concentration of octanethiol in the N<sub>2</sub> stream was sufficient for complete monolayer formation. The lower resistance could also be a result of contamination, in which case the analyte could be triple distilled in an oxygen and water free environment. Furthermore, a high purity gas flow line could be implemented where high purity N<sub>2</sub> gas flows through thick Teflon tubing to a 0.01μm membrane particulate filter before entering the analyte flask and then the flow cell (Figure 5.1).

### 5.1.3 Decrease Temperature

As discussed in the *Background* section, the atom-scale junctions are more stable at lower temperatures. The experiments could be contained in a Styrofoam chamber and cooled with He (g) or N<sub>2</sub> (l) ↔ N<sub>2</sub> (g).<sup>2</sup>

### 5.1.4 Mitigate Electrostatic Charge and Potential Difference

The substrate electrostatic charge or the inter-electrode potential difference can be significant enough to break an atom-scale junction by heating or electromigration of Au atoms. The electrostatic charge induced breakage of nanotips was resolved by switching to an oxidized Si substrate, but the potential difference from switching the leads between



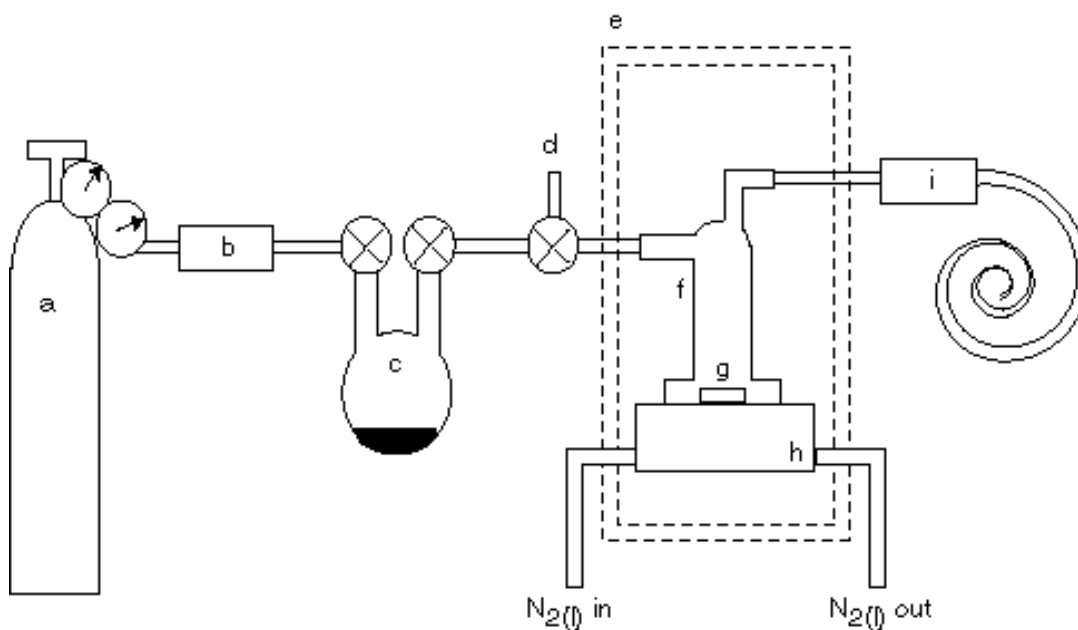


**Figure 5.1:** Schematic of experimental set up designed to reduce contamination of the atom-scale junction sensor. The analyte would be triple distilled in an oxygen and water free environment. Furthermore, a high purity gas flow line would be implemented, where high purity  $N_2$  gas flows through thick Teflon tubing to a  $0.01\mu m$  membrane particulate filter before entering the analyte flask and then the flow cell: a) ultra high purity  $N_{2(g)}$  and regulator, b)  $0.01\mu m$  particulate filter, c) distilled alkanethiol delivery flask, d) waste vent, e) double Faraday cage, f) flow cell, g) device containing PDMS microfluidic flow cell and atom-scale junction, h) cooled/ magnetically shielded box, and i) moisture filter.<sup>2</sup>

potentiostats is still a concern. Swint *et al* remedied this by shorting the electrodes until the potentiostat leads were attached.<sup>2</sup>

### 5.1.5 Reduce Au Nano-Particle Interference

When regenerating multiple samples, Au nano-particles build up across the cathode area submerged in the electrolyte (in channel). These nano-particles are dislodged by solution change out and potential change. If dislodged, the nano-particles often interfere with atom-scale junction formation. Therefore, before regenerating a new junction, the peristaltic pump could be used to intentionally dislodge any loose nano-particles by rinsing with a high flow rate (3 ml/min). Since the channel is not plasma-treated, it can be removed for piranha cleaning. Rather than removing loose Au nano-particles, perhaps the nano-particles would be stabilized by electrochemical cycling or annealing?

Au nano-particle interference would be reduced dramatically if the Au deposition was limited to the nanotip edges. This is possible with a lithography scheme designed to leave the nanotips and pads covered with photoresist. Since etchants are able to get under the photoresist (under-etching), Au<sup>+3</sup> should be reduced (deposit) at the nanotip anode edge. The photoresist could be removed with a q-tip in the area of the lead press connections.

### 5.1.6 Photochemical Growth

Due to potential isolated growth in the junction (limited nano-particle interference), the photochemical growth of Ag nanocrystals is worth considering. Brus *et al.* synthesized Ag nanocrystal seeds by reducing Ag with borohydrate.<sup>3</sup> Ag nanocrystals (100  $\mu$ L) were introduced to a sample of 50  $\mu$ L of 10 mM Ag<sup>+</sup> ions, 50  $\mu$ L of 5 mM

citrate, and 800  $\mu\text{L}$  of nanopure  $\text{H}_2\text{O}$ . The  $\text{Ag}^+$  ions adsorbed on the Ag nanocrystals and were capped by the citrate ligand. The Ag nanocrystals were photoexcited with a laser, and the citrate acted as a reducing agent for growing the Ag nano-particles. By polarizing laser light that is  $> 400\text{ nm}$ , the Ag nano-particles grew in an oval shape. The impact of the polarizer should be assessed by attempting laser-induced photochemical growth with and without a polarizer. For a photochemical growth control, the current should be monitored for 30 min before the laser light is introduced.

After forming an atom-scale gap with the comparator-terminated directional electrodeposition method, the reactants could be introduced to the junction area through the microfluidic channel: Ag nanocrystals,  $\text{Ag}^+$  ions, and citrate ligand. Then, polarized laser light could be directed onto the junction. The Ag nano-particle growth could be monitored by measuring the current between the electrodes. The laser-induced growth could be stopped with a comparator-terminated circuit, where the junction size is determined by a preset current. This could also be attempted with  $\text{Au}^{+3}$  ions.

#### 5.1.7 AC Monitoring of Junction Conductance

Morpurgo *et al.* reported an electrochemical method of forming atom-scale junctions that involved monitoring the junction resistance with AC instead of DC (Figure 5.2).<sup>4</sup> Directional electrodeposition was accomplished by applying a DC potential between one of the working electrodes and a sacrificial Au counter electrode (anode). Au deposition could also be accomplished by applying a potential between one of the working electrodes and a Pt counter electrode in the presence of Au deposition solution [ $\text{Au}^{+3}$ ]. By depositing on just one working electrode, the junction area will be better isolated for analysis. The sacrificial Au wire electrode removed directional

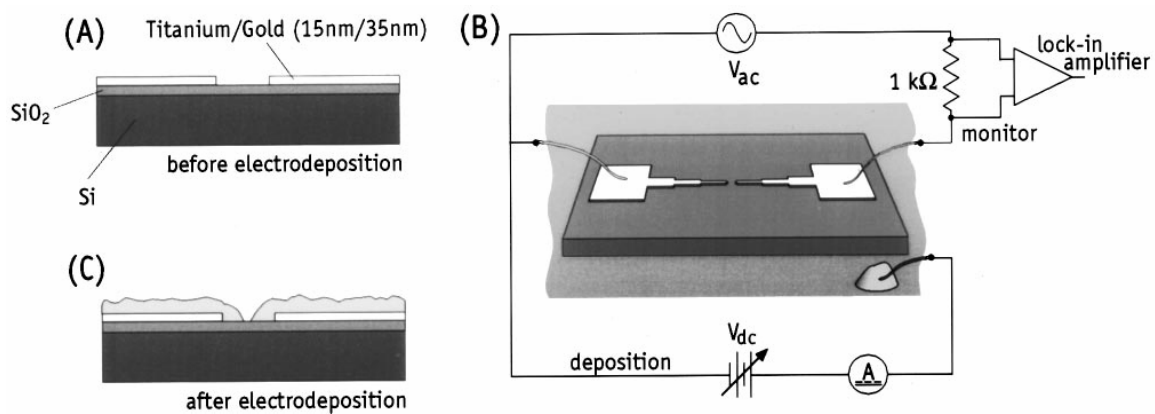


**Figure 5.2:** Experimental set up for electrochemically forming atom-scale junctions as reported by Morpurgo *et al.* The junction resistance was monitored with AC instead of DC. Directional electrodeposition was accomplished by applying a DC potential between one of the working electrodes and a sacrificial Au counter electrode (anode).<sup>4</sup>

electrodeposition between the nanotips, which eliminated the release of Au nano-particles from switching the nanotip anode/cathode. The nanotip anode/cathode was switched with prior experiments when the thin film Au anode was close to exhaustion, as determined by observing anode thinning with a 40X objective. This would not be a problem if using a comparatively large sacrificial Au wire (0.25 mm) counter electrode (anode).

This approach was given some attention in the pursuit of better-controlled formation of more stable atom-scale junctions, but time was not available for working through an issue with the experimental set up. For terminating the deposition with a comparator, the current between the working electrodes was monitored with 10 kHz AC (low voltage) and converted to DC with a precision rectifier. Initial tests demonstrated the ability to build up the working electrodes and etch the working electrodes back by reversing the DC. Unfortunately, the current representing the AC component was apparently not based only on the resistance of the junction. The DC deposition potential controlled the AC through the junction like the gate voltage of a FET, with the AC increasing and decreasing while adjusting the DC potential. The measured current could only be due to the AC component since it is high pass filtered. If the described issue is resolved, this AC monitoring method may offer additional control in making more stable atom-scale junctions.

#### **5.1.8 Referenced Electrodeposition**

Using a Ag/AgCl reference electrode with the Pine bipotentiostat may allow better junction isolation, stability, and formation control. Furthermore, a referenced system should allow better reproducibility of measurements/ effects and allow control of

thiol desorption for reusing a device. To preserve the electrodes and further isolate the junction area, a referenced system would enable a deposition-only experiment ( $[\text{Au}^{+3}]$ ) by setting the potential range away from the etching potential. A referenced system could poise the working electrodes for a potential range that isolates slow deposition (lower current density) in the junction area, possibly resulting in better formation control. This approach should reduce the build up of Au nanoparticles that could interfere with junction formation control, stability, and isolation.

To set up the Pine potentiostat for comparator-terminated formation of atom-scale junctions, the current between the working electrodes is required. According to Ed Berti at Pine Instruments, a possible way of determining the current between the working electrodes is to subtract the sum of the working electrode currents from the total current.<sup>5</sup> The potentiostat provides the current out of (or into) both  $K_1$  and  $K_2$ . The current out of (or into) the counter electrode (CE) could be measured via a resistor in series with the counter electrode jack. Solving for the current between  $K_1$  and  $K_2$  involves three equations with three unknowns:  $I_3 = I_1 + I_2$ ;  $I_1 = I_a + I_c$ ; and  $I_2 = I_b + I_c$  (current polarity needs to be considered). The known variables are the CE current ( $I_3$ ), the  $K_1$  current ( $I_1$ ), and the  $K_2$  current ( $I_2$ ). The unknown variables are the currents from CE to  $K_1$  ( $I_a$ ), from CE to  $K_2$  ( $I_b$ ), and from  $K_1$  to  $K_2$  ( $I_c$ ). The current between the working electrodes ( $I_c$ ) is determined by subtracting the sum of the working electrode currents ( $I_1 + I_2$ ) from the total counter current ( $I_3$ ) through the atom-scale junction,  $I_c = I_3 - (I_1 + I_2)$ . This referenced comparator-terminated method was not actively pursued due to limited time and concern that the current between the working electrodes could be compromised by

the error in the current to voltage converters, which are not meant for precision measurements.<sup>6</sup>

### 5.1.9 Two-Component Junction

A two-component electrochemically fabricated atom-scale heterojunction (*e.g.* Au and Ag) may have improved control and stability, as well as unique properties that can be exploited for nanoscience applications. What is the interfacial scattering magnitude difference from analyte chemisorption with a two-component junction? After forming an atom-scale gap between Au electrodes utilizing the comparator-terminated directional electrochemical method, a Ag deposition solution [ $\text{Ag}^+$ ] could be introduced through the microfluidic channel, and the cathode could be poised for deposition. A two-component atom-scale junction could be attempted by introducing a deposition solution with both [ $\text{Au}^{+3}$ ] and [ $\text{Ag}^+$ ].

## 5.2 Imaging Junction

Atom-scale junctions usually break if the electrolyte is allowed to evaporate. This breakage could possibly be reduced by imaging the junction with Environmental SEM under 100% relative humidity. Even better, the experimental set up (device, potentiostat, DAQ) could possibly be configured with an AFM for real time imaging during junction formation (in solution). This real time imaging may provide valuable insights for atom-scale junction formation that could be used for improving the control and stability of atom-scale junctions. For AFM imaging, the device should be fabricated on mica (< 1 angstrom of roughness) for a more meaningful junction thickness measurement.

## 5.3 Sensing

### 5.3.1 Noise Reduction

By increasing the DAQ precision (reduce potential range) and decreasing the noise associated with this electrically transduced sensing scheme, the sensitivity will increase, moving this scheme closer to realizing single molecule detection. The 12-bit DAQ card used in the experiment had a max range of  $\pm 10$  V with precision settings (digital step size) of 4.88 mV ( $\pm 10$  V), 2.44 mV ( $\pm 5$  V), 244  $\mu$ V ( $\pm 0.5$  V), and 24  $\mu$ V ( $\pm 0.05$  V). These ranges were adequate to measure the signal and even the noise ( $< 244$  nV) because the AC lock-in amplified the signal by 1000. To capture signal change ( $\Delta Z$ ) from chemisorption on the atom-scale junction, the  $\pm 5$  V range was required. However, to resolve the noise in the saturation region, the precision of the  $\pm 0.05$  V range was required. Therefore, after the signal leveled off in the saturation region of the adsorption curve, the DAQ range would have to be lowered to capture the noise and in turn the conductance fluctuations from molecular adsorption and desorption events on the atom-scale junction. To avoid interrupting the measurement when switching the DAQ range, a 16-bit DAQ card could be used, which has the required range for the signal and precision for the noise.

The noise could be reduced with digital filtering software (autocorrelation analysis, window averaging) and experimental set up modifications. Swint, *et al.* reduced the noise for the macro-scale ( $1 \text{ cm}^2$ ) Au thin film measurements from 61 nV to 20.5 nV by addressing the external noise with experimental set up modifications (Figure 5.3).<sup>2</sup> To counter the coupling of external noise sources (computer monitor, light fixtures, etc) with the measured signal, the experiment was enclosed in a Faraday cages made of fine copper



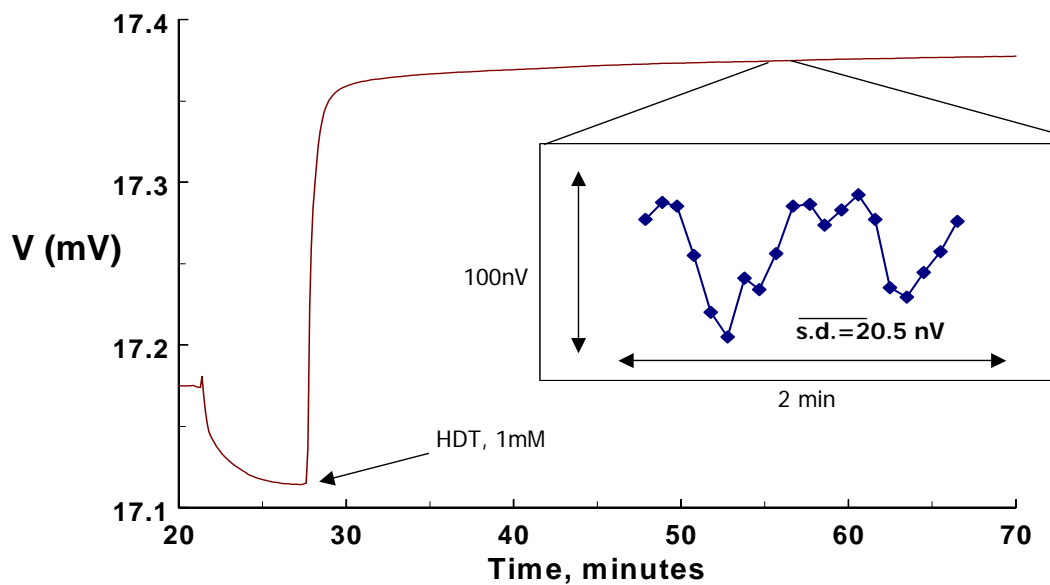


**Figure 5.3:** Adsorption curve for the introduction of 1 mM HDT/ EtOH to the surface of a 50 nm Au film. Swint, *et al.* made several experimental set up modifications, reducing the noise in the monolayer saturation region from a standard deviation of 61 nV to 20.5 nV.<sup>2</sup>

mesh. The cage shielded the experiment from external electromagnetic, mechanical and acoustic vibrations. The electronics and the device were also contained in a box made of magnetically shielding  $\mu$ -metal. To prevent noise-inducing ground loops, the cages and the instruments were grounded to a common physical point.<sup>7</sup> The Faraday cage was lined with Styrofoam and  $N_2(l) \leftrightarrow N_2(g)$  flowed through chamber to lower the experimental temperature and decrease the thermal (Johnson) noise. To minimize capacitive coupling, all electrical leads were shortened as much as possible. Furthermore, the leads were tied together to prevent loops susceptible to inductively coupled noise effects. The sensitivity of the electrically transduced sensing scheme for atom-scale junctions could be improved by increasing the lock-in amplifier time constant (Johnson noise from 185 nV to 6 nV) and by addressing the external noise like Swint *et al.* (61 nV to 20.5 nV).

### 5.3.2 Threshold Junction Size for Sensing

Junctions below  $20 G_0$  move from a chemisorbed-induced resistance change typically found with thin Au films ( $\sim 3\%$ ) to the larger-scale resistance change found in atom-scale junctions ( $>30\%$ ). This threshold junction size should be more closely defined by further populating the  $(\Delta Z/Z_0)\%$  vs.  $G_0$  plot (Figure 4.4). This data could be used to determine a practical balance between Au junction thickness (stability) and analyte detection level for implementation into a detection device.

### 5.3.3 Analytes

MPA is a great candidate for assessing the impact of gradually changing the surface dipole by adjusting the pH. By increasing the pH with a phosphate buffer, the MPA will have a more negative surface, which will modify the surface dipole. This will in turn affect the interfacial scattering, measured by the change in resistance.

After characterizing thiols, analytes with some of the same functional groups as chemical agents could be assessed. For example, low toxicity phosphines may adsorb similarly to a high toxicity phosphine nerve agent (like Tabun).

Biological agent sensing could be probed by introducing an analyte that models an affinity tag for a biological agent, *e.g.* CKWAKWAK (Cys-Lys-Trp-Ala-Lys-Trp-Ala-Lys).

#### **5.3.4 Chemical Isolation of Junction**

Since the resistance in the atom-scale junction was very large in comparison to the lead contact pads, the change in impedance ( $\Delta Z$ ) was attributed to changes with the junction (size and chemisorption). This could be highlighted by limiting the chemisorption to the junction. An atom-scale gap could be formed by closing the inter-electrode gap until tunneling current was measured ( $< 5$  nm).<sup>8</sup> The Au in the channel could be passivated with a stable, long-chain thiol. Then, an atom-scale junction could be formed and exposed to an analyte that adsorbs well to Au, like thiols or mercury. A reference system is necessary to ensure the passivating thiols are not desorbed ( $> 0.8$  V) while forming the atom-scale junction. The resistance in the junction before adsorbing the analyte would be compared to the resistance after adsorbing the analyte to determine the interfacial scattering impact. If the passivating thiols on the electrodes shift to the junction before analyte is introduced to the atom-scale junction, the passivating thiols could be bound with a linker like polylysine. This junction isolation technique will not work if Au atoms are not able to deposit between the passivating thiols in order to form an atom-scale junction.

### 5.3.5 Single Molecule Detection

Utilizing atom-scale junctions for single molecule detection of Lewis base molecules that mimic highly toxic chemical agents was pursued, with the goal of a field deployable detection device that could save lives. An initial attempt could be to detect the chemisorption of a single particle with many thiol groups (multifunctional adsorbate), like when a single phycoerythrin molecule with many fluorescent moieties was probed.<sup>2,9</sup> Next, a low concentration of thiolated calixarene molecules could be introduced to an atom-scale junction to detect single adsorption events (Figure 5.4).<sup>10</sup> A large thiolated molecule would be difficult to remove with ozone desorption, but the junction could be simply regenerated for additional analysis (section 3.2.8). Current fluctuation analysis (auto correlation) may confirm the molecular adsorption events.

### 5.4 Molecular Electronics

Molecular-scale gaps could be used for exploring the concept of molecular electronics.<sup>11</sup> The comparator-terminated electrochemical fabrication method for atom-scale junctions is equally well suited to form molecular-scale gaps, which could then be derivatized suitably with chemisorbed molecule(s) to yield a nanowire in which the conductance is ultimately determined by the electrical properties of the molecule(s). The molecular-scale gap could be bridged initially with a large conjugated dithiol and characterized with resistance measurements (*I-V* plots). Others have already succeeded in making conductance measurements through large molecules (*e.g.* DNA) employing the STM and MCBJ techniques.<sup>12</sup> However, other one-dimensional conductors (molecules) may have unique properties for use in molecular-based circuits. In the future, molecules

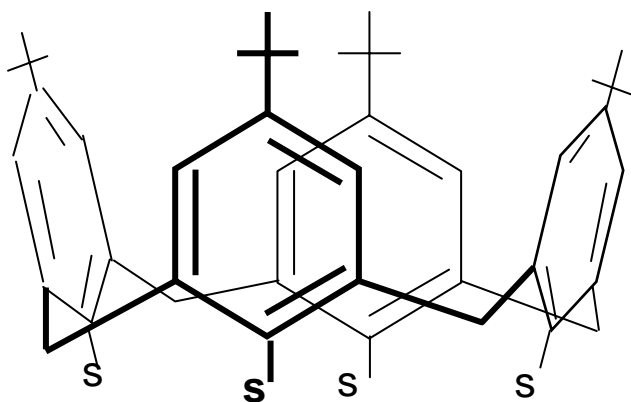


**Figure 5.4:** Drawing of *p*-*tert*-butylcalix[4]arenetetrathiolate. A low concentration of large thiolated calixarene molecules, like *p*-*tert*-butylcalix[4]arenetetrathiolate, could be introduced to an atom-scale junction to detect single adsorption events.<sup>2,10</sup>

may be designed for a specific function in an electronic circuit: diodes, electronic mixers, or switching elements.<sup>13-15</sup>

## 5.5 References

- (1) H Park, AKL Lim, AP Alivisatos, J Park, PL McEuen: "Fabrication of metallic electrodes with nanometer separation by electromigration" *Appl. Phys. Lett.* 75 (1999) 301-303.
- (2) AL Swint: In-Plane Conductance of Thin Films as a Probe of Surface Chemical Environment: Adsorbate Effects on Film Electronic Properties of Indium Tin Oxide and Gold, Dissertation, University of Illinois, Urbana-Champaign, 2003.
- (3) LE Brus, Photochemical Ag particle shape/size control, AFOSR MURI, WPAFB, OH, 2004.
- (4) AF Morpurgo, CM Marcus, DB Robinson: "Controlled fabrication of metallic electrodes with atomic separation" *Appl. Phys. Lett.* 74 (1999) 2084-2086.
- (5) E Berti, VP Engineering for Pine Instruments, 2005.
- (6) J Wentz, University of Illinois, School of Chemical Sciences, 2005.
- (7) SR Systems: SR830 DSP Lock-In Amplifier Operating Manual, 1999.
- (8) S Boussaad, NJ Tao: "Atom-size gaps and contacts between electrodes fabricated with a self-terminated electrochemical method" *Appl. Phys. Lett.* 80 (2002) 2398-2400.
- (9) M Wu, PM Goodwin, WP Ambrose, RA Keller: "Photochemistry and fluorescence emission dynamics of single molecules in solution: B-phycoerythrin" *J. Phys. Chem.* 100 (1996) 17406-17409.

- (10) MT Cygan, GE Collins, TD Dunbar, DL Allara, CG Gibbs, CD Gutsche:  
"Calixarene monolayers as quartz crystal microbalance sensing elements in  
aqueous solution" *Anal. Chem.* 71 (1999) 142-148.
- (11) YQ Xue, S Datta, MA Ratner: "Charge transfer and "band lineup" in molecular  
electronic devices: A chemical and numerical interpretation" *J. Chem. Phys.* 115  
(2001) 4292-4299.
- (12) D Porath, A Bezryadin, S de Vries, C Dekker: "Direct measurement of electrical  
transport through DNA molecules" *Nature* 403 (2000) 635-638.
- (13) CP Collier, EW Wong, M Belohradsky, FM Raymo, JF Stoddart, PJ Kuekes, RS  
Williams, JR Heath: "Electronically configurable molecular-based logic gates"  
*Science* 285 (1999) 391-394.
- (14) N Agrait, AL Yeyati, JM van Ruitenbeek: "Quantum properties of atomic-sized  
conductors" *Physics Reports-Review Section of Physics Letters* 377 (2003) 81-  
279.
- (15) J Chen, MA Reed, AM Rawlett, JM Tour: "Large on-off ratios and negative  
differential resistance in a molecular electronic device" *Science* 286 (1999) 1550-  
1552.